Thermochronologic and geophysical investigations of Canadian Cordilleran crust

Élyse Gaudreau

A thesis submitted in partial fulfillment of the requirements for the
Master's degree in Earth Sciences

Department of Earth and Environmental Sciences
Faculty of Science
University of Ottawa

Abstract

Lithospheric-scale geodynamic processes are interconnected with surface processes such as erosion and tectonic denudation, therefore the integration of geological and geophysical data is valuable when developing geodynamic models. One geodynamic problem that has gained worldwide interest is the contrast in lithospheric properties between the hot and thin Canadian Cordillera and cold and thick North American craton. This thesis focuses on characterizing two aspects of the crust in western Canada: 1) ancient surface and near-surface processes using low-temperature (U-Th)/He thermochronology; and 2) modern geothermal gradients using a wavelet analysis of magnetic anomalies. The first study resolves a differential, tectonically-driven Cretaceous exhumation history in the northern Canadian Cordillera. The second study finds that Curie depths (~580 °C) are shallow throughout the Cordillera, averaging ~15 km, compared to the Canadian Shield, averaging ~33 km. Both studies provide useful constraints for modeling the geodynamic evolution of the Canadian Cordillera.

Résumé

Les processus géodynamiques sont interconnectés avec les processus géologiques superficiels tels que l'érosion et la dénudation tectonique, donc l'intégration de données géologiques et géophysiques est importante dans la conception de modèles géodynamiques. Un problème géodynamique d'intérêt mondial est le contraste entre la lithosphère mince et chaude de la Cordillère Canadienne et la lithosphère épaisse et froide du Bouclier Canadien. Cette thèse a comme but de caractériser deux aspects de la croûte terrestre dans l'Ouest canadien: 1) les processus superficiels anciens par moyen de thermochronologie à basse température (U-

Th)/He; et 2) les gradients géothermiques modernes avec une analyse par ondelettes d'anomalies magnétiques. La première étude dévoile une histoire de dénudation tectonique différentielle dans le nord de la Cordillère Canadienne pendant le Crétacé. Dans la deuxième étude, les profondeurs Curie (~580 °C) calculées dans la Cordillère sont peu profondes (~15 km en moyenne) relativement au Bouclier Canadien (~33 km en moyenne). Ces résultats fournissent des contraintes utiles pour modéliser l'évolution géodynamique de la Cordillère Canadienne.

Acknowledgments

Firstly, I am very grateful to my co-supervisors, David Schneider and Pascal Audet. I thank Dave for constantly pushing my limits and for the many discussions allowing me to understand and interpret my dataset. I thank Pascal, for without his knowledge and ideas, my attempt at geophysics would not have been nearly as successful. I am grateful to both supervisors for their guidance, encouragement, constructive criticism, and for providing me with many opportunities to grow as a scientist.

This project was made possible by funding from a National Science and Engineering Research Counsil (NSERC) grant and a Natural Resources Canada grant to Dave, a NSERC grant to Pascal, and a Canadian Exploration Geophysics (KEGS) Scholarship to myself.

I thank Élise Cossette, Cassy Powell and Meghan Moher for conducting the (U-Th)/He analyses, and thanks are extended to the laboratory groups at University of Texas-Austin and University of Colorado-Boulder for analytical support, as well as Nancy Joyce (Geological Survey of Canada) for facilitating the sampling of archival material at the Geological Survey of Canada. Thanks are extended to Jean-Claude Mareschal (Université du Québec à Montréal) for providing the heat flow data for western Canada and Andy Parsons (University of Oxford) for sharing his results and interpretations of the Yukon River Shear Zone that are currently in review.

I am grateful for many discussions with fellow graduate students and researchers, notably Meghan Moher, Jeremy Powell and Mark Coleman at the University of Ottawa, and Jim Ryan, Alex Zagorevski and Mark Pilkington at the Geological Survey of Canada.

Lastly, I would like to thank my family and friends for their support and patience throughout my studies.

Table of Contents

List of figures

Chapter 2. Widespread Cretaceous exhumation of the Yukon Tanana Terrane, west-central Yukon: upper crustal tectonism resolved by (U-Th)/He thermochronology

Chapter 3. Mapping Curie depth across western Canada from a wavelet analysis of magnetic anomaly data

List of tables

Chapter 2. Widespread Cretaceous exhumation of the Yukon Tanana Terrane, west-central Yukon: upper crustal tectonism resolved by (U-Th)/He thermochronology

Chapter 3. Mapping Curie depth across western Canada from a wavelet analysis of magnetic anomaly data

Chapter 1.

Introduction

The Canadian Cordillera has been studied by geologists and geophysicists for decades because of its complex tectonic history, geomorphology and lithospheric architecture. The crust in the Canadian Cordillera records approximately 750 m.y. of tectonic processes, beginning with the rifting of Laurentia from the Rodinia supercontinent which created the margin where the Canadian Cordillera was subsequently built (Monger & Price 2002 and references therein). The Cordillera is composed of multiple sedimentary basins, magmatic arcs and arcs built on rifted continental fragments, which underwent multiple episodes of crustal thickening and metamorphism during orogenesis (e.g. Berman et al. 2007; Dusel-Bacon et al. 2002; Foster et al. 1985; Hansen & Dusel-Bacon 1998; Monger & Price 2002; Murphy et al. 2006). The Cordillera is still an active orogen, with most of the present-day deformation concentrated on the western and eastern margins of the Cordillera (e.g. Leonard et al. 2007; Mazzotti et al. 2008; Mazzotti & Hyndman 2002).

The Canadian Cordillera is studied by geologists and geophysicists around the world, since it provides a window into a myriad of geologic processes and hosts many important ore deposits due to its protracted tectonic history (e.g. Allan et al. 2013; Monger & Price 2002; Nelson et al. 2013). Many recent geophysical studies focus on characterizing the present-day lithosphere of the Canadian Cordillera and using these constraints to model past and present lithospheric-scale processes motivated by the large contrast in lithospheric properties between the hot and thin Cordilleran lithosphere and cold and thick lithosphere of the adjacent North American craton (e.g. Audet et al. 2007; Bao et al. 2014; Currie et al. 2008; Lewis et al. 2003;

McLellan et al. 2018; Schaeffer & Lebedev 2014). Numerous models have been proposed for the evolution of the lithosphere and source of uniform heat across the orogen in the Canadian Cordillera and similar tectonic settings. These models include the advection of heat by large convection cells in the asthenosphere caused by the downward motion of a subducting slab (e.g. Finzel et al. 2015) or the delamination of the once thickened Cordilleran lithosphere (e.g. Bao et al. 2014; Levander et al. 2011; Ranalli et al. 1989). Alternatively, present-day Cordilleran temperatures are maintained by vigorous small-scale convection in the upper asthenosphere triggered by a subducting slab or asthenospheric convection along the sharp edge of the cratonic lithosphere (e.g. Currie & Hyndman 2006; Hardebol et al. 2012).

These lithospheric-scale processes are often modeled based on constraints from geophysical data, however a wealth of information on these processes can be extracted from geological data, since they are interconnected with surface and near-surface processes such as uplift, erosion, and tectonic denudation. For instance, the gravitational collapse of orogens is expressed on the surface as widespread extension and normal faulting and the rapid exhumation of deep-seated metamorphic core complexes (e.g. Dewey 1988; Jolivet & Brun 2010; Rey et al. 2001), caused by an excess of gravitational potential energy after crustal thickening, resulting in the lateral flow of the crust (e.g. Dewey 1988). In convergent settings, the localization of surface deformation and uplift of orogens and subsequent preferential erosion of the uplifted portions can be influenced by the strength and geometry of a subducting slab beneath the mountain belt (Bendick and Ehlers 2014). Furthermore, slab detachment or retreating delamination of weak lithosphere below an orogen result in the migration of surface deformation and uplift contemporaneous with the detachment, which in turn results in increased erosion rates in the uplifted areas, and perhaps a shift in the regional climate,

affecting the pattern of precipitation-driven erosion (e.g. Fox et al. 2015; Krystopowicz & Currie 2013). Alternatively, delamination of strong lithosphere is modeled to result in the uplift of the entire orogen, only after the removal of the lithosphere (Krystopowicz & Currie, 2013). Erosion through a combination of fluvial, glacial and mass wasting processes has also been proposed as a catalyst for the localization of deformation and uplift in mountain belts (Koons et al. 2002; Molnar & England 1990; Simpson 2004; Willett et al. 2009; Zeitler et al. 2001), therefore the topographic evolution of many orogens is likely due to positive feedback mechanisms between surface and tectonic processes (e.g. Koons et al. 2013; Reiners & Brandon 2006; Thiede et al. 2004). Thus, studying the timing and patterns of surface processes as well as the present subsurface conditions of the lithosphere contributes to identifying and modeling geodynamic processes. The goal of this thesis is 1) characterizing Mesozoic-Cenozoic surface and shallow subsurface processes of Canadian Cordilleran crust and 2) characterizing present geophysical properties of Canadian Cordilleran crust derived from aeromagnetic anomalies, providing useful constraints for the geodynamic evolution of the Canadian Cordillera.

Chapters 2 and 3 of this thesis are two self-contained scientific articles prepared to be submitted to journals. Chapter 2 will be submitted to *Lithosphere* and Chapter 3 will be submitted to *Journal of Geophysical Research*, and the articles are formatted according to their respective journal's guidelines. I am the main author of both papers, which were modified according to comments from my co-supervisors David Schneider and Pascal Audet. Chapter 4 is the conclusion chapter of the thesis, outlining the contributions of both articles to the understanding of modern-day Cordilleran crust and its past crustal processes.

Chapter 2 presents the results of a low-temperature thermochronology study in west-central Yukon, in the metamorphic hinterland of the northern Canadian Cordillera, and was done in close collaboration with David Schneider. The numerical models and interpretations were discussed with Pascal Audet. Samples chosen for analysis are from the archives of the Geological Survey of Canada, facilitated by Nancy Joyce. The analyses were done by Élise Cossette, Cassandra Powell and Meghan Moher using the thermochronology laboratory facilities at the University of Texas-Austin and University of Colorado-Boulder, and I undertook the numerical modeling and interpretations of the dataset. This study focuses on an area of approximately 200 × 100 km of the Yukon Tanana Terrane, formed by a series of arcs that record multiple crustal thickening and metamorphic events between their accretion to the Laurentian margin in the Permian-Triassic to mountain-building in the Triassic-Cretaceous (e.g. Beranek & Mortensen 2011; Colpron et al. 2007; Nelson et al. 2013). Previous work has been done on the Permian-Jurassic tectonic history using geochronometers and high temperature thermochronometers (e.g. Beranek & Mortensen 2011; Colpron et al. 2007; Nelson et al. 2013). Chapter 3 builds on these previous studies by resolving the Cretaceous exhumation history of the shallow crust using (U-Th)/He thermochronology.

Apatite and zircon (U-Th)/He thermochronology is based on the production of radiogenic ^{4}He, through the α-decay of ^{238}U, ^{235}U and ^{232}Th and ^{147}Sm (Farley 2002; Harrison & Zeitler 2005), and how retentive of ^{4}He the apatite and zircon are once it is formed. Both zircon and apatite have a temperature range where the grains will retain a fraction of the ^{4}He, and the retentivity increases as temperatures decrease, until the grains start to retain all of the produced daughter product below a certain temperature. In general, zircon is partially retentive between 140 and 210 °C (Guenthner et al. 2013; Reiners 2002; Reiners et al. 2004; Stockli

2005; Wolfe & Stockli 2010) and apatite is partially retentive between 35 and 90 °C (Farley 2000; Flowers et al. 2009; Shuster et al. 2006; Stockli et al. 2000), and this temperature range is referred to here as the partial retention zone (PRZ). Using the (U-Th)/He ages as simply a "cooling age" is misleading, since different samples may spend a different amount of time within the PRZ, and the retentivity of the grain also depends on grain-specific parameters such as grain size and radiation damage from the ejection of α particles, thus the decay of U, Th and Sm to ^{4}He cannot be directly related to time. However, with the use of numerical models, and the current knowledge of ^{4}He diffusion kinetics within zircon and apatite, the timing and rate of cooling within the PRZ may be resolved. The dataset in Chapter 2 includes ^{4}He ages from zircon and apatite (ZHe and AHe, respectively), and can therefore resolve the thermal histories within a wide temperature range which approximately corresponds to the shallow crust (Currie & Hyndman 2006).

Knowing the rate and spatial pattern of cooling of the upper crust is useful for studying surface processes such as erosion and topographic development. A key assumption when studying past surface and near-surface processes using low-temperature thermochronology is the crustal thermal model, since surface temperatures and geothermal gradients allow the temperatures from thermochronology models to be converted into depths, and cooling rates into exhumation rates. However, since multiple factors can affect cooling rates, and multiple exhumation mechanisms operate at similar rates, cooling rates alone cannot distinguish between exhumation mechanisms. The spatial pattern of cooling and exhumation can give clues on the exhumation mechanisms. For example, if the change in (U-Th)/He ages is subtle within the study area, this may imply climate-driven exhumation, for example an increase in precipitation focused on one area, the location of which is often related to the regional

geomorphology (Willett et al. 1999). A marked change in (U-Th)/He ages or very different exhumation rates between two directly adjacent areas may imply tectonic exhumation, for example by tectonic denudation, where normal faulting rapidly exposes the underlying footwall. Exhumation by thrust faulting implies an increase in topography due to thickening, and the uplifted regions are preferentially eroded (Reiners & Brandon 2006). Low-temperature thermochronology may therefore be used to locate faults, or estimate the timing and rate of faulting, and has also been applied at larger scales, for example to show the overall movement of material showing the propagation of an orogenic front (Reiners & Brandon 2006).

Since the sampling density in Chapter 2 is relatively low for a thermochronology study, with 25 samples collected over an area of ~20 000 km^2, the study area was divided into five crustal blocks. The thermochronology models resolve the general thermal history that best represents each crustal block, although there may be smaller-scale cooling patterns within each of them. In some areas, the exact exhumation mechanisms could not be determined because of the scale of the study and poor constraints on faults in the area. Consequently, possible exhumation mechanisms are proposed, and smaller areas are found where future smaller-scale thermochronology studies may resolve the exhumation mechanisms that operate on the scale of the study presented in Chapter 2. Moreover, the study area in Chapter 2 is much larger than most other geological studies in Yukon, which highlights some issues with previously proposed tectonic models that were based on local studies. The large scale and low sampling density of this study makes resolving these issues challenging, but brings them to light nonetheless.

The article in Chapter 3 covers a much larger area with the goal of improving the constraints on modern geothermal gradients in the crust throughout the Canadian Cordillera and part of the adjacent craton. I worked closely with my co-supervisor Pascal Audet for this study, consulting with David Schneider when relating the results to the regional geology. As mentioned above, the contrast in lithospheric properties between the Canadian Cordillera and the adjacent North American craton has motivated many geophysical studies, and multiple geodynamic models have been proposed to explain the mechanisms behind the hot and thin Cordilleran lithosphere and contrasting cold and thick cratonic lithosphere. Therefore, the study area in Chapter 3 was expanded beyond the Canadian Cordillera to include the Canadian Shield. In this chapter, crustal temperatures in western Canada are characterized by estimating the depth to the Curie temperature of crustal rocks from a spectral analysis of magnetic anomaly data. The anomaly grid is a subset of NAMAG (2002), an aeromagnetic compilation grid that covers Canada, U.S.A., and Mexico, which is a useful and easily accessible dataset for characterizing the North American Cordillera and craton.

Aeromagnetic surveys are some of the oldest geophysical methods, with the earliest applications being mineral exploration and bedrock mapping (Hood 1992). The geomagnetic field can be divided into two categories; the core (or main) field and the crustal field. The former is generated by movements within the fluid outer core, while the latter reflects geological sources in the crust, mainly caused by highly magnetic minerals such as magnetite and titanomagnetite (Blakely 1995 and references therein). Before extracting information on the subsurface geology, the contributions of the crustal field must be isolated from the total magnetic field. This is done by subtracting the core field (or in most cases, a regional field from the International Geomagnetic Reference Field model) from the total magnetic field, the

result of which is referred to as crustal magnetic anomalies. The crustal field only reflects the subsurface geology to a certain depth, since ferrimagnetic minerals such as magnetite and titanomagnetite become paramagnetic (i.e. very weakly magnetic) at a certain temperature, called the Curie temperature. The Curie temperature varies between minerals, but is often assumed to be ~580 °C for bulk rocks since this is the Curie temperature of magnetite, one of the main minerals contributing to the crustal magnetic field (Blakely 1995). The depth to the bottom of the crustal source may be calculated using the statistical properties of the magnetic crust, and since this depth corresponds to the Curie temperature, geothermal gradients may be inferred. Methods of estimating the depth of the magnetic crust using the statistical properties of magnetic anomalies started to develop in the early 1970s by Spector & Grant (1970) and Treitel et al. (1971). These studies demonstrated how to calculate the depth of the base of the magnetic crust by analyzing the shape of the power spectra of the magnetic anomalies. Spector & Grant (1970) used a statistical model where the subsurface magnetic crust was represented by an ensemble of an infinite number of blocks of different dimensions, which all have the same statistical properties. An alternate model was proposed by Blakely (1988, 1995), who suggested a method of calculating the depth to the bottom of the magnetic crust using the statistical properties of a single randomly magnetized layer, where the depth to the top and bottom varies laterally. These models assume a randomly magnetized crust, and this became an often-used assumption for calculating depths to the base of the magnetized crust (Blakely 1988; Ross et al. 2006; Tanaka et al. 1999). However, in recent years, statistical models for a fractal distribution of magnetization have been shown to be more representative of the statistical properties of the crust, where the magnetization is spatially correlated (e.g. Bouligand et al. 2009; Li et al. 2017; Maus et al. 1997; Pilkington et al. 1994; Pilkington &

Todoeschuck 1993). Therefore, in this study, I use a statistical model in which the magnetized crust is represented by a single layer in the subsurface with a varied depth and thickness, and where the magnetization follows a fractal distribution to avoid systematic errors in the estimation of the Curie depth.

Inferring crustal temperatures using magnetic anomalies is advantageous because it gives independent constraints on crustal temperatures over the entire magnetic anomaly grid, improving on geothermal gradients based only on heat flow measurements, which are sparse and unevenly distributed (e.g. Lewis et al. 2003). The Curie depths presented in Chapter 3 are important for characterizing thermal models for the crust in western Canada, which are an essential part of geodynamic models.

References

Allan, M.M., Mortensen, J.K., Hart, C.J.R., Bailey, L.A., Sanchez, M.G., Ciolkiewicz, McKenzie, G.G., and Creaser, R.A., 2013, Magmatic and metallogenic framework of west-central Yukon and east-central Alaska *in* Colpron, M., Bissig, T., Rusk, B.G., and Thompson, J.H.F., eds., Tectonics, Metallogeny, and Discovery: The North American Cordillera and similar accretionary settings: Society of Economic Geologists Special Publication 17, p. 111–168, doi: 10.1017/CBO9781107415324.004.

Audet, P., Jellinek, A.M., and Uno, H., 2007, Mechanical controls on the deformation of continents at convergent margins: Earth and Planetary Science Letters, v. 264, p. 151–166, doi: 10.1016/j.epsl.2007.09.024.

Bao, X., Eaton, D.W., and Guest, B., 2014, Plateau uplift in western Canada caused by lithospheric delamination along a craton edge: Nature Geoscience, v. 7, p. 830–833, doi: 10.1038/NGEO2270.

Bendick, R., and Ehlers, T. A., 2014, Extreme localized exhumation at syntaxes initiated by subduction geometry. Geophysical Research Letters, v. 41, p. 5861–5867.

Beranek, L.P., and Mortensen, J.K., 2011, The timing and provenance record of the Late Permian Klondike orogeny in northwestern Canada and arc - continent collision along western North America: Tectonics, v. 30, p. 1–23, doi: 10.1029/2010TC002849.

Berman, R.G., Ryan, J.J., Gordey, S.P., and Villeneuve, M., 2007, Permian to Cretaceous polymetamorphic evolution of the Stewart River region, Yukon-Tanana terrane, Yukon, Canada: P-T evolution linked with in situ SHRIMP monazite geochronology: Journal of meramorphic geology, vol. 25, p. 803–827, doi: 10.1111/j.1525-1314.2007.00729.x.

Blakely, R.J., 1988, Curie temperature isotherm analysis and tectonic implications of aeromagnetic data from Nevada: Journal of Geophysical Research, v. 93, p. 11817–11832, doi: 10.1029/JB093iB10p11817.

Blakely, R. J., 1995, Potential Theory in Gravity and Magnetic Applications: Cambridge, U.K., Cambridge University Press, 441 p.

Bouligand, C., Glen, J.M.G., and Blakely, R.J., 2009, Mapping Curie temperature depth in the western United States with a fractal model for crustal magnetization: Journal of Geophysical Research: Solid Earth, v. 114, p. 1–25, doi: 10.1029/2009JB006494.

Colpron, M., Nelson, J. L., and Murphy, D.C., 2007, Northern Cordilleran terranes and their interactions through time: GSA Today, v. 17, p. 4–10, doi: 10.1130/GSAT01704-5A.1.

Currie, C.A., Huismans, R.S., and Beaumont, C., 2008, Thinning of continental backarc lithosphere by flow-induced gravitational instability: v. 269, p. 436–447, doi: 10.1016/j.epsl.2008.02.037.

Currie, C.A., and Hyndman, R.D., 2006, The thermal structure of subduction zone back arcs: Journal of Geophysical Research: Solid Earth, v. 111, p. 1–22, doi: 10.1029/2005JB004024.

Dewey, J.F., 1988, Extensional collapse of orogens: Tectonics, v. 7, p. 1123–1139, doi: 10.1029/TC007i006p01123.

Dusel-Bacon, C., Lanphere, M.A., Sharp, W.D., Layer, P.W., and Hansen, V.L., 2002, Mesozoic thermal history and timing of structural events for the Yukon-Tanana Upland, east-central Alaska: $^{40}Ar/^{39}Ar$ data from metamorphic and plutonic rocks: Canadian Journal of Earth Sciences, v. 1051, p. 1013–1051, doi: 10.1139/E02-018.

England, P., and Molnar, P., 1990, Surface uplift, uplift of rocks, and exhumation of rocks:

Geology, v. 18, p. 1173-1177.

Farley, K.A., 2002, (U-Th)/He Dating: Techniques, Calibrations, and Applications: Reviews in Mineralogy and Geochemistry, v. 47, p. 819–844, doi: 10.2138/rmg.2002.47.18.

Farley, K.A., 2000, Helium diffusion from apatite: General behavior as illustrated by Durango fluorapatite: Journal of Geophysical Research: Solid Earth, v. 105, p. 2903–2914, doi: 10.1029/1999JB900348.

Finzel, E.S., Flesch, L.M., Ridgway, K.D., Holt, W.E., and Ghosh, A., 2015, Surface motions and intraplate continental deformation in Alaska driven by mantle flow: Geophysical Research Letters, p. 4350–4358, doi: 10.1002/2015GL063987.Received.

Flowers, R.M., Ketcham, R.A., Shuster, D.L., and Farley, K.A., 2009, Apatite (U-Th)/He thermochronometry using a radiation damage accumulation and annealing model: Geochimica et Cosmochimica Acta, v. 73, p. 2347–2365, doi: 10.1016/j.gca.2009.01.015.

Foster, L., Cushing, W., Keith, E.C., and Laird, J., 1985, Early Mesozoic tectonic history of the boundary area, east-central Alaska: Geophysical Research Letters, v. 12, p. 553–556.

Fox, M., Herman, F., Kissling, E., and Willett, S.D., 2015, Rapid exhumation in the Western Alps driven by slab detachment and glacial erosion: Geology, v. 43, p. 379–382, doi: 10.1130/G36411.1.

Guenthner, W.R., Reiners, P.W., Ketcham, R.A., Nasdala, L., and Giester, G., 2013, Helium diffusion in natural zircon: radiation damage, anisotropy, and the interpretation of zircon (U-Th)/He thermochronology: American Journal of Science, v. 313, p. 145–198, doi: 10.2475/03.2013.01.

Hansen, V.L., and Dusel-Bacon, C. 1998, Structural and kinematic evolution of the Yukon-Tanana upland tectonites, east-central Alaska: A record of late Paleozoic to Mesozoic crustal assembly: GSA Bulletin, v. 110, p. 211–230.

Hardebol, N.J., Pysklywec, R.N., and Stephenson, R., 2012, Small-scale convection at a continental back-arc to craton transition: Application to the southern Canadian Cordillera: Journal of Geophysical Research: Solid Earth, v. 117, p. 1–18, doi: 10.1029/2011JB008431.

Harrison, T.M., and Zeitler, P.K., 2005, Fundamentals of Noble Gas Thermochronometry: Reviews in Mineralogy and Geochemistry, v. 58, p. 123–149, doi: 10.2138/rmg.2005.58.5.

Hood, P., 1992, Survey parameters and availability of low-level aeromagnetic data for geomagnetic field modelling, *in* Langel, R.A. and Baldwin, R.T., eds., NASA Conference Publication 3153, Types and Characteristics of Data for Geomagnetic Field Modeling, p. 249–286.

Jolivet, L., and Brun, J.-P., 2010, Cenozoic geodynamic evolution of the Aegean: International Journal of Earth Sciences, v. 99, p. 109–138, doi: 10.1007/s00531-008-0366-4.

Koons, P. O., Zeitler, P. K., Chamberlain, C. P., Craw, D., and Meltzer, A. S., 2002, Mechanical links between erosion and metamorphism in Nanga Parbat, Pakistan Himalaya: American Journal of Science, v. 302, p. 749–773.

Koons, P.O., Zeitler, P.K., and Hallet, B., 2013, Tectonic aneurysms and mountain building, *in*: Shroder, J., Owen, L.A., eds., Treatise on Geomorphology, vol. 5. Academic Press, San Diego, CA. 32 pp.

Krystopowicz, N.J., and Currie, C.A., 2013, Crustal eclogitization and lithosphere delamination in orogens: Earth and Planetary Science Letters, v. 361, p. 195–207, doi: 10.1016/j.epsl.2012.09.056.

Leonard, L.J., Hyndman, R.D., Mazzotti, S., Nykolaishen, L., Schmidt, M., and Hippchen, S., 2007, Current deformation in the northern Canadian Cordillera inferred from GPS measurements: Journal of Geophysical Research: Solid Earth, v. 112, p. 1–15, doi: 10.1029/2007JB005061.

Levander, A., Schmandt, B., Miller, M.S., Liu, K., Karlstrom, K.E., Crow, R.S., Lee, C.T.A., and Humphreys, E.D., 2011, Continuing Colorado plateau uplift by delamination-style convective lithospheric downwelling: Nature, v. 472, p. 461–465, doi: 10.1038/nature10001.

Lewis, T.J., Hyndman, R.D., and Flück, P., 2003, Heat flow, heat generation, and crustal temperatures in the northern Canadian Cordillera: Thermal control of tectonics: Journal of Geophysical Research: Solid Earth, v. 108, doi: 10.1029/2002JB002090.

Li, C.F., Lu, Y., and Wang, J., 2017, A global reference model of Curie-point depths based on EMAG2: Scientific Reports, v. 7, p. 1–9, doi: 10.1038/srep45129.

Maus, S., Gordon, D., and Fairhead, D., 1997, Curie-temperature depth estimation using a self-similar magnetization model: Geophysical Journal International, v. 129, p. 163–168, doi: 10.1111/j.1365-246X.1997.tb00945.x.

Mazzotti, S., and Hyndman, R.D., 2002, Yakutat collision and strain transfer across the northern Canadian Cordillera: Geology, v. 30, p. 495–498, doi: 10.1130/0091-7613(2002)030<0495:YCASTA>2.0.CO;2.

Mazzotti, S., Leonard, L.J., Hyndman, R.D., and Cassidy, J.F., 2008, Tectonics, Dynamics,

and Seismic Hazard in the Canada-Alaska Cordillera: Active Tectonics and Seismic Potential of Alaska, p. 297–319, doi: 10.1029/179GM17.

McLellan, M., Schaeffer, A.J., and Audet, P., 2018, Structure and fabric of the crust and uppermost mantle in the northern Canadian Cordillera from Rayleigh-wave tomography: Tectonophysics, v. 725, p. 28–41, doi: 10.1016/j.tecto.2018.01.011.

Molnar, P., and England, P. (1990). Late Cenozoic uplift of mountain ranges and global climate change: chicken or egg?: Nature, v. 346, p. 29–34.

Monger, J., and Price, R., 2002, The Canadian Cordillera: Geology and Tectonic Evolution: CSEG Recorder, v. 27, p. 17–36, doi: 10.13140/2.1.4483.1520.

Murphy, D. C., Mortensen, J. K., Piercey, S. J., Orchard, M. J., and Gehrels, G. E., 2006, Mid-Paleozoic to early Mesozoic tectonostratigraphic evolution of Yukon-Tanana and Slide Mountain terranes and affiliated overlap assemblages, Finlayson Lake massive sulphide district, southeastern Yukon, *in* Colpron, M., and Nelson, J. L., eds., Paleozoic evolution and metallogeny of pericratonic terranes at the ancient Pacific margin of North America, Canadian and Alaskan cordillera. Geological Association of Canada Special Paper 45, p. 75–105.

Nelson, J.L., Colpron, M., and Israel, S., 2013, The Cordillera of British Columbia, Yukon, and Alaska: Tectonics and Metallogeny *in* Colpron, M., Bissig, T., Rusk, B.G., and Thompson, J.H.F., eds., Tectonics, Metallogeny, and Discovery: The North American Cordillera and similar accretionary settings: Society of Economic Geologists Special Publication 17, p. 53–109, doi: 10.1017/CBO9781107415324.004.

Pilkington, M., Gregotski, M.E., and Todoeschuck, J.P., 1994, Using fractal crustal magnetization models in magnetic interpretation: Geophysical Prospecting, v. 42, p.

677–692, doi: 10.1111/j.1365-2478.1994.tb00235.x.

Pilkington, M., and Todoeschuck, J.P., 1993, Fractal magnetization of continental crust: Geophysical Research Letters, v. 20, p. 627–630, doi: 10.1029/92GL03009.

Ranalli, G., Brown, R. L., & Bosdachin, R. (1989). A geodynamic model for extension in the Shuswap core complex, southeastern Canadian Cordillera. Canadian Journal of Earth Sciences, 26, 1647–1653. https://doi.org/10.1139/e89-140

Reiners, P.W., 2002, (U-Th)/He chronometry experiences a renaissance: EOS Transactions American Geophysical Union, v. 83, p. 21–27, doi: 10.1029/2002EO000012.

Reiners, P.W., and Brandon, M.T., 2006, Using Thermochronology To Understand Orogenic Erosion: Annual Review of Earth and Planetary Sciences, v. 34, p. 419–466, doi: 10.1146/annurev.earth.34.031405.125202.

Reiners, P.W., Spell, T.L., Nicolescu, S., and Zanetti, K.A., 2004, Zircon (U-Th)/He thermochronometry: He diffusion and comparisons with $^{40}Ar/^{39}Ar$ dating: Geochimica et Cosmochimica Acta, v. 68, p. 1857–1887, doi: 10.1016/j.gca.2003.10.021.

Rey, P., Vanderhaeghe, O., and Teyssier, C., 2001, Gravitational collapse of the continental crust : definition, regimes and modes: v. 342, p. 435–449.

Ross, H.E., Blakely, R.J., and Zoback, M.D., 2006, Testing the use of aeromagnetic data for the determination of Curie depth in California: Geophysics, v. 71, p. L51–L59, doi: 10.1190/1.2335572.

Schaeffer, A.J., and Lebedev, S., 2014, Imaging the North American continent using waveform inversion of global and USArray data: Earth and Planetary Science Letters, v. 402, p. 26–41, doi: 10.1016/j.epsl.2014.05.014.

Shuster, D.L., Flowers, R.M., and Farley, K.A., 2006, The influence of natural radiation

damage on helium diffusion kinetics in apatite: Earth and Planetary Science Letters, v. 249, p. 148–161, doi: 10.1016/j.epsl.2006.07.028.

Simpson, G., 2004, Role of river incision in enhancing deformation: Geology, v. 32, 341–344.

Spector, A., and Grant, F.S., 1970, Statistical models for interpreting aeromagnetic data: Geophysics, v. 35, p. 293–302.

Stockli, D.F., Farley, K.A., and Dumitru, T.A., 2000, Calibration of the apatite (U-Th)/He thermochronometer on an exhumed fault block, White Mountains, California: Geology, v. 28, p. 983–986, doi: 10.1130/0091-7613(2000)28<983:COTAHT>2.0.CO;2.

Tanaka, A., Okubo, Y., and Matsubayashi, O., 1999, Curie point depth based on spectrum analysis of the magnetic anomaly data in East and Southeast Asia: Tectonophysics, v. 306, p. 461–470, doi: 10.1016/S0040-1951(99)00072-4.

Thiede, R.C., Bookhagen, B., Arrowsmith, J.R., Sobel, E.R., and Strecker, M.R., 2004, Climatic control on rapid exhumation along the Southern Himalayan Front: Earth and Planetary Science Letters, v. 222, p. 791–806, doi: 10.1016/j.epsl.2004.03.015.

Treitel, S., Clement, W.G., and Kaul, R.K., 1971, The Spectral Determination of Depths to Buried Magnetic Basement Rocks: Geophysical Journal of the Royal Astronomical Society, v. 24, p. 415–428, doi: 10.1111/j.1365-246X.1971.tb02187.x.

Willett, S.D., 1999, Orogeny and orography: The effects of erosion on the structure of mountain belts: Journal of Geophysical Research: Solid Earth, v. 104, p. 28957–28981, doi: 10.1029/1999JB900248.

Wolfe, M.R., and Stockli, D.F., 2010, Zircon (U-Th)/He thermochronometry in the KTB drill hole, Germany, and its implications for bulk He diffusion kinetics in zircon: Earth

and Planetary Science Letters, v. 295, p. 69–82, doi: 10.1016/j.epsl.2010.03.025.

Zeitler, P. K., Meltzer, A. S., Koons, P. O., Craw, D., Hallet, B., Chamberlain, C. P., Kidd, W.S.F., Park, S.K., Seeber, L., Bishop, M., Shroder, J., 2001, Erosion, Himalayan geodynamics, and the geomorphology of metamorphism: GSA Today, v. 11, 4–9.

Chapter 2.

Widespread Cretaceous exhumation of the Yukon Tanana Terrane, west-central Yukon: upper crustal tectonism resolved by (U-Th)/He thermochronology

Élyse Gaudreau, David A. Schneider, Pascal Audet

Abstract

The complex patchwork of terranes that make up the northern Canadian Cordillera is characterized by local extension and exhumation, with orogen-parallel strike-slip motion and widespread orogen-normal compression and during the Cretaceous. Important tectonic events often result in rapid exhumation of deep-seated rocks, the timing of which is resolvable through numerical modeling of low-temperature thermochronology data. In this study, the timing and rate of exhumation of different crustal blocks within the Yukon Tanana Terrane (YTT) in the Canadian Cordillera is determined using low-temperature (U-Th)/He thermochronology. Previous studies using $^{40}Ar/^{39}Ar$ thermochronology have outlined the Jurassic cooling history of the YTT to upper crustal temperatures. In this study, numerical modeling of the zircon and apatite thermochronology data indicates that the YTT remained in the upper crust until the late-Early Cretaceous when the structurally higher Mississippian rocks cooled relatively rapidly (~10 °C/m.y.) to surface temperatures, followed by the rapid exhumation of a late-Early Cretaceous metamorphic core complex from beneath the YTT. The structurally lower Permian rocks however began exhuming 30 m.y. later in the Late Cretaceous. The differential exhumation of the structural domains likely requires tectonically-driven exhumation, rather than climate-influenced erosion rates. These results mark an older

low-temperature exhumation history compared to the Cordillera in Alaska and British Columbia, which define a dominant Eocene signature.

2.1. Introduction

Despite the relatively high elevation of the Canadian Cordillera, the orogenic lithosphere is more than 100 km thinner than the adjacent cratonic lithosphere and has a flat and shallower Moho, reflecting a contrast in thermal regime and physical characteristics between the stable craton and mountainous Cordilleran region (Bao et al. 2014; Hyndman and Currie 2011). Not surprisingly, the structural and exhumation history is very different between the two regions, as well. Models commonly invoked to explain the present-day lithospheric structure of the Cordillera involve down-welling and delamination of the lithosphere, resulting in rapid, large-scale plateau uplift and an increase in magmatic activity (Currie et al. 2008; DeCelles et al. 2015; Hardebol et al. 2012). The timing and rate of exhumation and cooling of the shallow crust associated with the these lithospheric-scale processes may be estimated using low-temperature thermochronometers such as zircon and apatite fission track and (U-Th)/He dating (e.g. Barnes and Ehlers 2009; Colgan and Henry 2009; Dai et al. 2013; Fan and Carrapa 2014; Herman et al. 2009). To better resolve the cooling and unroofing models for the northern Canadian Cordillera in west-central Yukon Territory, the shallow crustal thermal history of several crustal blocks of the Yukon Tanana Terrane (YTT; **Figure 2.1**) is determined using low-temperature (U-Th)/He thermochronology. Previous investigations established the higher temperature exhumation history of west-central Yukon, documenting Jurassic cooling due to the overthrusting of the terrane onto ancestral North America (e.g. Joyce et al. 2015; Knight et al. 2013). This elaborates on the Jurassic thermal history, and

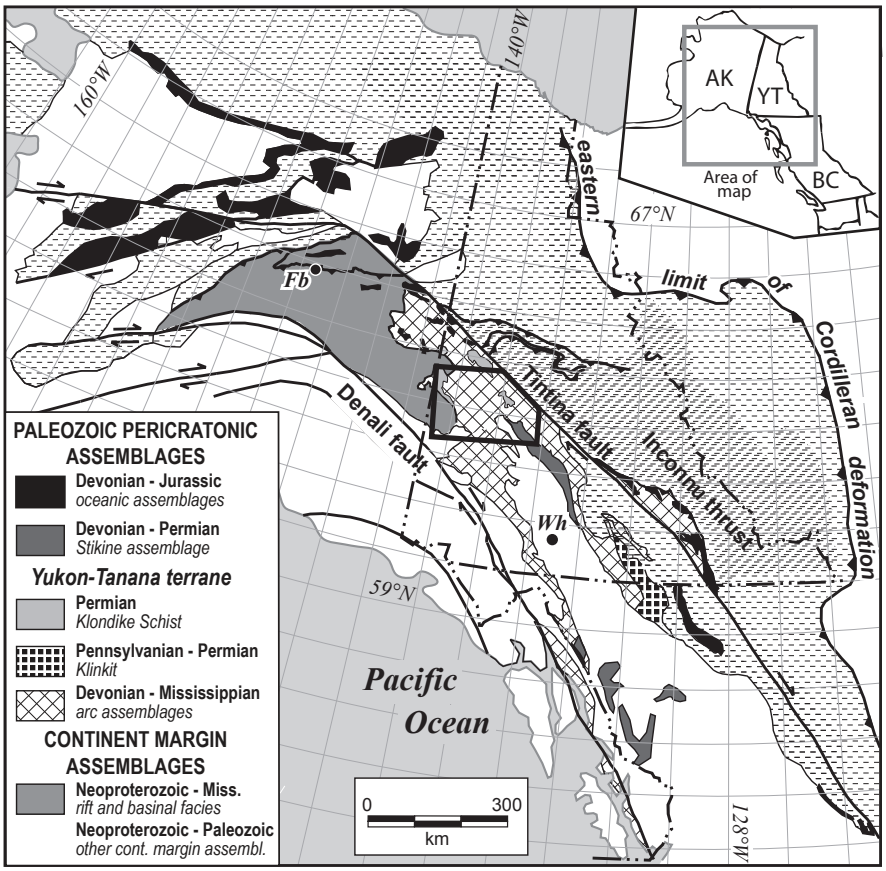

Figure 2.1. Simplified map of the Paleozoic arc and oceanic assemblages in the northern Canadian Cordillera (modified from Knight et al. 2013; Murphy et al. 2006; Silberling et al. 1992; Wheeler & McFeely 1991). The study area is outlined in black. **Fb:** Fairbanks. **Wh:** Whitehorse.

furthermore a proposed a large-scale Cretaceous extensional and exhumation episode (e.g. Staples et al. 2016) is assessed within the context of our new data in order to evaluate the proposed lithospheric-scale processes driving exhumation. The post-Cretaceous thermal history according to our numerical modeling results corroborate several lines of geological, geochronological, and geomorphological evidence that require that the landscape in western and southern Yukon has not witnessed major changes since the Late Cretaceous (Gordey and Ryan 2005; Ryan et al. 2010, 2017; Staples et al. 2016). The post-Cretaceous thermal history of the YTT outlined in this study is in marked contrast with the major Eocene extension and exhumation of the Canadian Cordillera in the neighboring regions of Yukon, Alaska and British Columbia (Bao et al. 2014; Cook et al. 1992; Dusel-Bacon et al. 2016; Enkelmann et al. 2017; O'Sullivan et al. 1997; Parrish et al. 1988). Since the last major phase of exhumation in the YTT is during the Cretaceous, central Yukon appears to have been isolated from the geodynamic processes governing lithospheric thinning and slab window opening that occurred in the Canadian Cordillera throughout the Cenozoic.

2.2. Geologic setting

2.2.1. Tectonic history of the Yukon Tanana Terrane

The Canadian Cordillera is composed of a patchwork of terranes that comprise parts of ancestral North America, the allochtonous peri-Laurentian Intermontane terranes, which includes the YTT, the Insular terranes, as well as other oceanic, arc and accretionary terranes (Colpron et al. 2007). Since our study is focussed on the YTT, we summarize the main structural levels of the terrane and their formation. The YTT was originally part of ancestral

North America's margin (Nelson et al. 2006). The terrane is thought to have rifted from the continental margin in the Devonian-Mississippian, and transitioned between continental arc, back arc and island settings between the Devonian and the Triassic (Nelson et al. 2006, 2013). The structurally lowest assemblage of the YTT in west-central Yukon is the metamorphosed and polydeformed siliciclastic Snowcap assemblage, deposited in a pre-Late Devonian continental margin setting (Piercey and Colpron 2009). The Late Devonian-Early Mississippian Finlayson assemblage is structurally higher, composed of low pressure metavolcanic and metasedimentary rocks (Berman et al. 2007). The Finlayson assemblage was intruded by the c. 355-345 Ma Simpson Range suite, contemporaneous with YTT rifting from the North American margin and the opening of the Slide Mountain Ocean (Nelson et al. 2006). The Snowcap assemblage is overlain by the intermediate to mafic volcanic and volcaniclastic sequences of the 342-269 Ma Klinkit assemblage (Nelson et al. 2006), and the the c. 264-252 Ma volcanic arc material which forms the greenschist facies Klondike schist and the spatially associated Sulphur Creek granites and amphibolite facies orthogneisses (Ryan et al. 2014).

The late Permian (c. 260-239 Ma) was characterized by a convergent tectonic setting, high pressure metamorphism and deformation, resulting in a transposition foliation that is found in most rocks of the YTT that are Permian and older (Beranek and Mortensen 2011; Berman et al. 2007; Gordey and Ryan 2005; Mackenzie et al. 2008; Staples et al. 2014). After subduction of the Slide Mountain Ocean beneath the Yukon Tanana arc by the Middle Triassic, the YTT accreted onto North America via the Late Triassic Inconnu thrust and its equivalents (Beranek et al. 2010; Beranek and Mortensen 2011; Murphy et al. 2006; Nelson et al. 2006). The YTT was thrust northeastward over the North American continental margin

as a thin thrust sheet; within the YTT, the Jurassic was highlighted by NW-SE thrusting and folding in Alaska and Yukon (Dusel-Bacon et al. 2002; Foster et al. 1985; Hansen 1998; Murphy et al. 2006). In west-central Yukon, the NE-dipping Yukon River Shear Zone (YRSZ) was active in the pre-Middle Jurassic as a top-to-ESE shear zone, and juxtaposed contrasting structurally lower rocks of the Klondike assemblage (Klondike schist and Sulphur Creek suite), Finlayson assemblage and Snowcap assemblage against amphibolite facies rocks of the Simpson Range Suite and Finlayson assemblage in the hanging wall (**Figure 2.2**). Regional folding formed dm- to km-scale folds with NW-SE trending axial traces, also possibly folding the YRSZ within a regional-scale synform that is currently dipping shallowly to the southeast (Parsons, pers. comm., 2018; Ryan et al. 2014, Ryan, pers. comm. 2015). The synform model has been used to explain the exposure of the Klondike assemblage to the north and south of the Simpson Range Suite, the rocks on the hanging wall of the YRSZ, however only the southern exposure of the YRSZ has been studied and the exposure of the YRSZ to the north is inferred (**Figure 2.2**; Colpron et al. 2016; Parsons, pers. comm., 2018; Ryan, pers. comm., 2016). After regional folding, the YRSZ was reactivated as a top-to-WNW thrust, likely accommodating a large amount of displacement (Parsons, pers. comm., 2018; Ryan et al. 2014).

The Stewart River and Australia Creek normal faults and dextral strike-slip faults such as the Teslin fault accommodated Cretaceous extension and perhaps crustal thinning (**Figure 2.2**; Gabrielse et al. 2006; Pavlis et al. 1993; Staples et al. 2014, 2016). Many crustal-scale Jurassic thrust faults in west-central Yukon may have also been reactivated as strike-slip and normal faults in the Cretaceous (Ryan et al. 2013), and dextral orogen-parallel fault displacement continued into the Paleogene, resulting in major offset on the crustal-scale

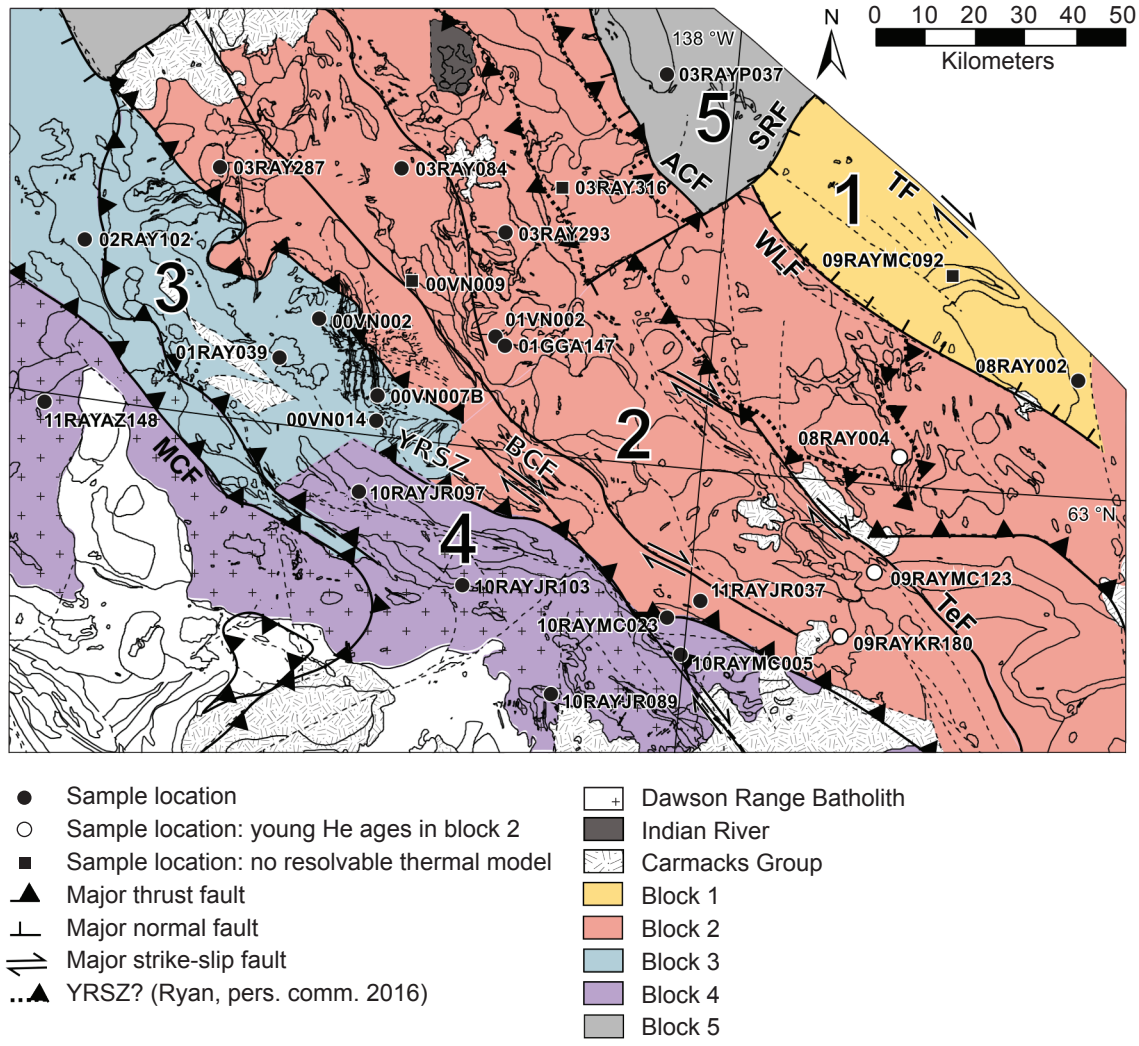

Figure 2.2. Map highlighting the distribution of sample locations and crustal blocks within the northern YTT. White symbols are samples from block 2 where the zircon are reset by Carmacks Group volcanic sequences and square symbols denote samples that could not be resolved with the plausible thermal models discussed in the text. Area south of block 4 (not in color) is the White River Assemblage (Ryan et al. 2014). Major faults after Ryan (pers. comm. 2016) are bold; see Colpron et al. (2016) for fault confidence. **TF:** Tintina fault. **SRF:** Stewart River fault. **ACF:** Australia Creek fault. **WLF:** Willow Lake fault. **TeF:** subfault of the Teslin network. **YRSZ:** Yukon River Shear Zone. **BCF:** Big Creek fault. **MCF:** Moose Creek fault.

Tintina and Denali faults (Gabrielse et al. 2006). The Cretaceous is interpreted as the timing of orogenic collapse (Staples et al. 2016), driving the rapid exhumation of deep-seated rocks and widespread increase in magmatism in the YTT (e.g. Johnston 1999). Late-Early to Late Cretaceous magmatic rocks outcrop in various locations within west-central Yukon such as the Whitehorse plutonic suite, which includes the Dawson Range Batholith located in the southwest portion of the study area (**Figure 2.2**; Johnston 1995). It has also been argued that the Cretaceous was a time of slab window opening or lithospheric delamination that may explain some of the crustal extension, increased magmatism, hot crust and shallow asthenosphere in the Canadian Cordillera (Thorkelson et al. 2011; Thorkelson and Taylor 1989).

2.2.2. Exhumation history in west-central Yukon

The main upper crustal exhumation events recorded in west-central Yukon that have been resolved through previous geochronologic investigations commence in the middle Mesozoic. Widespread Early Jurassic metamorphism and subsequent relatively rapid cooling in the YTT are associated with the obduction of the terrane onto the Laurentian continental margin (Berman et al. 2007; Dusel-Bacon et al. 2002; Joyce et al. 2015; Knight et al. 2013).

Early Jurassic $^{40}Ar/^{39}Ar$ cooling ages are preserved in tectonites of the Willow Lake fault (WLF), constraining the timing of localized YTT exhumation in the footwall of the fault. The hanging wall of the fault is the Reid Lakes complex, a crustal block of the YTT that is structurally higher than the rest of the YTT and has resided at temperatures <300 °C since the Carboniferous (Berman et al. 2007; Knight et al. 2013). The Finlayson assemblage and

Klondike assemblage rocks to the west also record Early to Middle Jurassic cooling (Joyce et al. 2015), yet no obvious structures have been linked to this exhumation event.

Structurally deeper rocks outcrop in a few areas in the study area, interpreted by Staples et al. (2016) as North American continental margin that resided beneath the YTT until the Cretaceous. The Early Cretaceous metamorphic ages and post-Early Cretaceous cooling history in west-central Yukon may be explained by diachronous deformation and metamorphism due to underplating beneath the advancing orogenic wedge (Staples et al. 2016). In this model, the orogenic wedge advances without deforming internally once critical taper is attained. Accreted or underplated material at the toe of the wedge causes it to become unstable, and rocks at depth are buried and metamorphosed, compensated by extension in the upper crust to once again reach the critical taper. This enables high pressure metamorphic core complexes to form at depth and exhume to the surface (Platt 1986; Staples et al. 2016). The Australia Mountain domain (block 5 of **Figure 2.2**) is a metamorphic core complex interpreted to have exhumed during a major extensional episode because of an unstable orogenic wedge, when the geodynamic regime shifted from orogen-normal convergence to orogen-parallel extension in the late-Early Cretaceous (Staples et al. 2016). The overlying YTT is interpreted to have been exhumed and reduced to sea level by this time, allowing for the deposition of the Indian River Formation in marine conditions (Lowey and Hills 1988; Staples et al. 2016). Timing of deposition of the Indian River Formation, constrained to 112-100 Ma by Albian palynomorphs (Lowey and Hills 1988) and felsic ash layers (Mortensen and Dusel-Bacon 2014), is coeval with the timing of rapid exhumation of the Australia Mountain domain (Staples et al. 2016). Also, the Indian River Formation contains metamorphic detritus, and has

therefore been interpreted as a synextensional detachment basin to the Australia Creek fault (Staples et al. 2016).

The c. 70 Ma Carmacks Group volcanic rocks that extruded on to the YTT landscape and other topographic relationships indicate that this area possesses an ancient landscape, relatively unchanged since the Late Cretaceous (Joyce et al. 2015; Gordey and Ryan 2005; Mortensen and Dusel-Bacon 2014; Staples et al. 2016; Ryan et al. 2010, 2017).

2.3. (U-Th-Sm)/He Thermochronology

Determining the temporal and spatial extent of surface processes such as exhumation and cooling may lead to further insight into the deeper mechanisms that invoke large-scale lithospheric structures. The (U-Th)/He system in apatite and zircon is well-suited for studying surface processes, since it is sensitive to a range of temperatures that is aligned with near-surface to upper crustal temperatures. Apatite and zircon (U-Th)/He thermochronology is based on the production of radiogenic ^{4}He, through the α-decay of ^{238}U, ^{235}U and ^{232}Th with a small contribution from ^{147}Sm (Farley 2002; Harrison and Zeitler 2005), and the factors that control its rate of diffusion through the crystal. The closure temperature (T_c) of a crystal (Dodson, 1973) is dependent on the cooling rate (Flowers et al. 2009; Guenthner et al. 2013; Reiners 2005; Stockli et al. 2000), grain size (Farley, 2000) and effective uranium concentration (eU; Flowers et al. 2009; Guenthner et al. 2013; Shuster et al. 2006). Zircon has a nominal T_c of ~180 °C and a PRZ range of 140-210 °C (Guenthner et al. 2013; Reiners 2002; Reiners et al. 2004; Stockli 2005; Wolfe and Stockli 2010) whereas apatite has a nominal T_c of ~70 °C and a PRZ range of 35-90 °C (Farley 2000; Flowers et al. 2009; Shuster

et al. 2006; Stockli et al. 2000). The finite T_c may only be applied to crystals that have cooled rapidly through the PRZ. At temperatures warmer than the PRZ the crystal behaves as an open system and allows the diffusion of ^{4}He. Once the crystal begins to cool into the PRZ it accumulates some ^{4}He and acquires a non-zero date, however it only starts to track calendar time once temperatures drop below the PRZ.

Flowers et al. (2009) reported that older dates are obtained from apatite with increased radiation damage, using effective uranium (eU) concentration as a proxy for damage, when the samples witness protracted cooling through the AHe PRZ. Guenthner et al. (2013) found a similar positive correlation in the ZHe system with the exception that at elevated levels of radiation damage (i.e. high eU), the trend reverses and younger dates are recorded. The inflection from a positive to negative correlation with respect to ZHe date-eU values commonly occurs at 200-250 eU if the sample has a very protracted cooling history (on the order of 1000 m.y.) or can occur at >1000 eU if the sample has spent a shorter amount of time within the PRZ (on the order of 100 m.y. or less). Fractional loss of ^{4}He is controlled by grain size as well, such that larger grains will retain an increased fraction of radiogenic helium, resulting in older dates (Dodson 1973; Reiners and Farley 2001), an effect also amplified by time spent in the PRZ. Our dataset follows semi-quantifiable trends with respect to date-eU as suggested by this theory.

In order to extract more information from a potentially complex dataset, where single crystal dates within a rock sample can vary by tens of millions of years, numerical modeling utilizing the program HeFTy (version 1.9.1; Ketcham 2005) was carried out on all samples applying the apatite radiation damage accumulation and annealing model (RDAAM; Flowers et al. 2009) and zircon radiation damage and accumulation and annealing model (ZRDAAM;

Guenthner et al. 2013). This accounts for the effects that grain size and radiation damage have on diffusion, and reveal probable time-temperature histories rather than a single cooling age. Our approach was to generate both forward and inverse models to assess the consistency of a single possible thermal history to a group of samples. Inverse modeling produces a series of temperature-time paths, generated through a Monte Carlo random search method, which illustrate the plausible thermal histories experienced by the sample. Parameters specific to zircon and apatite which control the range in ages for a given grain, such as eU concentration and grain size, along with user-specified independent temperature-time constraints, such as the timing of known unconformities and other independent geochronology (e.g. U-Pb and $^{40}Ar/^{39}Ar$ ages), are used to help define viable temperature-time paths. Modeled thermal paths generated by HeFTy are compared against the analytical dates and then classified as having a "good" fit or "acceptable" fit (cf. Ketcham 2005 for details on goodness-of-fit). Certain crystals are not used to model time-temperature histories; spuriously old ages with low eU may be due to ^{4}He implantation from neighboring grains or fluid inclusions (Flowers et al. 2009; Ketcham 2012; Spencer et al. 2004; Spiegel et al. 2009) and anomalously young ages may be due to broken grains or mineral zonation (Meesters and Dunai 2002; Murray et al. 2014).

The disadvantage with inverse models is that they are based on data from one sample, therefore it may not represent an entire crustal block, and may yield a wide range of possible thermal histories. Forward models, conversely, test single time-temperature paths and calculates a theoretical distribution of ^{4}He ages as a function of eU. Forward models use possible time-temperature paths as input, and generates date trends that would result from these paths according to diffusion kinetics and the predicted accumulated radiation damage.

Forward modeling was employed to create a series of date-eU curves based on grain sizes (equivalent surface radii; ESR), which cumulatively form an "envelope" (Guenthner et al. 2014). Measured zircon and apatite dates are then compared to these envelopes to assess the fit of the forward model. The use of "envelopes" helps quantify the effects of grain size on partially reset grains and allows for the unraveling of a thermal history with increased confidence.

The analytical portion of the experiments was conducted at the University of Colorado (Boulder, USA) and the University of Texas (Austin, USA). Laboratory procedures are described in detail in the Appendix A1. Archival mineral separates from rocks which have previously been dated for U-Pb geochronology were used to provide a framework for this study (Geological Survey of Canada, unpublished data; Knight et al. 2013). Twenty-four Devonian to Cretaceous granitoids and metagranitoids were selected for thermochronology, with 2-10 zircon and 3-5 apatite analyzed for each sample (**Tables 2.1-2.3**). Granitoids and metagranitoids were analyzed because of the extensive, previously published geochronology and high temperature thermochronology studies on these units that provide useful constraints for numerical models and because of the likelihood of a single age population. Detrital samples were avoided since the provenance is often unknown and may have a protracted pre-depositional thermal history. This adds complexity to the numerical modeling of the post-deposition thermal history, since the samples may have inherited ^{4}He and radiation accumulation damage from their pre-depositional history if the samples have not been buried to temperatures high enough to completely reset the (U-Th)/He system (e.g. Guenthner et al. 2014, 2015; Powell et al. 2016).

Table 2.1. Summary of (U-Th)/He data, YTT, Canada

crustal block	sample	coordinates: UTM (NAD83)	sample description	U-Pb crystallization age (Ma)	ZHe age range (Ma)	AHe age range (Ma)
1	08RAY002	63.2053, -136.54049	unfoliated hbl-granodiorite	342	102 - 141	46 - 51
	09RAYMC092	63.3803, -137.05981	volcanic breccia/qz-rich sandstone	<446	182 - 289	-
2	03RAY084	63.48424, -139.31567	monzogranite	345	138 - 154	53 - 128
	03RAY287	63.44881, -140.04494	foliated monzogranite to alkali feldspar granite	345	63 - 103	60 - 98
	00VN09	62.83494, -137.30240	augen granite	360	81 - 86	66 - 79
	03RAY293	63.38606, -138.8713	tonalitic orthogneiss	355	145 - 178	88 - 282
	01GGA147	63.18417, -138.82639	orthogneiss	355	135 - 140	89 - 93
	01VN002	63.19669, -138.8741	hbl diorite to hbl-qz diorite	345	-	52 - 64
	08RAY004	63.04254, -137.23962	hbl granodiorite orthogneiss	261	70 - 89	56 - 126
	03RAY316	63.47676, -138.66234	augen granite orthogneiss	263	129 - 262	-
	09RAYKR180	62.72004, -137.41599	monzogranite	-	99 - 115	-
	09RAYMC123	62.83494, -137.30240	granodiorite	205	81 - 86	-
3	00VN014	63.0228, -139.31711	bt monzogranite	259	89 - 100	72 - 125
	02RAY102	63.28797, -140.55289	granodiorite	261	95 - 100	-
	01RAY039	63.1164, -139.72384	augen monzongranite	260	90 - 104	68 - 70
	00VN002	63.19042, -139.57583	granite dyke	180	24 - 56	-
	00VN007B	63.07090, -139.33053	ms-qz schist	264	91 - 118	-
4	10RAYJR089	62.56145, -138.51692	breccia clast	101	59 - 73	-
	10RAYJR103	62.7464, -138.90464	gneissic granodiorite	261	60 - 78	10 -12
	11RAYAZ148	62.98926, -140.63564	hbl-bt-ep granodiorite	103	57 - 62	-
	10RAYJR097	62.8907, -139.34373	gneissic monzogranite	262	61 - 75	-
	10RAYMC005	62.65047, -138.02613	augen monzogranite	261	58 - 66	-
	10RAYMC023	62.72097, -138.09735	granodiorite	344	67 - 83	-
	11RAYJR037	62.7615, -137.9737	metaplutonic granodiorite	-	48 - 69	-
5	03RAYP037	61.92579, -137.48953	granodiorite	360	78 - 118	-

Table 2.2. Single-Grain (U-Th)/He analyses of zircon, YTT, Canada

sample	corrected age (Ma)	uncertainty (Ma)	U (ppm)	Th (ppm)	Th/U (Ma)	eU (ppm)	He (nmol/g)	Mass (µg)	ESR (µm)	FT
08RAY002: hbl-granodiorite - block 1. UTM (NAD83): 63.2053, -136.54049*										
z1	141.206	10.018	162.410	177.073	1.090	204.022	121.004	6.443	50.064	0.769
z2	107.345	7.573	168.002	114.706	0.683	194.958	83.615	2.510	42.429	0.734
z3	109.704	7.820	266.244	242.283	0.910	323.181	132.155	2.137	35.597	0.684
z4	102.721	7.209	172.503	99.239	0.575	195.824	84.457	4.053	49.799	0.772
z5	109.542	7.690	127.257	100.526	0.790	150.881	61.526	2.376	35.425	0.683
09RAYMC092: quartz sandstone/volcanic breccia - block 1. UTM (NAD83): 63.3803, -137.05981*										
z1 †	208.268	14.633	724.898	374.259	0.516	812.848	561.185	0.802	27.387	0.603
z2 †	213.326	15.238	236.771	41.111	0.174	246.432	210.437	1.984	40.757	0.728
z3 †	182.943	13.069	324.459	104.866	0.323	349.103	224.296	1.095	30.278	0.640
z4 †	228.086	16.430	125.538	59.044	0.470	139.413	130.049	2.974	43.867	0.743
z5 †	289.479	19.946	226.442	130.075	0.574	257.010	287.601	1.488	36.978	0.699
03RAY084: monzogranite - block 2. UTM (NAD83): 63.48424, -139.31567										
z1	150.761	12.061	218.423	128.098	0.586	247.915	172.811	23.612	78.755	0.846
z2	142.987	11.439	219.822	101.236	0.461	243.132	150.212	8.050	56.901	0.792
z3	154.290	12.343	223.799	104.537	0.467	247.869	167.864	10.558	60.575	0.804
z4	138.466	11.077	200.332	94.087	0.470	221.997	138.753	14.469	69.397	0.827
03RAY287: monzogranite - block 2. UTM (NAD83): 63.44881, -140.04494										
z1	70.732	5.659	244.894	107.399	0.439	269.621	81.924	8.062	56.714	0.792
z2	69.832	5.587	306.066	146.134	0.477	339.712	104.686	12.076	63.796	0.813
z3 †	103.084	8.247	419.103	168.954	0.403	457.999	188.600	3.865	43.573	0.735
z4	63.709	5.097	230.529	100.791	0.437	253.736	64.514	3.546	43.866	0.736
00VN09: granodiorite - block 2. UTM (NAD83): 62.83494, -137.30240										
z3 †	113.981	9.118	264.853	130.596	0.493	294.919	146.351	8.697	59.297	0.800
z4 †	184.750	14.780	3453.783	1491.024	0.432	3797.046	1934.847	1.201	21.177	0.507
03RAY293: tonalitic orthogneiss - block 2. UTM (NAD83): 63.38606, -138.8713										
z1	178.571	14.286	184.007	56.363	0.306	196.985	160.221	16.076	71.086	0.833
z2	156.251	12.500	267.527	90.561	0.339	288.378	190.566	6.816	51.922	0.775
z3	162.156	12.972	229.749	81.780	0.356	248.578	167.048	5.139	48.292	0.759
z4	145.777	11.662	386.635	136.138	0.352	417.979	236.629	3.109	39.756	0.713
01GGA147: orthogneiss - block 2. UTM (NAD83): 63.18417, -138.82639										
z1	137.552	11.004	178.821	70.552	0.395	195.065	120.985	15.354	68.877	0.827
z2	138.416	11.073	206.527	96.185	0.466	228.672	139.501	10.279	61.992	0.808
z3	140.638	11.251	200.759	82.484	0.411	219.749	136.008	10.851	61.422	0.807
z4	135.393	10.831	247.242	90.667	0.367	268.115	154.964	6.806	54.161	0.783
03RAY316: orthogneiss - block 2. UTM (NAD83): 63.47676, -138.66234										
z2 †	262.715	21.017	363.298	180.846	0.498	404.932	352.777	0.989	27.886	0.605
z3 †	204.210	16.337	244.732	117.257	0.479	271.735	203.294	1.699	34.270	0.670
z4 †	129.905	10.392	541.716	376.608	0.695	628.420	282.225	1.227	30.832	0.635
08RAY004: orthogneiss - block 2. UTM (NAD83): 63.04254, -137.23962*										
z1	74.009	5.287	620.242	139.839	0.225	653.104	199.031	5.310	46.497	0.759
z2	89.106	6.331	559.982	166.524	0.297	599.115	229.704	7.436	54.472	0.792
z3	75.079	5.426	797.704	117.061	0.147	825.213	271.040	7.473	58.380	0.806
z4	78.750	5.736	752.643	140.275	0.186	785.607	264.328	4.878	52.936	0.787
z5	70.715	6.628	810.079	146.764	0.181	844.569	252.626	5.095	51.093	0.780
09RAYKR180: monzogranite - block 2. UTM (NAD83): 62.72004, -137.41599										
z1	99.156	7.932	180.225	36.696	0.204	188.673	84.285	15.734	69.048	0.829
z2	111.625	8.930	224.439	77.916	0.347	242.377	123.517	20.398	74.125	0.839
z3	115.233	9.219	219.339	70.838	0.323	235.647	121.964	15.658	67.943	0.825
z4	114.278	9.142	105.920	43.660	0.412	115.972	61.762	26.587	83.554	0.856
09RAYMC123: granodiorite - block 2. UTM (NAD83): 62.83494, -137.30240										
z1	81.495	6.520	83.170	21.055	0.253	88.017	31.419	9.453	60.925	0.807
z2	86.181	6.894	130.565	32.266	0.247	137.996	55.265	27.733	82.782	0.856
00VN014: monzogranite - block 3. UTM (NAD83): 63.0228, -139.31711										
z1*	113.380	8.091	719.840	237.027	0.329	775.541	423.863	41.364	101.075	0.885
z2*	101.303	7.215	973.774	277.032	0.284	1038.877	466.770	11.015	61.420	0.816
z3*	122.833	41.800	647.366	302.334	0.467	718.414	303.983	1.388	29.696	0.632
z4*	113.648	22.913	831.994	243.639	0.293	889.250	385.666	2.202	37.043	0.701
z5*	105.519	11.694	950.651	293.115	0.308	1019.533	445.971	4.071	47.215	0.762
z6	94.984	7.599	365.938	88.596	0.242	386.340	152.144	5.622	48.871	0.764
z7	89.503	7.160	527.888	149.016	0.282	562.213	222.035	11.505	62.895	0.813
z8	93.827	7.506	541.798	135.229	0.250	572.963	218.941	4.934	46.039	0.750
z9	100.646	8.052	532.602	99.505	0.187	555.512	235.383	6.258	51.393	0.775
01RAY039: monzogranite - block 3. UTM (NAD83): 63.1164, -139.72384										

sample	corrected age (Ma)	uncertainty (Ma)	U (ppm)	Th (ppm)	Th/U (Ma)	eU (ppm)	He (nmol/g)	Mass (µg)	ESR (µm)	FT
z1	92.140	7.371	334.627	83.253	0.249	353.798	144.531	11.944	64.149	0.816
z2	104.336	8.347	677.903	142.239	0.210	710.656	316.540	8.011	54.217	0.786
z3	90.934	7.275	389.330	95.574	0.245	411.336	161.989	8.960	57.813	0.798
z4	92.718	7.417	279.139	63.783	0.228	293.826	118.361	9.622	58.514	0.800
00VN002: granite dike - block 3. UTM (NAD83): 63.19042, -139.57583										
z1 †	24.426	1.954	0.030	0.034	1.143	0.038	0.004	27.101	84.927	0.854
z2	56.415	4.513	217.000	84.210	0.388	236.389	62.157	28.204	85.979	0.860
z3	52.804	4.224	92.956	35.925	0.386	101.229	24.075	15.689	70.736	0.831
00VN007B: muscovite-quartz schist - block 3. UTM (NAD83): 63.07090, -139.33053										
z1	110.586	8.847	1093.985	570.744	0.522	1225.422	472.240	1.482	31.194	0.641
z2 †	5.428	0.434	0.873	0.430	0.492	0.972	0.021	3.603	44.874	0.741
z3	118.217	9.457	1950.795	528.986	0.271	2072.597	822.640	1.194	28.584	0.618
z4	91.745	7.340	403.453	228.680	0.567	456.105	148.735	1.623	32.651	0.654
02RAY102: granodiorite - block 4. UTM (NAD83): 63.28797, -140.55289										
z1	95.3	7.62	270.2	56.7	0.21	283.2	113.5	6.16	51.33	0.77
z2	93.1	7.44	403.2	102.7	0.25	426.8	169.9	7.88	54.90	0.79
z3	99.8	7.98	389.6	136.1	0.35	421.0	190.4	17.36	71.57	0.83
10RAYJR089: breccia clast - block 4. UTM (NAD83): 62.56145, -138.51692*										
z1	64.092	4.553	309.677	122.931	0.397	338.566	92.958	7.284	54.160	0.790
z2	63.373	4.500	315.511	121.679	0.386	344.106	89.516	3.185	46.339	0.757
z3	59.453	4.226	376.853	162.870	0.432	415.128	93.142	1.803	36.533	0.696
z4	65.243	4.590	575.484	279.834	0.486	641.244	147.899	1.019	31.501	0.652
z5	69.919	4.803	414.590	219.291	0.529	466.123	126.077	2.046	41.130	0.713
z6	73.679	5.232	525.278	202.940	0.386	572.969	204.423	43.518	108.297	0.893
z7	62.376	4.426	462.572	215.940	0.467	513.318	147.318	15.415	76.367	0.849
z8	69.198	4.881	596.809	384.665	0.645	687.205	203.614	5.620	54.314	0.789
z9	69.273	4.883	781.879	347.521	0.444	863.547	266.453	8.559	64.100	0.821
z10	60.932	4.289	444.451	181.159	0.408	487.023	133.566	9.882	67.661	0.830
10RAYJR103: gneissic granodiorite - block 4. UTM (NAD83): 62.7464, -138.90464*										
z1	77.424	5.516	1300.166	610.834	0.470	1443.712	483.875	6.525	56.330	0.797
z2	73.743	5.173	963.937	305.773	0.317	1035.793	306.531	2.332	42.866	0.740
z3	60.907	4.360	870.962	440.328	0.506	974.439	205.764	1.275	30.391	0.639
z4	78.521	5.610	601.358	224.419	0.373	654.096	204.296	2.878	41.843	0.733
z5	73.820	5.212	987.372	470.068	0.476	1097.838	331.387	3.150	45.744	0.753
11RAYAZ148: granodiorite - block 4. UTM (NAD83): 62.98926, -140.63564*										
z1	62.451	4.445	269.121	91.035	0.338	290.514	78.209	6.765	55.456	0.795
z2	57.019	4.078	327.567	92.747	0.283	349.362	82.221	5.116	47.220	0.762
z3	61.910	4.389	338.447	133.385	0.394	369.793	100.192	7.529	59.242	0.807
z4	61.309	4.316	408.022	137.542	0.337	440.344	117.137	5.739	56.940	0.801
z5	61.759	4.381	291.820	117.690	0.403	319.477	83.527	7.939	51.803	0.781
z6	62.512	4.434	394.985	126.881	0.321	424.802	126.362	29.195	94.856	0.878
z7	59.497	4.213	332.332	109.394	0.329	358.040	97.044	12.465	72.029	0.841
z8	59.454	4.238	397.190	124.612	0.314	426.473	118.838	20.111	85.430	0.865
z9	57.944	4.047	898.914	363.883	0.405	984.426	248.556	5.283	60.545	0.804
10RAYJR097: gneissic monzogranite - block 4. UTM (NAD83): 62.8907, -139.34373										
z1	75.667	6.053	699.958	436.012	0.623	800.346	268.311	10.780	65.094	0.815
z2	75.623	6.050	1228.050	809.995	0.660	1414.554	435.697	4.596	47.000	0.750
z3	69.878	5.590	970.305	878.723	0.906	1172.653	337.494	5.047	49.086	0.757
z4	61.312	4.905	795.883	445.352	0.560	898.413	256.087	26.694	84.689	0.856
10RAYMC005: monzogranite - block 4. UTM (NAD83): 62.65047, -138.02613										
z1	66.674	5.334	746.016	242.524	0.325	801.848	222.267	6.199	49.912	0.767
z2	58.669	4.694	398.925	93.402	0.234	420.428	89.022	1.694	33.350	0.667
z3	68.532	5.483	1229.849	390.277	0.317	1319.694	335.619	2.256	35.740	0.685
z4	63.337	5.067	788.312	252.089	0.320	846.344	196.391	2.067	34.690	0.676
10RAYMC023: granodiorite - block 4. UTM (NAD83): 62.72097, -138.09735										
z1	70.843	5.667	53.630	32.585	0.608	61.133	17.626	4.541	46.864	0.750
z2	67.163	5.373	44.181	20.125	0.456	48.815	13.895	6.538	53.857	0.781
z4	83.889	6.711	48.684	62.104	1.276	63.000	22.030	5.312	51.211	0.765
11RAYJR037: metagranodiorite - block 4. UTM (NAD83): 62.7615, -137.9737										
z1	48.176	3.854	239.138	96.073	0.402	261.255	57.153	16.720	74.039	0.838
z2	48.825	3.906	529.138	185.695	0.351	571.887	124.245	12.602	66.576	0.822
z3	52.042	4.163	706.125	234.940	0.333	760.217	176.061	13.163	66.488	0.822
z4	69.959	5.597	393.592	141.689	0.360	426.212	131.199	9.937	62.713	0.811
03RAYP037: granodiorite - block 5. UTM (NAD83): 61.92579, -137.48953										
z1	93.372	7.470	254.566	28.846	0.113	261.208	110.831	19.127	72.033	0.837

sample	corrected age (Ma)	uncertainty (Ma)	U (ppm)	Th (ppm)	Th/U (Ma)	eU (ppm)	He (nmol/g)	Mass (µg)	ESR (µm)	FT
z3	118.517	9.481	97.356	41.143	0.423	106.832	54.681	7.892	57.119	0.793
z4	78.387	6.271	158.395	14.391	0.091	161.709	57.673	15.610	72.888	0.839

* Sample data acquired at the CU TRaIL facility at the University of Colorado in Boulder (USA).

† Grain not used in (U-Th)/He models

Blocks 2A and 2B refer to the western and eastern samples in block 2, respectively, which have different age-eU signatures

Table 2.3. Single-Grain (U-Th)/He analyses of apatite, YTT, Canada

sample	corrected age (Ma)	uncertainty (Ma)	U (ppm)	Th (ppm)	Th/U (Ma)	eU (ppm)	He (nmol/g)	Mass (µg)	ESR (µm)	FT
08RAY002: hbl-granodiorite - block 1. UTM (NAD83): 63.2053, -136.54049										
a1	46.777	3.275	5.975	13.448	2.251	9.136	1.879	11.035	78.150	0.810
a2	50.999	3.437	25.118	61.099	2.432	39.477	7.657	2.587	49.511	0.700
a3	50.201	7.079	48.365	42.325	0.875	58.312	9.460	0.674	34.178	0.596
03RAY287: monzogranite - block 2. UTM (NAD83): 63.44881, -140.04494										
a1	60.516	15.658	13.747	47.897	3.484	25.003	3.336	0.221	23.368	0.403
a2	61.844	4.651	22.158	40.372	1.822	31.645	6.906	1.089	40.198	0.647
a3	256.047	78.179	2.065	16.036	7.765	5.834	2.770	0.188	20.988	0.333
a4	98.432	13.555	8.447	26.523	3.140	14.680	4.370	0.541	31.746	0.551
03RAY293: tonalitic orthogneiss - block 2. UTM (NAD83): 63.38606, -138.8713										
a1 †	0.283	1.711	2.657	2.499	0.941	3.244	0.003	1.266	41.133	0.662
a2	88.702	13.638	1.088	1.963	1.804	1.550	0.475	1.071	38.731	0.631
a3	126.825	31.255	4.816	7.697	1.598	6.625	2.369	0.422	28.762	0.515
a4	282.144	46.351	2.768	4.527	1.636	3.832	3.333	0.534	31.524	0.557
a5 †	204.549	39.772	1.139	3.135	2.751	1.876	1.147	0.511	31.132	0.545
01VN002: hbl-qtz diorite - block 2. UTM (NAD83): 63.19669, -138.8741										
a1	116.247	16.011	2.526	6.982	2.764	4.167	1.431	0.479	30.593	0.540
a2	60.656	12.388	24.088	54.991	2.283	37.011	6.548	0.508	30.568	0.536
a3	64.476	9.126	2.218	5.621	2.534	3.539	0.764	0.970	37.643	0.616
a4	61.242	8.112	46.721	114.918	2.460	73.727	13.645	0.531	31.711	0.556
a5	52.588	8.185	3.453	12.561	3.637	6.405	1.063	0.718	34.580	0.580
03RAY084: monzogranite - block 2. UTM (NAD83): 63.48424, -139.31567										
a1	81.443	22.049	1.425	3.089	2.168	2.151	0.524	0.535	31.872	0.544
a2	152.747	11.711	0.759	1.025	1.351	1.000	0.622	2.777	54.885	0.740
a3	53.943	6.925	1.178	4.564	3.875	2.250	0.414	1.358	39.363	0.624
a4	128.130	24.790	1.905	6.413	3.366	3.412	1.297	0.588	31.345	0.540
a5 †	455.153	70.652	0.352	4.629	13.142	1.440	2.145	0.933	37.319	0.591
01VN09: granodiorite - block 2. UTM (NAD83): 62.83494, -137.30240										
a1	74.776	5.949	1.455	4.245	2.917	2.453	0.739	2.691	57.320	0.737
a2	177.811	13.763	1.210	3.224	2.664	1.968	1.366	2.099	51.212	0.708
a4	79.626	13.798	18.349	29.649	1.616	25.316	6.113	0.636	31.565	0.554
a5	66.846	12.923	13.523	40.105	2.966	22.947	4.279	0.472	28.873	0.508
01GGA147: orthogneiss - block 2. UTM (NAD83): 63.18417, -138.82639										
a1	32.157	4.722	29.087	14.106	0.485	32.402	3.265	0.610	32.432	0.579
a3	93.608	12.945	29.659	44.110	1.487	40.025	11.530	0.570	32.039	0.565
a4	89.682	12.435	30.416	44.387	1.459	40.847	11.080	0.509	31.178	0.556
08RAY004: orthogneiss - block 2. UTM (NAD83): 63.04254, -137.23962										
a1	191.649	29.587	3.556	14.817	4.167	7.038	4.218	0.668	33.768	0.569
a2	56.473	8.698	44.673	22.950	0.514	50.066	8.559	0.482	30.496	0.556
a3	126.944	26.297	38.619	35.582	0.921	46.981	16.490	0.360	27.392	0.503
a4	88.501	19.247	43.947	26.659	0.607	50.212	13.538	0.636	31.186	0.557
00VN014: monzogranite - block 3. UTM (NAD83): 63.0228, -139.31711										
a1 †	543.585	101.674	0.953	12.893	13.535	3.982	4.946	0.251	24.630	0.411
a2	124.904	27.944	2.818	9.540	3.386	5.060	1.909	0.541	32.531	0.545
a3	89.345	17.999	20.046	51.526	2.570	32.155	8.576	0.553	30.543	0.532
a4	72.556	5.448	6.521	12.218	1.874	9.392	2.582	1.623	45.627	0.686
01RAY039: monzogranite - block 3. UTM (NAD83): 63.1164, -139.72384										
a1 †	511.106	143.816	0.221	3.283	14.863	0.992	1.453	0.474	32.067	0.516
a2	68.358	15.937	6.410	11.908	1.858	9.208	1.944	0.473	32.115	0.550
a3	70.759	16.155	5.757	5.643	0.980	7.083	1.489	0.444	28.602	0.518
10RAYJR103: gneissic granodiorite - block 4. UTM (NAD83): 62.7464, -138.90464										
a1	10.208	0.732	9.992	25.596	2.562	16.007	0.666	5.670	57.871	0.743
a2	12.516	0.878	14.046	34.584	2.462	22.173	1.060	2.275	47.821	0.694
a3	10.632	0.787	7.769	17.614	2.267	11.908	0.505	3.308	53.004	0.723
a4	10.388	0.763	10.471	29.674	2.834	17.444	0.726	4.846	55.283	0.731

† Sample not used in (U-Th)/He models

All data were acquired at the CU TRaIL facility at the University of Colorado in Boulder (USA). Blocks 2A and 2B refer to the western and eastern samples in block 2, respectively, which have different age-eU signatures

2.4. Analytical results

2.4.1. Sample groups

In order to facilitate discussion, we have divided the YTT into distinct sample groups (**Figure 2.2**) that exhibit different low temperature thermal histories. The boundaries between sample groups coincide with mapped faults, except for the southern boundary of block 4, which is an intrusive contact of the Dawson Range Batholith with the White River assemblage. Some of these faults such as the YRSZ and WLF record major displacement prior to the exhumation of upper crustal material currently at the surface, and serve as borders for the fundamental components of the YTT, thus also define the higher temperature history of the terrane. These boundaries were chosen for the low temperature history of the YTT since they mark a structural break between our new (U-Th)/He ages, which is supported by field observations that suggest at least some of these fault zones were reactivated at a later time when the (currently exposed) rocks were in the upper crust (Johnston 1999; Parsons, pers. comm., 2018; Ryan et al. 2013, 2014). These faults also serve as physical boundaries that separate the sample groups based on previously published metamorphic petrology (e.g. Berman et al. 2007), $^{40}Ar/^{39}Ar$ ages (e.g. Hunt and Roddick 1992; Joyce 2002; Joyce et al. 2015; Knight et al. 2013; Staples et al. 2014; Wanless et al. 1978), structural relationships (e.g. Ryan et al. 2014) and aeromagnetic data (Hayward et al. 2011), as well as the (U-Th)/He ages presented herein. Even though many of the crustal blocks' boundaries coincide with major faults, this is not meant to imply that exhumation was along those specific faults, but perhaps along nearby faults. In many cases, the specific faults responsible for any tectonic exhumation cannot be identified because of the paucity of outcrops and lack of detailed studies on the faults in west-central Yukon: the spatial extent, fault type, timing of fault nucleation

and reactivation of many of these structures are still uncertain (e.g. Colpron et al. 2016; Ryan et al. 2014; Ryan, pers. comm., 2016). The published $^{40}Ar/^{39}Ar$ ages (Joyce et al. 2015; Knight et al. 2013) used to characterise the different crustal blocks do not include data from the Late Cretaceous Carmacks Group volcanic rocks that spans 70-55 Ma. These ages do not represent the timing of YTT exhumation, but instead provide a constraint on the timing of the Carmacks unconformity, placing the currently exposed portion of the YTT at the surface at this time. The $^{40}Ar/^{39}Ar$ ages from the Carmacks Group are younger than the $^{40}Ar/^{39}Ar$ (and occasionally the zircon (U-Th)/He ages) of the subjacent crystalline basement, which tentatively indicates that widespread Late Cretaceous volcanism did not reset the $^{40}Ar/^{39}Ar$ system in the surrounding rocks.

Five crustal blocks have been defined: two samples were used to characterize block 1, seven to eight samples for blocks 2, 3, and 4, and block 5 contains one sample. In the aforementioned section, diffusion and radiation damage annealing in zircon and apatite ages yields predictable trends in date-eU space. Since the effects of grain-specific parameters become greater with more residence time within the PRZ, date-eU correlations are related to the thermal history of the samples. In this section, (U-Th)/He ages with respect to eU for all samples within one group are described, and individual sample date-eU plots are reported in **Figures A1, A2** and **A3** in the Appendix.

2.4.2. Block 1

The Reid Lakes complex (block 1; **Figure 2.2**) is primarily composed of relatively undeformed and unmetamorphosed Devonian-Mississippian plutonic and volcanic rocks of the Simpson Range Suite and Finlayson assemblage (Colpron et al. 2015; Colpron and Ryan 2010; Ryan et al. 2010). Since it is relatively unmetamorphosed, the Reid Lakes complex is

unique within the YTT, and therefore it has a distinctive temperature-pressure history. This is evident with the 349-316 Ma $^{40}Ar/^{39}Ar$ cooling ages, which are much older than the $^{40}Ar/^{39}Ar$ cooling ages from the rest of the YTT (Knight et al. 2013). Average (U-Th)/He zircon ages from the plutonic samples in this area are 146-130 Ma (Knight et al. 2013). The Reid Lakes complex resides in the hanging wall of the Jurassic Willow Lake normal fault and the Cretaceous Stewart River normal fault, the latter fault in part responsible for the exhumation of metamorphic core complex of the Australia Mountain domain (block 5; Staples et al. 2016).

Only one sample, 08RAY002, is used for (U-Th)/He models (**Figure 2.3A**, **Table 2.1**). ^{4}He ages for both zircon and apatite remain concordant with increasing eU, spanning 141 and 102 Ma for zircon, and 51 and 46 Ma for apatite (**Tables 2.2, 2.3**). The eU values range from 151 to 323 ppm for zircon and 9 to 58 ppm for apatite. There is no trend between zircon ^{4}He ages and ESR, and a slightly negative trend between apatite ^{4}He and ESR, which ranges from 35 and 50 μm for zircon and 34 to 78 μm for apatite. This sample is an unfoliated granodiorite which is more representative of the Reid Lakes complex than sample 09RAYMC092. The latter is a quartz sandstone containing pre-Devonian zircon (Knight et al. 2013), and the zircon's pre-depositional history and relatively protracted cooling probably explains the large variance in ^{4}He ages (**Table 2.2**).

2.4.3. Block 2

Block 2 is in the hanging wall of the YRSZ, which defines the western limit of this crustal block. It is composed of the Simpson Range, Snowcap and Finlayson assemblages, similar to block 1, however block 2 underwent Permian high pressure and high temperature metamorphism, resulting in amphibolite facies metamorphism, in contrast with the relatively unmetamorphosed block 1 (Berman et al. 2007; Knight et al. 2013). Most $^{40}Ar/^{39}Ar$ data

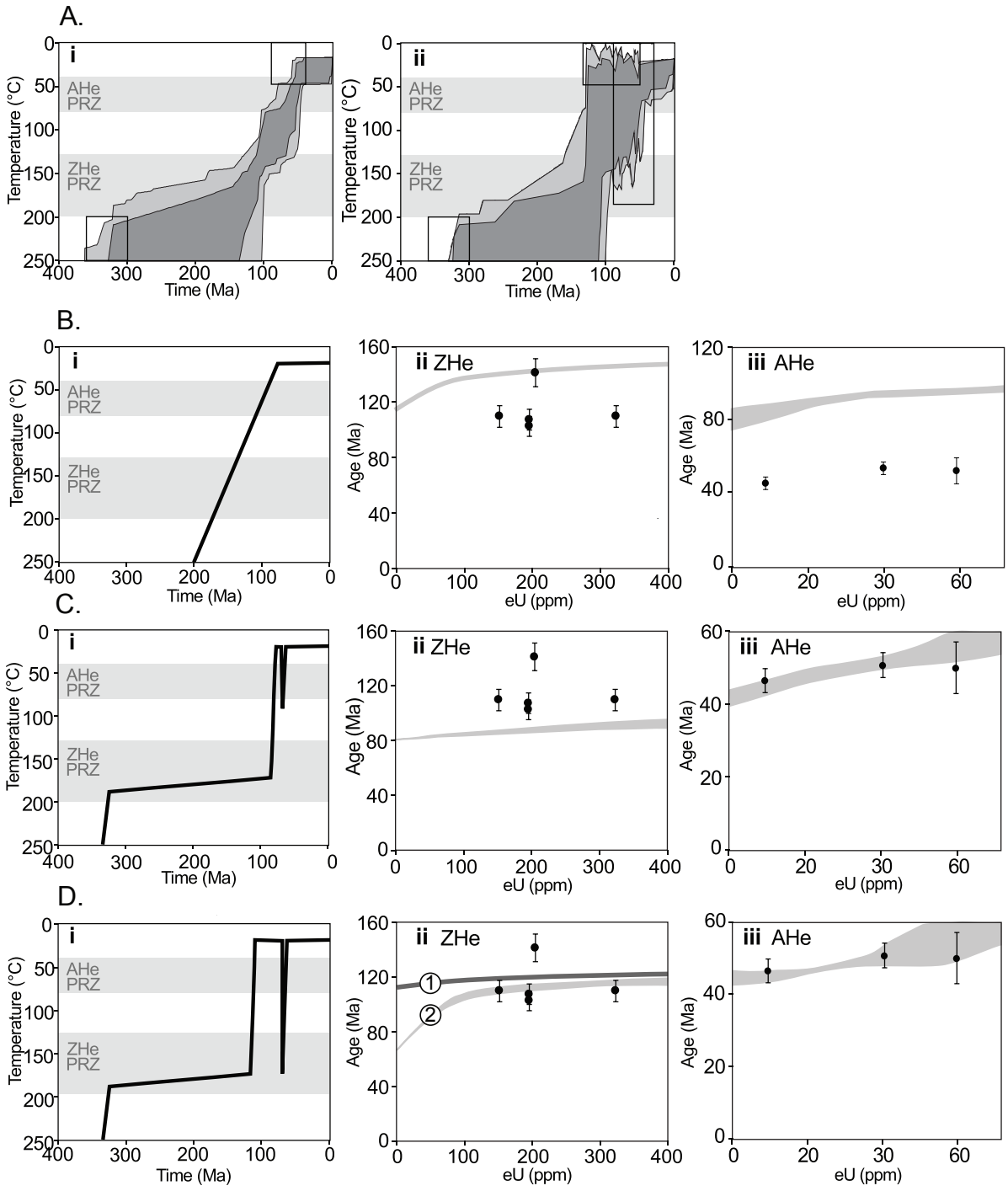

Figure 2.3. Numerical modeling results for crustal block 1 showing A) inverse models for sample 08RAY002; boxes represent the independent time-temperature constraints applied to the model and are listed in Table 2.4, without (Ai) and with (Aii) the 90-30 Ma constraint discussed in the text. The light grey polygons in A) envelops all time-temperature pathways of acceptable fit from the Monte Carlo inversion, and the dark grey polygon envelops the pathways of good fit (after 10,000 inversions). B-Di) Forward model paths; B-Dii, iii) Forward model results for path in (i) shown as age-eU envelopes (grey area) for a range of grain sizes and eU values, plotted against measured zircon (ZHe) and apatite (AHe) ages, respectively. Envelopes 1 and 2 in Dii are for the time-temperature path without and with a reheating event in the Late Cretaceous, respectively. In all age-eU graphs, ESR ranges from 35 to 50 μm for zircon, and 40 to 80 μm for apatite.

Table 2.4. Geologic constraints used in inverse modeling

Sample group	Age (Ma)	T range (°C)	Details	Reference
1	375-335	800-900	U-Pb crystallization	Knight et al. 2013; Colpron et al. 2015
	360-300	200-500	^{40}Ar-^{39}Ar; metamorphic cooling	Knight et al. 2013
	130-50	0-60	Unconformity with Carmacks group volcanic rocks	Ryan et al. 2003
	90-30	0-180	Reheating event	
2	365-345	800-900	U-Pb crystallization	
	260-240	500-650	HP metamorphism	Berman et al. 2007
	200-170	300-500	^{40}Ar-^{39}Ar; K/Ar; metamorphic cooling	Knight et al. 2013; Joyce et al. 2015
	120-90	0-60	Unconformity with Indian River formation	Lowey and Hills 1988
	95-55	0-200	* Reheating event	
3	270-240	800-900	U-Pb crystallization	
	195-155	200-500	^{40}Ar-^{39}Ar; metamorphic cooling	Joyce et al. 2015
	130-50	0-60	Unconformity with Carmacks group volcanic rocks	Ryan et al. 2003
	90-50	0-200	* Reheating event	
4	300-250	800-900	U-Pb crystallization	Wanless et al. 1978
	110-80	250-450	^{40}Ar-^{39}Ar; metamorphic cooling	Joyce 2002; Godwin 1975; Wanless et al. 1978; Johnston 1995
	100-60	0-100	Unconformity with Carmacks group volcanic rocks	Ryan et al. 2003
	75-0	0-200	* Reheating event	
5	375-350	800-900	U-Pb crystallization	Mortensen 1990
	155-110	600-700	HP metamorphism	Staples et al. 2013
	140-100	300-500	^{40}Ar-^{39}Ar; metamorphic cooling	Staples et al. 2014; Hunt & Roddick 1992
	120-90	0-60	* Unconformity with Indian River formation	Lowey & Hills, 1988
	90-30	0-200	* Reheating event	

* Additional constraints tested on the inverse models as described in section 2.5.

record midcrustal cooling ages of 205 to 165 Ma (Berman et al. 2007; Joyce et al. 2015; Knight et al. 2013). Data from the eastern and western areas of block 2 have different ^{4}He age-eU signatures, as described below.

In the western portion of block 2, zircon (U-Th)/He ages are 64 to 262 Ma, though most ages are between 135 to 179 Ma, with a generally positive correlation with eU (**Figure 2.4B**), between 195 and 845 ppm. The ESR values are from 40 to 79 μm, and 03RAY316 has values between 28 and 34 μm (**Table 2.2**). The apatite ages yield a dispersion from 32 to 282 Ma, an abnormally large range for apatite in this study. This may be due to ^{4}He implantation from neighboring grains, fluid inclusions, broken grains or a mineral zonation (Flowers et al. 2009; Ketcham 2012; Meesters and Dunai 2002; Murray et al. 2014; Spencer et al. 2004; Spiegel et al. 2009). For apatite data with relatively smaller errors (<15 m.y.), the ages span 32 to 126 Ma, with a slightly positive age-eU correlation (**Figure 2.4B**; **Table 2.3**). The eU values are 2 to 74 ppm and ESR values are from 23 to 54 μm (**Table 2.3**). The eastern samples in block 2 are characterized by zircon (U-Th)/He ages of 115 to 82 Ma and a positive age-eU correlation (**Figure 2.4B**) with values between 88 and 242 ppm, and ESR ranges from 61 to 84 μm (**Table 2.2**).

2.4.4. Block 3

Defined as a separate tectonometamorphic domain from block 2 and fundamental component of the YTT (Berman et al. 2007; Staples et al. 2016), block 3 is composed of Permian greenschist facies and amphibolite facies metamorphic rocks, mainly the Klondike Schist and the Snowcap assemblage intruded by the Sulphur Creek Suite. This block is structurally lower than blocks 1 and 2 (Ryan, pers. comm., 2016) and was subjected to Permian high pressure metamorphism, and subsequently retrogressed to greenschist facies in

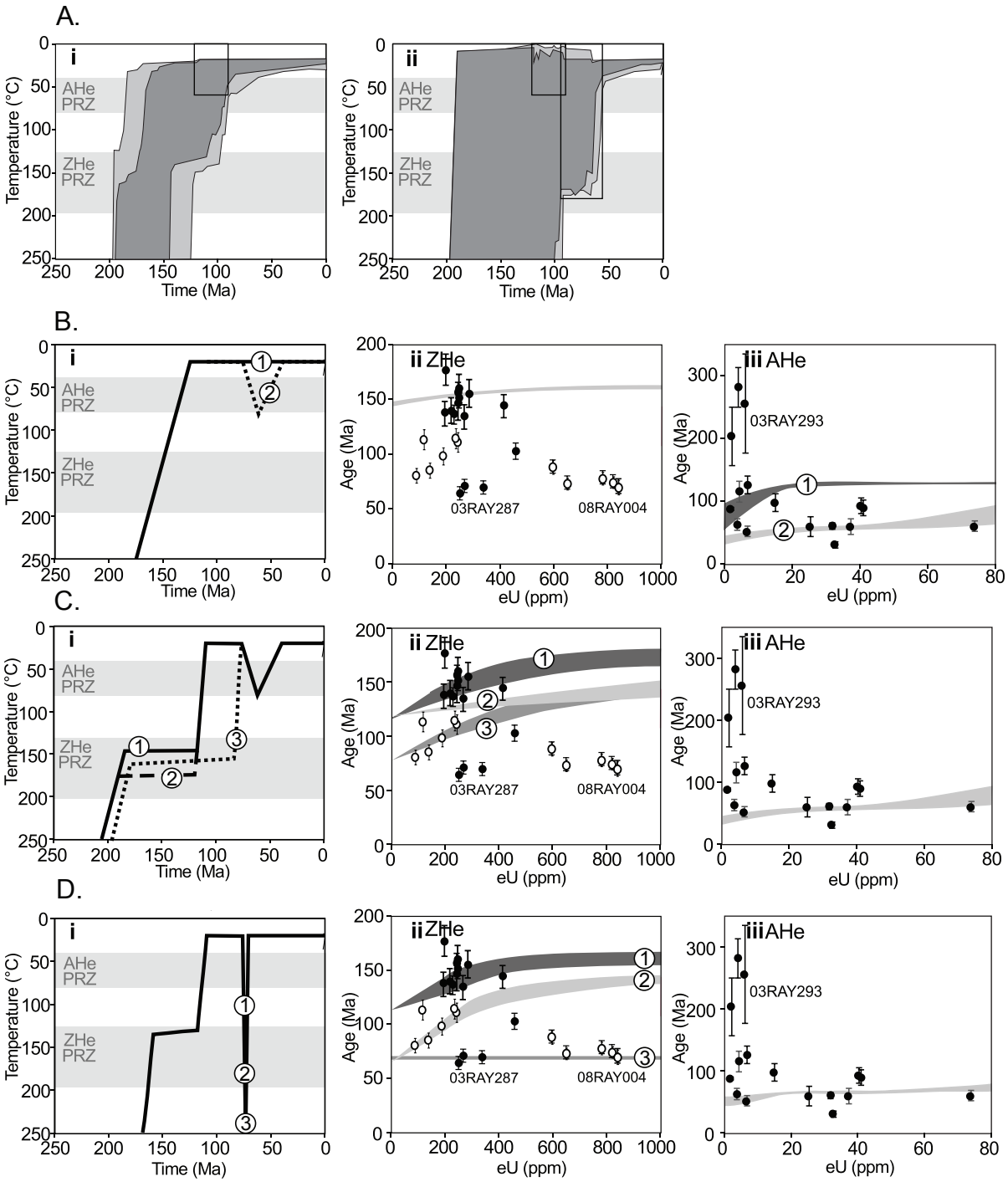

Figure 2.4. Numerical modeling results for crustal block 2 showing Ai,ii) inverse models for samples 03RAY293 and VN0102, respectively; boxes represent the independent time-temperature constraints applied to the model and are listed in Table 2.4, with and without the 95-55 Ma constraint, respectively. B-D) Forward models: samples that are outliers in age-eU space are identified on the graphs. White data points correspond to results from the eastern part of block 2 (see Figure 2.2). B) ESR ranges from 40 to 80 µm for ZHe, and 20 to 40 µm for AHe. C, D) the dark envelopes have an ESR range from 35 to 50 µm for ZHe, and 60 to 84 µm for the lighter ZHe envelopes (represents samples on the eastern side of block 2). ESR ranges from 20 to 40 µm for AHe. Paths 1-3 for each forward model is described in section 2.5. An envelope with no number means that any of the paths 1-3 give the same result. Dashed lines are used to differentiate between different paths. Formatting is as in Figure 2.3.

certain areas (Berman et al. 2007). Block 3 is bounded by major thrust faults including the YRSZ and Moose Creek fault, and the truncation of a high, positive magnetic anomaly (Hayward et al. 2011). Mineral $^{40}Ar/^{39}Ar$ data from Joyce et al. (2015) resolves mid-crustal cooling from 185 to 163 Ma.

Zircon (U-Th)/He ages are between 90 and 123 Ma, but relative to the samples in the eastern side of block 2, the positive correlation between age and eU is less remarkable (**Figure 2.5B**). The zircon cooling ages for sample 00VN002 are between 56 and 24 Ma. The eU values range from 0.04 to 1225 ppm, and ESR ranges from 29 to 101 μm (**Table 2.2**). Apatite (U-Th)/He ages are 68-125 Ma, apart from two grains with 511 Ma and 544 Ma dates. Apatite ages between 125 and 68 Ma increase with elevated eU, which varies from 1 to 32 ppm. ESR varies from 25 to 46 μm (**Table 2.3**).

2.4.5. Block 4

In block 4 are the Sulphur Creek Suite, Snowcap and Finlayson assemblages and Cretaceous to Paleogene magmatism, separated from block 2 by the low-angle YRSZ and Moose Creek Fault (**Figure 2.2**; Ryan et al. 2014). Block 2 south of the YRSZ is also a distinct magnetic domain (Hayward et al. 2011). The White River assemblage, is located southwest of block 4 in **Figure 2.2** and is structurally lower than the YTT (Ryan et al. 2014), therefore it is not included in the crustal block. Block 4 is characterized by late-Early to Late Cretaceous $^{40}Ar/^{39}Ar$ ages (Godwin 1975; Johnston 1995; Joyce 2002; Wanless et al. 1978).

The ^{4}He ages in this group lack a positive or negative trend with respect to eU (**Figure 2.6B**). Zircon data includes dates from 48 to 84 Ma, with corresponding eU between 49 to 1444 ppm. ESR varies between 30 and 108 μm (**Table 2.2**). Only one sample had apatite

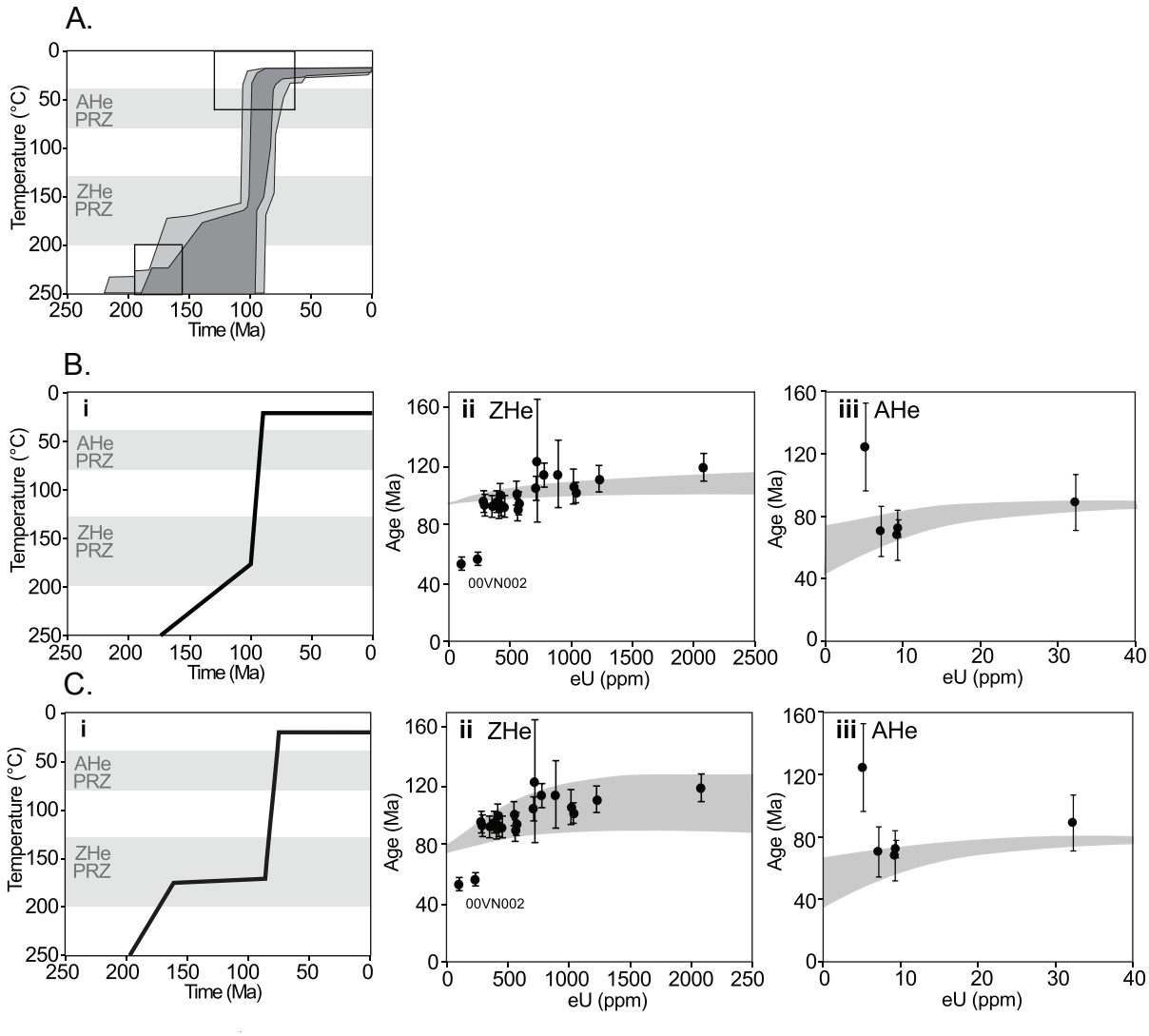

Figure 2.5. Numerical modeling results for crustal block 3 showing A) inverse model for sample 01RAY039; boxes represent the independent time-temperature constraints applied to the model and are listed in Table 2.4. B-C) Forward models: samples that are outliers in age-eU space are identified on the graphs. In all age-eU graphs, ESR ranges from 30 to 100 μm for ZHe, and 30 to 45 μm for AHe. Formatting is as in Figure 2.3.

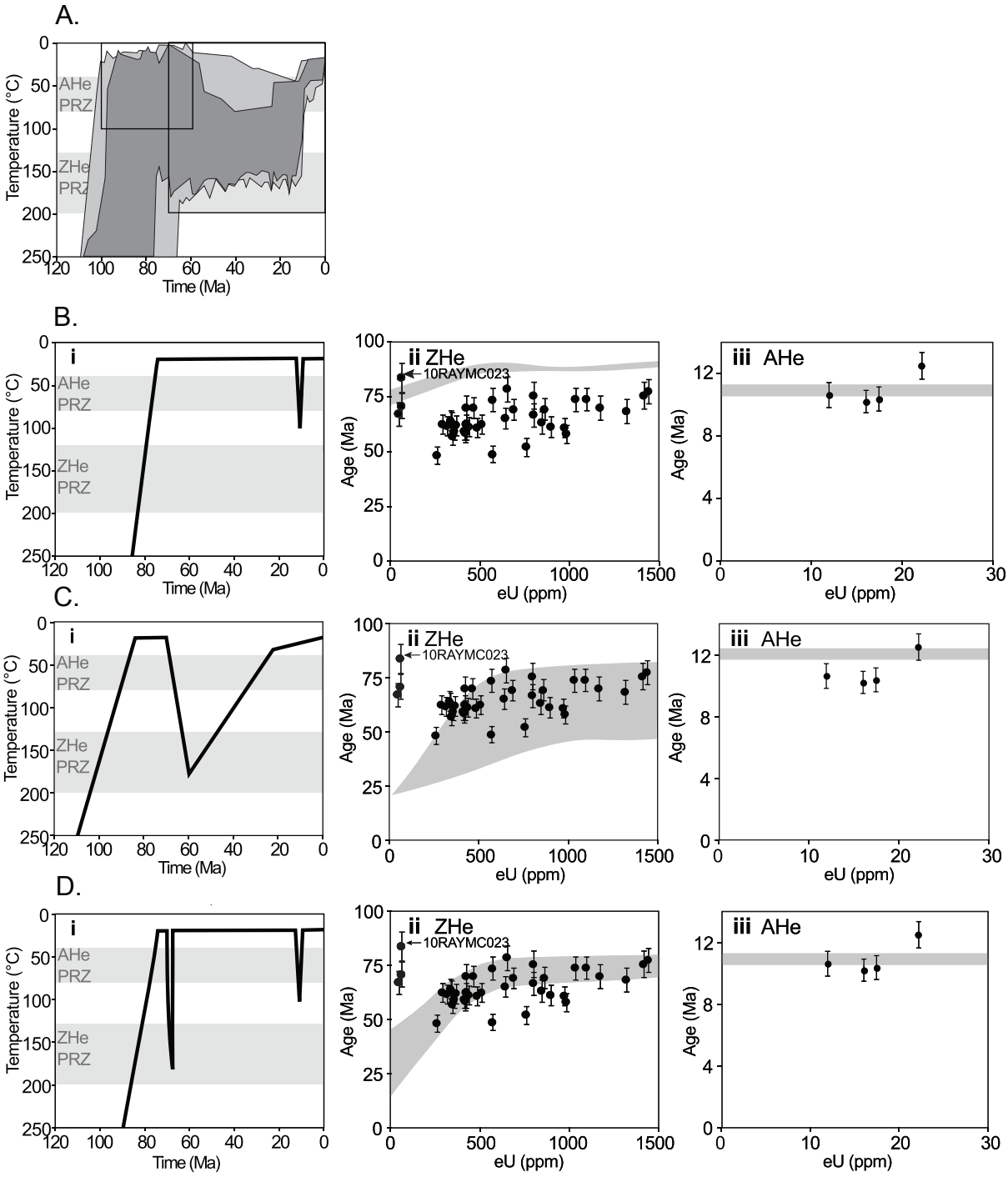

Figure 2.6. Numerical modeling results for crustal block 4 showing Ai) inverse model for sample 10RAYJR103; boxes represent the independent time-temperature constraints applied to the model and are listed in Table 2.4. B-D) Forward models: samples that are outliers in age-eU space are identified on the graphs. In all age-eU graphs, ESR ranges from 30 to 85 µm for ZHe, and 45 to 60 µm for AHe. Formatting is as in Figure 2.3.

(10RAYJR103), and yielded ages of 13 to 10 Ma. The eU values span 12 to 22 ppm, and ESR ranges from 48 and 58 μm (**Table 2.3**).

2.4.6. Block 5

Block 5 is the Australia Mountain domain, bounded by the Australia Creek and Stewart River faults, is composed of metamorphosed parautochthonous continental margin (Staples et al. 2013). This metamorphic core complex is thought to have exhumed from below the YTT in the late-Early Cretaceous (Staples et al. 2013, 2016). The block is characterized by a positive magnetic anomaly and relatively young $^{40}Ar/^{39}Ar$ ages, between 140 and 102 Ma (Staples et al. 2016).

The granodiorite sample from the block yields only three zircon grains and no apatite. Zircon (U-Th)/He ages range from 78 to 119 Ma, and eU values that vary from 261 to 760 ppm (**Figure 2.7B**). ESR values are from 63 to 74 μm (**Table 2.2**).

2.5. Numerical Modeling Results

The dispersion in zircon and apatite (U-Th)/He dates in this dataset can be used to resolve the low temperature history of the YTT. Although **Figures 2.3-2.7** only shows time-temperature paths below 250 °C, the numerical models in fact start at 900 °C (maximum crystallisation conditions for the granites) and include other independent geologic constraints at temperatures above 250 °C, such as $^{40}Ar/^{39}Ar$ ages (**Table 2.4**). Zircon (U-Th)/He ages cannot accurately resolve a time-temperature history above ~200 °C, thus it is important to include the timing of higher temperature events in the models as these will enable the models to explore a greater range of temperatures beyond those preserved in the (U-Th)/He dataset.

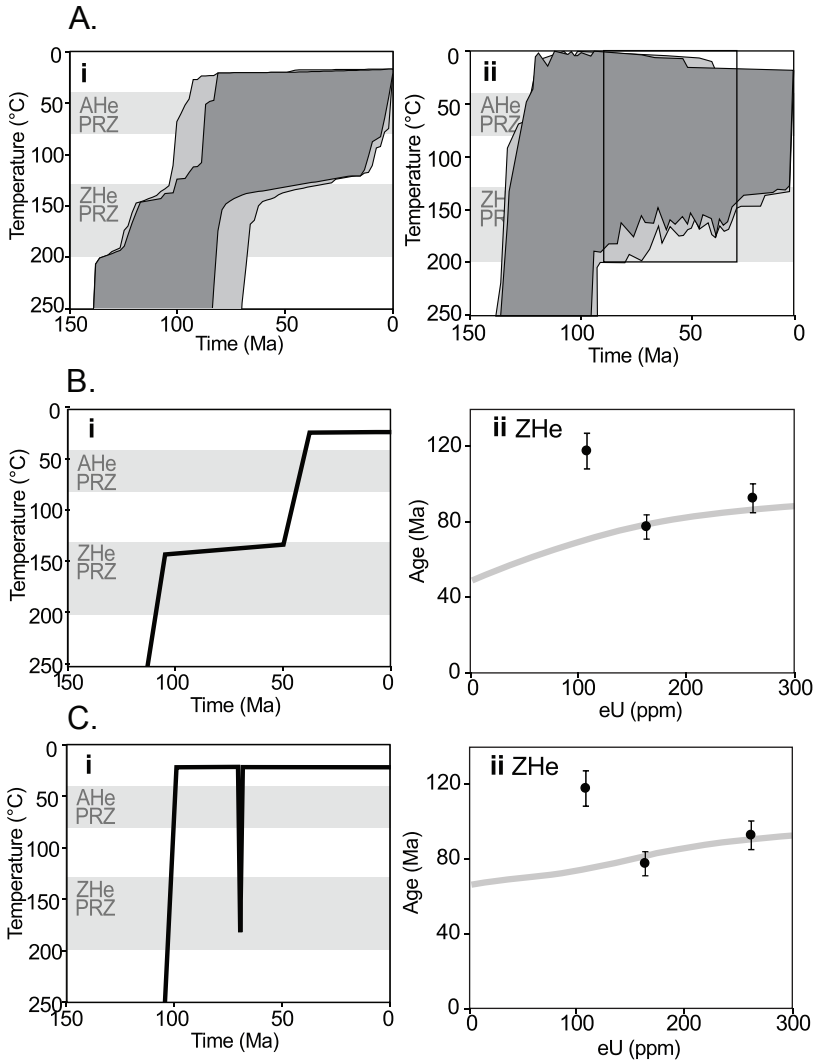

Figure 2.7. Numerical modeling results for crustal block 5 showing Ai,ii) inverse models for sample 03RAYP037; boxes represent the independent time-temperature constraints applied to the model and are listed in Table 2.4, without (Ai) and with the 90-30 Ma constraint (Aii). B-C) The ESR used for the forward models is 73 μm. Formatting is as in Figure 2.3.

From the forward and inverse models, the timing and rates of cooling and heating events are resolved from the analytical data, which are often directly linked to tectonic processes. In west-central Yukon, higher temperature thermochronology, geochronology and thermobarometry studies have resolved important Jurassic and Cretaceous tectonic events affecting the lower crust, and low-temperature thermochronology has the potential to reveal the consequences that these processes had on the upper crust (e.g. Berman et al. 2007; Hansen et al. 1991; Johnston et al. 1996; Knight et al. 2013; Staples et al. 2013, 2016). In addition to determining the timing of cooling and exhumation in this area, the forward models were also evaluated in the context of a previously recognised Cretaceous high flux magmatic event, and to what extent the (U-Th)/He system may have been partially reset by an elevated geothermal gradient in the upper crust due to the volcanism.

2.5.1. Block 1

Two inverse models for the same sample are shown in **Figure 2.3A**. The first model includes previously published geological constraints for these rock units as discussed in the previous sections. The second model has the same constraints, but with two added constraints which assess whether block 1 could be at surface temperatures before the deposition of the nearby late-Early Cretaceous Indian River Formation, and whether a heating event in the Late Cretaceous (90-30 Ma) related to Carmacks volcanism or Eocene displacement along the Tintina fault may have (partially) reset the samples (**Table 2.4**). The first inverse model is shown in **Figure 2.3Ai**, the paths with a "good fit" require the Reid Lakes complex to cool below 200 °C as early as the Pennsylvanian. At c. 130-100 Ma, inverse modeling shows an increase in cooling rate (~10 °C/km) until surface temperatures are reached post-50 Ma. There are no paths that reach surface temperatures before 70 Ma, the age of the unconformity with

the Carmacks Group volcanics. The second inverse model (**Figure 2.3Aii**) also has good and acceptable paths, meaning that there are possible thermal histories that include a reheating event during or after the Late Cretaceous. This model yields similar "good fit" time-temperature paths as in **Figure 2.3Ai** until c. 130 Ma. The cooling rate increases at this time, and some paths reach surface temperature conditions earlier, at c. 130 Ma, followed by a heating event between 90 and 30 Ma, at a maximum of ~150 °C. The timing of cooling to surface temperatures after the heating event is not resolved by the inverse model.

Multiple plausible forward model paths based on the inverse modeling results and their model age-eU results are shown in **Figures 2.3B-D**. The paths in the forward model reach surface temperatures before the Carmacks unconformity at c. 70 Ma. The first forward model exhibits a constant cooling rate of 1.8 °C/Ma through the zircon and apatite PRZ, where surface temperatures are reached by 75 Ma, and temperatures remain cooler than the apatite PRZ until the present day (**Figure 2.3B**). The resulting age-eU envelope for zircon is c. 30-40 m.y. older than most measured ages, and fits only one of five measured ages that is not in the 103-110 Ma range. This suggests that if the crustal block cools to surface temperatures before 70 Ma, but is not subsequently reheated, the apatite age-eU envelope for this model yields older ages than the measured Eocene ages. For the zircon forward model, the width of the age-eU envelope is <5 m.y., and <10 m.y. for the apatite model. The forward model path in **Figure 2.3C** spends 250 m.y. in the zircon PRZ and cools relatively rapidly (~16 °C/km) to surface temperatures between 85 and 75 Ma. This crustal block is required to be at surface temperatures before c. 70 Ma, however the apatite ages are between 51 and 47 Ma. Because of these young apatite ages, the inverse models and forward model B show that pre-Paleogene surface temperatures are not possible without a subsequent reheating event to reset the apatite

system. A reheating event at c. 70 Ma that cools to surface temperatures within 2 m.y. fits the apatite ages if the temperatures attained are higher than the apatite PRZ (**Figure 2.3C**). However, the age-eU envelope for the zircon models is between 81 and 95 Ma, younger than the measured grains that have Early Cretaceous ages (**Figure 2.3C**). An earlier exhumation is required to satisfy the zircon data: the forward model path in **Figure 2.3D** spends c. 200 m.y. in the zircon PRZ, then cools relatively rapidly (~16 °C/km) to surface temperatures between 118 and 110 Ma, prior to the deposition of the Indian River Formation. The predicted zircon ages are therefore older than the predicted zircon ages in **Figure 2.3C** (age-eU envelope 1), and only fit the measured zircon and apatite ages if there is a c. 70 Ma reheating event that reaches temperatures of 180 °C (age-eU envelope 2).

The inverse and forward models show that in order to accommodate the Carmacks volcanics unconformity, a reheating event is required after crustal block 1 reaches the surface because the apatite ages are post-Late Cretaceous. Also, forward models C and D illustrate that cooling from the zircon PRZ to surface temperatures must occur prior to 85 Ma to fit the measured zircon data.

2.5.2. Block 2

The samples in block 2 are part of a distinct tectonometamorphic domain (Staples et al. 2016), however differences in (U-Th)/He ages and age-eU trends between the zircon in the western and eastern parts of the block may be explained by slightly disparate cooling histories. Therefore, no single sample is representative of the entire crustal block. Two inverse models for block 2 were evaluated, where the first has only geological constraints based on previous studies, and the second has the same constraints, but with an additional one to assess the possibility of a Late Cretaceous heating event. Both inverse models were performed using

sample 03RAY293, however they both had similar results, therefore only the first inversion is shown in **Figure 2.4Ai**. Since the samples within this crustal block have very different apatite age-eU trends and no single sample can represent the age-eU distribution of the block (**Figures A1, A2, A3**), the second inversion was also performed on sample VN0102, which is shown in **Figure 2.4Aii**.

At temperatures below 250 °C, the first inverse model exhibits two phases of cooling: a) cooling to the zircon PRZ between c. 200 and 150 Ma, and b) cooling to surface temperatures between c. 175 and 90 Ma. This sample does not allow a post-70 Ma heating event (**Figure 2.4A**). The model paths allow, but do not require, slow cooling between the two phases. The second inverse model shows that cooling from temperatures in excess of 250 °C to surface temperatures can be between c. 200 and 90 Ma, followed by a reheating event to maximum temperatures above the apatite PRZ between 95 and 55 Ma (**Figure 2.4A**). Since this sample only has apatite grains, the model cannot resolve the maximum temperature of the heating event.

The first forward model shown (**Figure 2.4B**) is a time-temperature path located within the envelope of inverse model 1, and cools at a constant rate of 4.6 °C/km until the path reaches surface temperatures at 125 Ma (path 1). The model zircon age-eU envelope is relatively constant across the eU values, and only fits with a small subset of samples with older ages (**Figure 2.4B**). The model apatite age-eU envelope only satisfies certain samples that have eU <20 ppm, and reaches a plateau at c. 130 Ma at higher concentrations of eU (path 1). A Late Cretaceous reheating event to 80 °C was added to this model, and did not change the zircon model ages (path 2). The model apatite ages became more uniform, only increasing by c. 20 m.y. within the range of eU, and fit the samples that have Eocene ages (**Figure 2.4B**).

Figure 2.4C shows three viable time-temperature paths that reside in the zircon PRZ for 67-96 m.y. at different temperatures, each having a different age-eU envelope for the zircon data. There is a similar Late Cretaceous-Paleocene heating event as in **Figure 2.4B**, therefore the model apatite ages are the same as the previous model (the apatite system is fully reset), and the following observations are for the zircon model ages. The difference in temperature within the zircon PRZ has the effect of widening the age-eU envelope (**Figure 2.4C**): within each path, the samples on the west side of the crustal block (black symbols in figure) are best represented by a time-temperature history when the rocks stay in the zircon PRZ for 67 m.y., then relatively quickly reach surface temperatures by 118 Ma (path 1). The same path was evaluated, only the rocks reside at a higher temperature within the PRZ (path 2); the resulting age-eU envelope has a lower slope and smaller width. The samples on the east side of the crustal block (white symbols in figure) are best represented by the age-eU envelope from a forward model path that spends c. 100 m.y. within the zircon PRZ at a higher temperature, followed by an increase in cooling rates until surface temperatures are attained, between 85 and 75 Ma (path 3; **Figure 2.4C**). The age-eU envelope for paths 1 and 3 have a similar slope, despite the difference in temperature during residence within the PRZ, illustrating that a protracted cooling history within the PRZ offsets the effect of higher temperatures on the age-eU trend by increasing the slope.

Figure 2.4D has a single forward model path, except for a c. 70 Ma reheating event that reaches different temperatures of 100 °C (path/envelope 1 in the figure), 190 °C (path/envelope 2 in the figure), and a temperature higher than the zircon PRZ (path/envelope 3 in the figure). This path cools rapidly to the upper crust by 110 Ma, prior to the deposition of the Indian River Formation that is exposed on the western portion of the crustal block

(**Figures 2.2, 2.4D**). The zircon age-eU envelope fits the pre-late Early Cretaceous measured ages from the western side of the crustal block when the reheating event reaches 100 °C (age-eU envelope 1), and fits the late-Early to Late Cretaceous measured ages from the eastern part of the crustal block (younger ages) when it reaches 190 °C (age-eU envelope 2). Samples 03RAY287 and 08RAY004 are spurious and only a complete resetting of the zircon (U-Th)/He system at c. 70 Ma can produce an age-eU envelope that agrees with these samples (age-eU envelope 3).

The inverse and forward models illustrate that there is no single time-temperature path that represents the data from the entire crustal block. However, block 2 can be divided into western and eastern sections, and according to forward modeling these areas may have the same low temperature history until they reach surface temperatures for the first time.

2.5.3. Block 3

One inverse model is shown for block 3 (**Figure 2.5A**). As with the other crustal blocks, a second inverse model was performed with an additional thermal constraint from 0 to 200 °C, between 90 and 50 Ma. Since the second inverse model was unsuccessful at resolving a thermal event within the additional constraint, only resulting in five "good fit" paths out of 10,000, and has similar path envelopes to the first model, only the first inverse model is shown. The inverse model illustrates that block 3 cooled to upper crustal temperatures in the Triassic or Jurassic, then cooled at a moderate rate until the late-Early to Late Cretaceous when it rapidly reached surface conditions.

Two plausible forward models are shown (**Figure 2.5B, C**). The forward model path in **Figure 2.5B** cools relatively rapidly through the zircon PRZ, within 25 m.y. starting at c. 125

Ma. Surface temperatures are reached by 90 Ma, resulting in age-eU envelopes that encompass most of the measured zircon and apatite ages. In **Figure 2.5C**, the forward model path reaches 175 °C in the zircon PRZ by 160 Ma, and stays within the PRZ for 75 m.y. The cooling rate increases at 85 Ma, and the path reaches surface temperatures by 75 Ma. The age-eU trend for zircon from this model is similar, only wider than the envelope from **Figure 2.5B** because of the protracted time within the zircon PRZ, thus better accounts for the spread in measured zircon ages. The increase in time spent in the zircon PRZ also requires cooling to surface temperatures at a later time than 90 Ma to fit the measured zircon and apatite ages (**Figure 2.5C**).

The forward models illustrate that cooling to the zircon PRZ can vary between the Middle Jurassic to Early Cretaceous while still fitting the data, depending on the cooling rate through the PRZ, and the time that the path cools through the upper bound of the zircon PRZ. The second forward model better represents the dispersion in zircon ages with the wider zircon age-eU envelope (**Figure 2.5B, C**), and the Jurassic thermal histories between blocks 2 and block 3 are similar, simplifying the exhumation model.

2.5.4. Block 4

For block 4, the time-temperature constraints used in inverse modeling are in **Table 2.4**. The inverse models do not yield "good" or "acceptable fit" time-temperature paths without an additional constraint between 75 and 0 Ma, and 0 and 200 °C, therefore the inverse model with the added constraint is the only one shown in **Figure 2.6A**. The inverse model shows that block 4 cooled to 20 °C in the late-Early to Late Cretaceous with a maximum amount of time within the zircon PRZ of 20 m.y. The apatite ages are younger than the constraint for the Carmacks unconformity (**Tables 2.2-2.4**), therefore in order to conform to the unconformity,

the inverse model requires a reheating event between 75 and 0 Ma up to ~180 °C to reset the apatite ages. This is also illustrated by the forward model **Figure 2.6B** where rapid cooling from 250 °C to surface temperatures between 85 and 75 Ma without reheating results in model zircon ages that are older than the measured ages. Since the forward models from the previous crustal blocks show that apatite ages that are younger than the time constraint for surface temperatures requires resetting after cooling to surface temperatures, a 2 m.y. Miocene reheating event to 100 °C was added to the model, however there is not yet any independent geological data to support this. The forward model in **Figure 2.6C** has a reheating event after the Carmacks unconformity that is c. 50 m.y. and reaches temperatures of 180 °C, and yields age-eU curves that represents the dispersion in zircon ages, and an apatite age-eU envelope that is 1-2 m.y. older than three out of four of the measured grains. The forward model in **Figure 2.6D** shows that partially resetting the zircon samples to 170 °C at c. 70 Ma and cooling to surface temperatures within a few million years yields an age-eU envelope that encompasses most of the measured zircon ages, and a similar reheating at c. 10 Ma to 100 °C resets the apatite (U-Th)/He system to Miocene ages.

The inverse and forward models for block 4 show that at least one reheating event is required after surface temperatures are attained for the first time (post 75 Ma) a maximum temperature of 180 °C, resetting the apatite ages.

2.5.5. Block 5

Inverse models for block 5 are limited by the lack of apatite data and other low temperature geologic constraints, leaving many possibilities for the low-temperature history of the Australia Mountain domain (**Table 2.4**). The first inverse model shown in **Figure 2.7A** is based on previously published geologic constraints that are >250 °C, therefore are not

within the time-temperature space of the figure. The first inverse model indicates that block 5 cooled to the zircon PRZ by the Early Cretaceous, but does not resolve the thermal history below this PRZ from the lack of independent temperature constraints and apatite dates (**Figure 2.7A**). The second inverse model has additional constraints which test the possibility of reaching surface temperatures before or during the deposition of the Indian River Formation, and the possibility of a reheating event during the Late Cretaceous-Paleocene (**Figure 2.7A**). The "good fit" paths from this model reaches maximum temperatures of ~190 °C within the constraint that tests for reheating.

Two forward models that yield age-eU envelopes that satisfy the measured zircon ages are shown in **Figures 2.7B** and **2.7C**. In **Figure 2.7B**, the forward model path reaches 150 °C by 105 Ma, followed by slow (<1 °C/km) cooling within the zircon PRZ until it reaches 130 °C at 50 Ma. Cooling rates then increase to ~9 °C/km until surface temperatures are attained. The age-eU curve is representative of two out of three measured zircon ages. The forward modeling path in **Figure 2.7C** illustrates relatively rapid cooling (~46 °C/km) to surface temperatures during the deposition of the 112-100 Ma Indian River Formation, to assess the interpretation that the material eroded from block 5 was deposited as the Indian River Formation (**Figure 2.2**; Colpron et al. 2016; Lowey and Hills 1988; Staples et al. 2016). This path results in a similar age-eU envelope as the forward model in **Figure 2.7B** if there is a reheating event to 180 °C, fitting the same two out of three measured zircon ages (**Figure 2.7C**).

2.6. Discussion

2.6.1. Exhumation of the Yukon Tanana Terrane, west-central Yukon

In order to interpret the data in a tectonic context, the preferred model(s) for the low temperature history of the YTT must be evaluated. When multiple time-temperature histories fit the (U-Th)/He data and independent field and geochronology data, the simplest model is chosen. In general, the age-eU trends do not exhibit noticeable positive to negative roll-over points, which suggests that the samples had a relatively short low-temperature cooling history supported by the numerical models that illustrate that the crustal blocks spent <250 m.y. in the zircon PRZ.

Pre-Cretaceous exhumation history

As illustrated in the previous section, numerical models suggest a low-temperature cooling history as early as the Carboniferous for some samples. Forward models show that the Reid Lakes complex (block 1) cooled to upper crustal temperatures before the Triassic (**Figure 2.3**), whereas blocks 2, 3, and 4 only cooled to the zircon PRZ between the Early Jurassic and Early Cretaceous (**Figures 2.4-2.6**). The cooling of block 1 earlier than the rest of the YTT corroborates previously published observations that block 1 occupied shallower crustal levels and was not deformed and metamorphosed at high pressure (9 kbar) conditions, unlike the rest of the YTT at ca. 260 Ma (Berman et al. 2007; Dusel-Bacon et al. 2002). Moreover, the timing of exhumation of block 2 from beneath block 1 along the WLF was interpreted to have started in the Early Jurassic, based on c. 190 Ma $^{40}Ar/^{39}Ar$ ages near the WLF that contrast with the Carboniferous ages recorded in the rest of the block (Knight et al. 2013).

Blocks 3 and 4 are structurally lower than blocks 1 and 2. They are interpreted to be from the same structural panel and possess generally similar rock assemblages (except for sample 11RAYAZ148 in block 4; Ryan et al. 2014). However, blocks 3 and 4 have very different (U-Th)/He ages and age-eU trends, indicating that the two crustal blocks have had dissimilar low-temperature histories. Plausible low-temperature thermochronology models place block 3 in the upper crust by the Middle Jurassic. $^{40}Ar/^{39}Ar$ and (U-Th)/He ages from block 4 are late-Early to Late Cretaceous, and the (U-Th)/He ages do not show steep positive or negative age-eU trends, suggestive of rapid cooling through the PRZ. Since they are from the same structural panel with no major faults separating the two blocks, it is likely that block 4 had a similar temperature history as block 3 until the Cretaceous, and that the $^{40}Ar/^{39}Ar$ and (U-Th)/He ages in block 4 were reset in the late-Early to Late Cretaceous by a heating event (**Figures 2.5, 2.6**). Moreover, in block 4, the Whitehorse plutonic suite including the Dawson Range Batholith was emplaced under mid- to shallow crustal conditions within this structural panel in the late-Early Cretaceous (Johnston et al. 1995; 1999), thus this block was in fact at shallow crustal temperatures (i.e. near the zircon PRZ) at this time, similar to block 3.

Previous studies report that YTT rocks were metamorphosed under amphibolite conditions during the Early Jurassic, and started to exhume to shallower depths in the Early to Middle Jurassic, cooling through $^{40}Ar/^{39}Ar$ closure temperatures between 205 and 163 Ma (Berman et al. 2007; Dusel-Bacon et al. 2002; Joyce et al. 2015). This exhumation event has been associated with the obduction of the YTT and other outboard terranes onto North American continental margin, which brought the obducted material to shallow crustal levels (Berman et al. 2007; Colpron et al. 2005; Dusel-Bacon et al. 2002; Hansen et al. 1991; Johnston et al. 1996; Knight et al. 2013; Staples et al. 2016). In the preferred low-temperature

forward models for blocks 2, 3 and 4, these blocks reach the zircon PRZ at c. 160 Ma (**Figures 2.4-2.6**). This simple model was chosen for Jurassic cooling since there is no requirement for crustal blocks 2, 3, and 4 to cool to upper crustal temperatures at different times based on the low-temperature thermochronology results, previously published field and structural observations (Joyce et al. 2015; Knight et al. 2013; Parsons, pers. comm., 2018; Ryan et al. 2014). Differential cooling to the zircon PRZ could be related to variable erosion rates within the study area or tectonic exhumation of one of the crustal blocks via low-angle normal faulting that accommodated a large amount of displacement in the Jurassic, similar to the exhumation of block 2 along the WLF. Block 2 is juxtaposed against the structurally lower blocks 3 and 4 at the YRSZ in the southwest of the study area. WNW-WSE brittle thrusting has been recorded on the YRSZ, displacing block 2 relative to blocks 3 and 4 at temperatures <450 °C sometime after 176 Ma (Parsons, pers. comm., 2018), however, the ESE-dip of the fault plane is shallow, therefore the WNW-ESE thrusting did not result in significant vertical offset in block 2 relative to blocks 3 and 4. The structurally lower level is thought to be exposed southwest of block 2 not only because of the YRSZ, but because of an interpreted regional-scale synform that formed during widespread NE-SW contraction prior to 176 Ma, bringing the structurally lower panel to the same crustal level as the structurally higher panel in some areas (Parsons, pers. comm., 2018; Ryan, pers. comm., 2016). The YRSZ had previously juxtaposed block 2 over blocks 3 and 4, either in an extensional environment in the Permian to Middle Triassic, or a compressional environment in the latest Triassic to Early Jurassic (Parsons, pers. comm., 2018). The folding event happened before the YTT reached the zircon PRZ since, at 176 Ma, the YTT in west-central Yukon was still cooling through $^{40}Ar/^{39}Ar$ closure temperatures (Joyce et al. 2015). Therefore, it is simplest to assume that

cooling rates at the upper bound of the zircon PRZ were uniform across the synform, and the samples from blocks 2, 3 and 4 reached the zircon PRZ at the same time.

Based on the interpretations from higher temperature studies that characterize the Jurassic as a time of crustal thickening due to the obduction of the YTT onto ancestral North America (Berman et al. 2007; Dusel-Bacon et al. 1995, 2006; Hansen et al. 1991; Johnston et al. 1996; Knight et al. 2013), the cooling of crustal blocks 2, 3 and 4 to upper crustal temperatures in the Middle Jurassic as resolved through our numerical models may be due to increased erosion rates as a result of thickening and uplift of the YTT. However, the forward models for blocks 2-4 show that the time at which these blocks reached the zircon PRZ can vary between the Early Jurassic (c. 200 Ma) to Early Cretaceous, and still satisfy the measured zircon and apatite data, moreover, the Jurassic cooling rates that are accepted by the models vary by multiple orders of magnitude (**Figures 2.3-2.6**). With such a wide range of possible cooling times and rates, the (U-Th)/He system is not able to resolve exhumation mechanisms in the shallow crust during the Jurassic and Earliest Cretaceous. Forward modeling has shown that the model age-eU results are much more sensitive to the thermal history from the late-Early Cretaceous to the present day.

Early Cretaceous exhumation of blocks 1, 2 and 5

The preferred thermal history during the Cretaceous involves the relatively rapid cooling of the structurally higher blocks 1 and 2 to the surface between 118 and 110 Ma. Block 2 must be exposed at the surface and at sea-level by the Early Cretaceous because of the unconformity with the Indian River Formation, which was deposited in the Albian in what is interpreted to be a marine environment (Lowey and Hills 1988; Mortensen and Dusel-Bacon 2014). Since the Indian River Formation is exposed in such a small area of block 2, the low-temperature

models cannot resolve if the entire extent of block 2 on **Figure 2.2** was at the surface by 110 Ma, however this is the simplest model. Numerical modeling indicates that the data on the eastern part of block 2 may have cooled to surface temperatures later than the western part in the Late Cretaceous, and to accommodate the age-eU relationship, this model requires the eastern and western parts of block 2 to be at different temperatures prior to the increases in cooling rate in the Cretaceous (**Figure 2.4**). If the western part of block 2 exhumed earlier than the eastern part, this either requires different erosion rates between the western and eastern parts of block 2 during the Cretaceous, or tectonic exhumation through a combination of thrust-driven uplift and erosion, or exhumation through normal faulting. There are no independent constraints on erosion rates between the eastern and western parts and currently there are no mapped faults that separate block 2 into eastern and western parts that may explain a differential cooling history within the block. Therefore the simpler solution of the entire crustal block exhuming at the same time is preferred. Perhaps the NE-SW trending Stewart River fault, that cuts across the northern part of block 2, is more significant than previously suggested and defines a separation of block 2 into western and eastern parts, however this is equivocal given the sparse thermochronology samples in the eastern part of block 2.

Block 1 may also exhume to the surface later than 110 Ma, however the simpler model of block 1 exhuming at the same time as block 2 is preferred. A differential exhumation between blocks 1 and 2 is unlikely because this would imply that block 1 would exhume along its bounding low-angle faults (Stewart River and Willow Lake faults). These faults are not optimal for exhumation of block 1 from temperatures of ~170 °C to surface temperatures, because thrusting on low-angle faults is unlikely to create enough vertical offset to

significantly increase erosion. There are no other known faults nearby that may accommodate enough displacement to exhume block 1 separately.

According to our preferred model, block 5, the metamorphic core complex that formed beneath the YTT, exhumed to surface temperatures in the late-Early Cretaceous (**Figure 2.7**) after cooling through $^{40}Ar/^{39}Ar$ closure temperatures in the Early Cretaceous (Hunt and Roddick, 1992; Staples et al. 2014). Even though the numerical models allow exhumation to surface temperatures in the Eocene, late-Early Cretaceous exhumation is the preferred model, since the YTT surrounding it has been tectonically quiescent since the Late Cretaceous (Gordey and Ryan 2005; Ryan et al. 2003, 2010, 2017; Staples et al. 2016), and it supports the interpretation that the 112-100 Ma Indian River Formation in block 2 is a syn-extensional detachment basin to the Australia Creek fault (Staples et al. 2016). Also, there are no known post-Late Cretaceous sedimentary units that can be associated with the exhumation of block 5 in the Eocene (Colpron et al. 2016). The late-Early Cretaceous exhumation of block 5 supports the model for late-Early Cretaceous exhumation of block 1; when block 5 exhumes, block 1 is required to have exhumed prior to this, since the final exhumation of block 5 was along the Stewart River fault, the SE-dipping normal fault that bounds block 1 to the northwest (**Figure 2.2**). The Stewart River fault cross cuts the Australia Creek fault, therefore exhumation along the Stewart River fault post-dated the exhumation of block 5 along the Australia Creek fault (**Figure 2.2;** Staples et al. 2016).

Blocks 3 and 4 did not exhume to the surface by 110 Ma, such as blocks 1 and 2, since blocks 3 and 4 were at greater depths at this time, constrained by the 105-100 Ma Dawson Range batholith that intruded the structural panel of blocks 3 and 4 at mid- to shallow crustal levels (Johnston, 1999). Intrusion of the batholith likely reset the $^{40}Ar/^{39}Ar$ ages to c. 105-90

Ma (Godwin 1975; Johnston 1995; Joyce 2002; Wanless et al. 1978) and zircon (U-Th)/He ages to c. 80-60 Ma in block 4 (**Table 2.2**). Thus, an exhumation mechanism is required to cool blocks 1, 2 and 5 in the late-Early Cretaceous without exhuming blocks 3 and 4.

The rate of cooling alone cannot be used to distinguish between the exhumation processes in the Early Cretaceous, however in certain cases it can narrow the possibilities. Knowledge of the exhumation of shallow crustal material is imprecise because, in part, of a lack of information on paleogeothermal gradients and exact cooling rates, since the cooling rates in certain cases in the forward models may change by an order of magnitude without altering the overall model's results. In the Cretaceous for example, the models cannot distinguish between cooling rates on the order of 10 °C/Ma or 100 °C/Ma. In **Figures 2.3-2.7**, the increase in Cretaceous cooling rates are 10-15 °C/Ma. Since paleogeothermal gradients are also unknown, so are the depths from which the crustal blocks exhume. Block 2 is modeled to have a pre-exhumation temperature between 140 and 135 °C, meaning there was ~3.4 km of material removed from the YTT above block 2 between 118 and 110 Ma, assuming the geothermal gradient in the upper crust is similar to the modern-day estimates of ~40 °C/km (see Chapter 3; Hyndman et al. 2005). Moreover, the high modern-day geothermal gradient likely developed as a response to lithospheric thinning, which usually involves widespread rapid cooling and exhumation (e.g. Bao et al. 2014; Currie et al. 2008; Currie and Hyndman 2006; Morales and Tommasi 2011; Ueda et al. 2012). However, there is no indication in the low-temperature thermochronology data that this would have happened before the Early Cretaceous cooling event. If the very slow cooling (<1 °C/Ma) between the Jurassic and Cretaceous rapid cooling events is due to slow or no erosion, a geothermal gradient might be as low as ~10 °C/km, since a lack of erosion is often associated with low geothermal gradients

(Stüwe 2007). This would mean that ~14 km of material must have been removed from block 2 in the Cretaceous – an unrealistic amount. On a greater scale, since the northern Canadian Cordillera was still an active orogen between the Jurassic and Cretaceous cooling events, the geothermal gradient may have been higher.

The equivocal exhumation rates hinder a detailed analysis of the exhumation history and shallow crustal processes of the YTT, however geological constraints and numerical modeling results do require there to be a hiatus of c. 30 m.y. between the exhumation of blocks 1, 2 and 5, and blocks 3 and 4. Climate-driven erosion is often invoked as an efficient exhumation process (e.g. Clift et al. 2008; Reiners and Brandon 2006; Thiede et al. 2004; Willett 1999), however this does not explain the differential exhumation that is apparently present across west-central Yukon. The difference in thermal histories between block 2 and blocks 3 and 4 is also not explained by the burial of block 2 by the Indian River Formation, which is interpreted to have filled numerous small, shallow basins, since the rocks have not been deformed or undergone metamorphism (Ryan and Gordey 2004). A tectonically-driven exhumation may cause a differential exhumation if there are major faults separating block 2 from blocks 3 and 4, supported by the sample groups occupying distinct areas in age-eU space (**Figures 2.3-2.7**). Low-angle normal faults may exhume footwall rocks very rapidly (e.g. Ring et al. 1999), however there is no known low-angle normal fault that could have exhumed blocks 1, 2 and 5 in the Cretaceous (Colpron et al. 2016). The preferred forward model paths suggest cooling from upper crustal conditions to surface temperatures between 118 and 110 Ma, which does not require extremely rapid exhumation. The crustal-scale YRSZ is a major fault separating block 2 from blocks 3 and 4, which has been reactivated multiple times, including under brittle conditions (Parsons, pers. comm., 2018). Since block 2 is on the

hanging wall of the fault, thrusting along this fault leading to uplift and erosion would need to be invoked to explain the increase in cooling rates. Reactivation of the fault due to NE-SW contraction in the late-Early Cretaceous could have resulted in southwestward thrusting along the YRSZ and uplift of block 2, which is consistent with late Cretaceous amphibolite facies metamorphism and a suggested crustal thickening episode in the YTT and Kluane schist south of the study area in southwestern Yukon (Israel et al. 2011; Mezger et al. 2001; Vice 2017). Erosion contemporaneous or subsequent to the thrusting of blocks 1 and 2 can explain the increase in cooling rates, and can explain the preferred thermal model where blocks 1, 2 and 5 exhume at the same time in the late-Early Cretaceous (**Figure 2.8A**). Even though the late-Early Cretaceous is associated with northwestward displacement of the YTT (Gabrielse et al. 2006; Pavlis et al. 1993; Staples et al. 2016), northwestward thrusting along the YRSZ is not as likely to have resulted in uplift since the plunge of the synform (to the southeast) is shallow (Parsons, pers. comm., 2018).

Late Cretaceous exhumation of blocks 3 and 4

There must also be a mechanism for the Late Cretaceous exhumation of blocks 3 and 4 after the emplacement of the 105-100 Ma Dawson Range Batholith. The preferred forward models have increasing cooling rates at 85 Ma, until surface temperatures are reached at 75 Ma. If a geothermal gradient of 25 °C/km is used, ~7 km of material had to be removed to exhume blocks 3 and 4 within 10 m.y., or ~4 km of material if a geothermal gradient of 40 °C/km is used. Numerous faults are located near or at the boundary separating block 2 from blocks 3 and 4, including the YRSZ and the Big Creek fault (**Figure 2.2**; Colpron et al. 2016), and the delayed exhumation compared to block 2 suggest a tectonic exhumation process. The lack of published data on fault kinematics leaves many possibilities for the exhumation

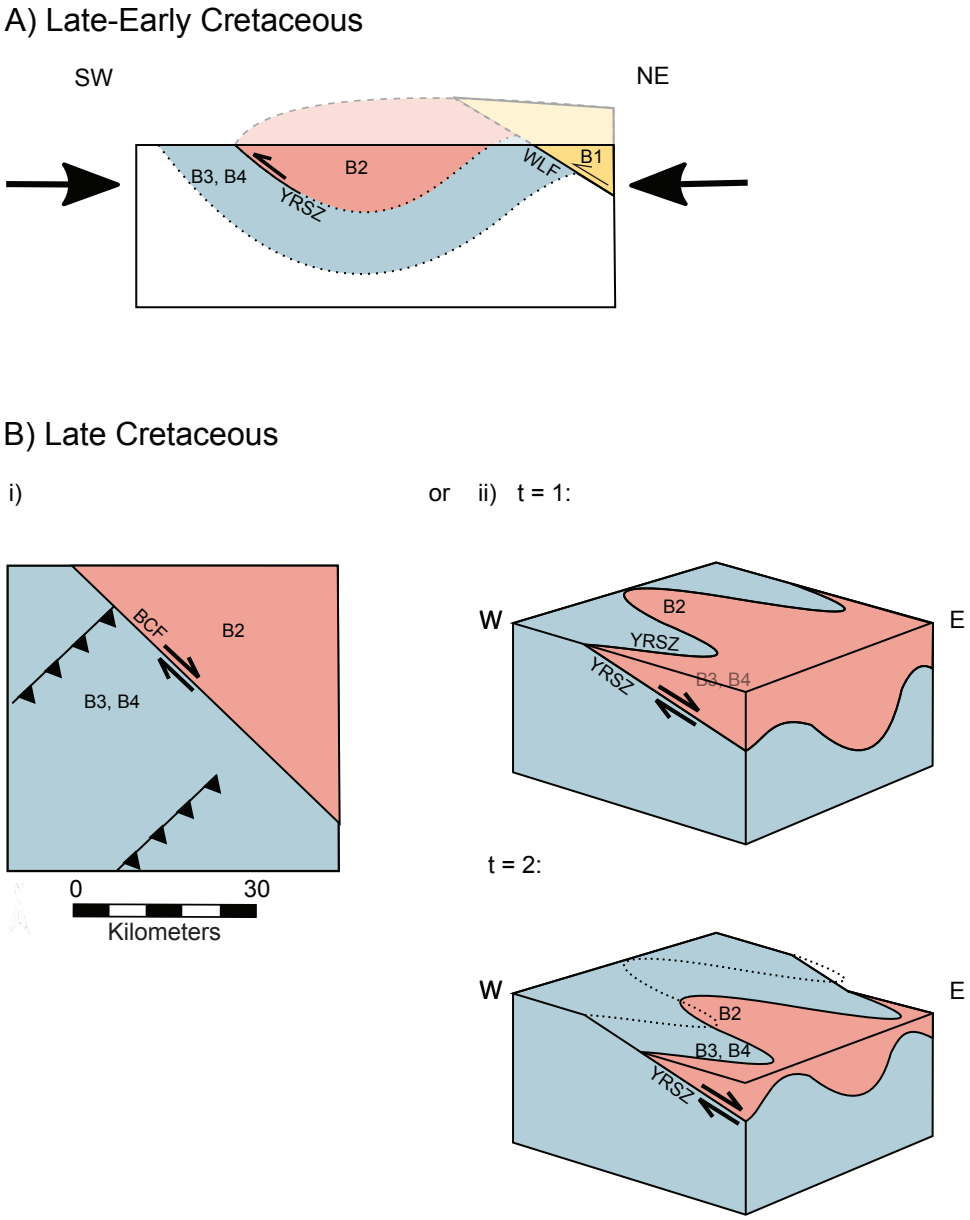

Figure 2.8. A) Schematic cross-section showing the late-Early Cretaceous orogen-normal compression resulting in thrusting along the YRSZ and WLF, which led to uplift and increased erosion rates of blocks 1 and 2. The dotted line shows the inferred YRSZ synform (Ryan pers. comm. 2016). Bi) Schematic map showing a possible exhumation mechanism for the Late Cretaceous deformation of blocks 3 and 4, as proposed NE-SW-trending thrust faults accommodate shortening parallel to the BCF causing uplift and erosion in blocks 3 and 4. Bii) Schematic block diagram showing an alternate deformation mechanism for the Late Cretaceous exhumation of blocks 3 and 4 as NW-SE extensional exhumation is along the YRSZ. Dotted line in t = 2 corresponds to the YRSZ fault trace in t = 1. B1, B2, B3 and B4 corresponds to blocks 1, 2, 3 and 4, respectively. Fault labels are as in Figure 2.2.

history. The steeply-dipping Big Creek fault has a similar orientation to the YRSZ (NW-SE) and accommodated >20 km of dextral displacement in the Late Cretaceous and is the northern boundary of the Dawson Range batholith in block 4 (**Figure 2.2**; Betsi et al 2012; Johnston 1999). Exhumation of blocks 3 and 4 along thrust or extensional faults perpendicular to the Big Creek fault could result in increased cooling rates (**Figure 2.8Bi**). There are many perpendicular thrust and extensional faults mapped within blocks 3 and 4, however there currently is no knowledge of a dominant NE-SW fault along which the crustal blocks exhumed. Perhaps the vertical uplift of blocks 3 and 4 along the BCF was due to the buoyancy of the Dawson Range batholith, resulting in isothermal exhumation and doming prior to unroofing at 85 Ma, but there still is no field evidence within blocks 3 and 4 for faults other than the BCF accommodating the uplift. Alternatively, blocks 3 and 4 may have exhumed through NW-SE extensional faulting, for example along the YRSZ, from the northwestward motion of crustal blocks of the YTT in the Cretaceous, since the fault dips shallowly to the southeast (**Figure 2.8Bii**). Even though the exact faults that exhumed blocks 3 and 4 are uncertain due to a lack of detailed field observations, exhumation through faulting is the most likely cause for their exhumation in the Late Cretaceous, c. 30 m.y. after blocks 1, 2 and 5.

The 105-100 Ma emplacement of the Dawson Range batholith suggests that blocks 3 and 4 exhumed after 100 Ma (thus after block 2), however the 112-100 Ma Whitehorse plutonic suite has also been mapped in some very localised areas within the eastern side of block 2 (Colpron et al. 2016). Nonetheless, the sampling density in the eastern side of block 2 is low therefore we are unable to resolve whether it exhumed later than the western side of block 2 because the mapped exposures of the Whitehorse plutonic suite are relatively very small, and could have been the result of very localized exhumation.

Latest Cretaceous thermal resetting

After the Late Cretaceous, the landscape in west-central Yukon has remained relatively unchanged, preserving the Carmacks Group extrusive rocks and Indian River Formation, and relatively low incision rates since c. 100 Ma (Gordey and Ryan 2005; Mortensen and Dusel-Bacon 2014; Ryan et al. 2003, 2010, 2017; Staples et al. 2016). This contrasts with low temperature thermochronology data in Alaska, SW Yukon and southern British Columbia that suggest rapid uplift and cooling in the Eocene (e.g. Cook et al. 1992; Dusel-Bacon et al. 2016; Enkelmann et al. 2017; O'Sullivan et al. 1997; Parrish et al. 1988). A few samples in this study have post-Late Cretaceous apatite ages (i.e. after the crustal blocks are required to be at the surface), meaning that the apatite system had to be reset after reaching surface temperatures. These samples were not thermally reset through burial to the point of fully resetting the apatite ages since the current landscape in the YTT dates back to the Late Cretaceous (Gordey and Ryan 2005; Mortensen and Dusel-Bacon 2014; Ryan et al. 2003, 2010, 2017; Staples et al. 2016), however they may have been partially or fully reset by hydrothermal fluids associated with Carmacks volcanism. The Late Cretaceous Carmacks Group is present in numerous places within the study area, however the spatial extent of the group is unknown (Ryan, pers. comm., 2016). Many of the numerical models require some low-temperature reheating at c. 70 Ma, probably due to the extensive volcanism during the Late Cretaceous. Blocks 1, 4, and the samples in the eastern half of block 2 require the zircon ages to be partially or completely reset, whereas the samples on the western side of block 2 only require some of the samples to have the apatite ages reset at c. 70 Ma (**Figures 2.3, 2.4, 2.6**). Forward models show that any resetting of the zircon ages in the western samples of block 2 and will yield model zircon ages that are younger than the measured ages, and resetting

of block 3 will result in younger model zircon and apatite ages (**Figures 2.4, 2.5**). Therefore, Late Cretaceous volcanism seems to have more of an effect on the eastern side of the study area. This is either because the Carmacks volcanic rocks once covered more area in the eastern side than the western side, or the samples on the western side were still at shallow depths (but at temperatures below the apatite PRZ) at c. 70 Ma, and the western side has since been slightly more eroded than the eastern side.

In some of the crustal blocks where there are apatite ages younger than 70 Ma, the ages are from a single sample (e.g. block 4), so there are not enough data to discount the possibility that the young apatite ages may instead reflect sample-specific details (e.g. broken grain or mineral zonation) that control such dates (**Figure 2.6,** Meesters and Dunai 2002; Murray et al. 2014). The numerical models presented in this study assume that the ^{4}He data represent regional cooling of an entire crustal block, however other factors may affect ^{4}He loss. Localized thermal events such as fluid flow and mineralization may partially or fully reset the ^{4}He ages, which may explain some of the anomalous data points in age-eU space that do not fit any numerical models. The YTT hosts many Jurassic to Late Cretaceous mineral deposits near samples in this study such as Minto, Casino, Sonora Gulch, White Gold and Nucleus and Revenue, many of which are associated with the Klondike assemblage (Bennett et al. 2010; Colpron and Ryan, 2010). Sample 00VN002 is located near the White Gold deposit, and has anomalously young zircon ages, however these ages are younger than 60 Ma. The rocks are required to be at the surface by 70 Ma, thus mineralization cannot be used to explain these ages. Other samples that are near mineral deposits do not appear to have been reset (i.e. do not have anomalously young zircon ages, e.g. samples 10RAYJR097 and 10RAYJR103), which are near the Coffee and Casino deposits, respectively (**Figure 2.2**; Colpron and Ryan

2010). Sample 10RAYJR103 has very young (10-12 Ma) apatite ages, however mineralization occurred in the Cretaceous, and this crustal block had to have been at the surface by 70 Ma, therefore the apatite ages cannot be explained by mineralization (Mackenzie et al. 2014). Moreover, the numerical modeling is based on the effect that accumulation and annealing of radiation damage has on diffusion kinetics in zircon and apatite, and factors other than radiation damage may contribute to ^{4}He retention in zircon and apatite, yielding anomalously old ages. Such factors include fluid inclusions and ^{4}He implantation from neighboring phases, including oxides (Flowers et al. 2009). The numerical models are also limited in the sense that the ^{4}He diffusion kinetics used are based on very localized studies (e.g. Guenthner et al. 2013) and may not be representative zircon populations in other locations. Moreover, the zircon radiation damage annealing model used is based on zircon fission track annealing, which does not account for the multiple mechanisms affecting radiation damage annealing in zircon (Geisler et al. 2001; Zhang et al. 2000).

The low-temperature thermochronometers and numerical models highlight the complex Cretaceous exhumation history in the upper crust that cannot be readily explained by erosion and normal faulting alone, which are often invoked as efficient exhumation processes (Brandon et al. 1998; Jolivet and Brun 2010; Kirby et al. 2002).

2.6.2. Implications for regional tectonics

Staples et al. (2016) proposed a late-Early Cretaceous orogenic collapse episode in west-central Yukon, expressed on the surface by Cretaceous normal faulting, the exhumation of the Australia Mountain domain from beneath the YTT and an increase in volcanic and plutonic activity (Dusel-Bacon et al. 2002; Nelson et al. 2006 and references therein; Ryan et al. 2014; Staples et al. 2013). In this model, northwestward orogen-parallel extrusion is associated with

lateral escape tectonics, in which orogen dynamics transition from orogen-normal compression to orogen-parallel extension (England and Houseman 1990; Meissner and Mooney 1998). Lateral escape of the crust has been proposed to explain the transition from mainly compressional tectonics to extensional tectonics in many orogens such as the Himalayas and Basin and Range, and is caused by the decoupling of the upper and lower crust where viscosity is low (England and Houseman 1990; Gans 1987; Tapponnier et al. 1982). However, the only field evidence of major low-angle extensional structures in the Cretaceous in the study area are the Australia Creek and Stewart River faults, and the most likely model for the late-Early Cretaceous exhumation of blocks 1 and 2 involves NE-SW contraction, which suggests that extension was localized. In the Late Cretaceous, the exhumation of blocks 3 and 4 may have been along extensional structures that were active during the NW-SE motion of the crustal blocks that characterize the Cretaceous tectonic history of the YTT, involving the many NW-SE trending strike-slip faults in the study area. Widespread extension may therefore have started after the exhumation of the Australia Mountain domain, later than the widespread late-Early Cretaceous extension proposed by Staples et al. (2016), coeval with the beginning of dextral fault motion on the Tintina in the Late Cretaceous (Gabrielse et al. 2006). However, the exhumation models in this paper and in Staples et al. (2016) require unidentified faults, and additional work on characterizing brittle faults within west-central Yukon will shed light on the Cretaceous exhumation mechanisms.

Lateral escape of the crust due to decoupling at a low-viscosity zone is also associated with lower crustal and lithospheric delamination (Meissner and Mooney 1998). Lithospheric detachment, Rayleigh-Taylor type instabilities and slab windows have been proposed as an explanation for the rapid cooling rates, flat Moho and hot, thin lithosphere in the southern

Canadian Cordillera (e.g. Bao et al. 2014; Currie et al. 2008; Thorkelson et al. 2011). These processes cause the upwelling of the asthenosphere, and this hot, low-density material triggers thermal (and possibly isostatic) uplift, and an increase in geothermal gradient and regional magmatism (DeCelles et al. 2015; Dewey 1988; Houseman and Molnar 1997; Thorkelson and Taylor 1989). The thermal uplift results in increased erosion rates and extension, directly followed by rapid cooling (England and Molnar 1990; Meissner and Mooney 1998; Ueda et al. 2012). The increase in magmatic activity throughout west-central Yukon in the late-Early Cretaceous and subsequent increase in cooling rates as resolved through low and high temperature thermochronometers suggests the late-Early to Late Cretaceous as the timing of crustal thinning in the northern Canadian Cordillera (Dusel-Bacon et al. 2002; Staples et al. 2013, 2014). Although multiple studies invoke lithospheric thinning to explain the rapid cooling rates and current thin lithosphere in the southern Canadian Cordillera in British Columbia, the (U-Th)/He data and numerical models from this study do not show an obvious spatial migration of Cretaceous exhumation or a spatial transition from lower to higher cooling and sedimentation rates that can distinguish between the different lithospheric thinning mechanisms for the northern Canadian Cordillera (e.g. Bao et al. 2014; Currie et al. 2008; Currie and Hyndman 2006; Morales and Tommasi 2011; Ueda et al. 2012). Rapid cooling of the upper crust in the late-Early to Late Cretaceous is also consistent with low-temperature thermochronology results from the Mount Nansen area (Moher 2018), and are contemporaneous with the eastward progression of upper crustal exhumation in the foreland fold and thrust belt, shown by an increase in cooling rates in the western Mackenzie Mountains in the latest Cretaceous followed by relatively rapid Paleocene cooling closer to the deformation front (Powell et al. 2016).

The Cretaceous signature of the low temperature data contrasts with the large-scale extension, exhumation and magmatism associated with lithospheric thinning in the Eocene in British Columbia and Alaska (e.g. Cook et al. 1992; Dusel-Bacon et al. 2016; Enkelmann et al. 2017; O'Sullivan et al. 1997; Parrish et al. 1988). Moreover, the lack of a late Oligocene-early Miocene exhumation event resolved by the low-temperature thermochronometers indicates that there was no thermal event in the shallow crust in west-central Yukon related to the slab window opening on the west coast of British Columbia and southwestern Yukon. Geochemical and geophysical data constrain the opening of this slab window to the early Cenozoic, causing an increase in magmatic activity, thinning of the lithosphere and high heat flow (Thorkelson et al. 2011), but this did not affect west-central Yukon, since the current landscape has not undergone major changes since the Late Cretaceous (Gordey and Ryan 2005; Ryan et al. 2003, 2010, 2017; Staples et al. 2016). The lack of exhumation events in the Cenozoic suggests that this area of the Cordillera has been isolated from the Cenozoic exhumation processes affecting Alaska, southern Yukon and British Columbia.

2.7. Conclusion

Numerical modeling of low temperature (U-Th)/He data has the potential to provide information on the timing of multiple cooling and heating events and estimate cooling rates, giving invaluable insight on shallow crustal tectonic processes. The low temperature results presented in this paper builds on previous studies that resolve the high temperature history of the YTT to give a more complete picture of the tectonothermal history of west-central Yukon (Berman et al. 2007; Knight et al. 2013; Staples et al. 2013; 2016).

The numerical models evince three main periods of cooling in west-central Yukon. The first is the Jurassic exhumation of the crustal blocks; the YTT reached the zircon PRZ in the upper crust at c. 160 Ma. According to the low temperature models, cooling rates subsequently decreased dramatically until the Cretaceous. The crustal blocks in west-central Yukon exhumed in the Cretaceous, however if the unroofing is via tectonic mechanisms, the exhumation requires currently unidentified faults. West-central Yukon is divided into two areas separated by major faults that have very different Cretaceous cooling histories, and these faults separate distinct tectonometamorphic domains. The crustal blocks north of the YRSZ and BCF must exhume before c. 110 Ma, whereas the blocks in the footwall are necessarily at mid-crustal depths, and only exhume c. 30 m.y. later. Thrusting along the YRSZ, resulting in uplift and increased erosion rates in the northern part of the study area may explain the late-Early Cretaceous exhumation. Numerical modeling corroborates the rapid late-Early Cretaceous exhumation of the underlying metamorphic core complex (block 5; Staples et al. 2013), however that model proposes widespread extensional collapse that drove the exhumation of the core complex. The numerical models presented here evince no synchronous events in the late-Early Cretaceous, but possibly in the Late Cretaceous. In the Late Cretaceous, the structurally lower blocks to the south likely exhumed as a consequence of northwestward motion of the YTT which was accommodated by NW-SE trending dextral faults such as the Big Creek fault and perpendicular thrust or extensional faults, perhaps aided by the buoyancy of widespread magmatism (e.g. Dawson Range batholith; Gabrielse et al. 2006; Johnston et al. 1999). Alternatively, the northwestward motion of the YTT may have driven the exhumation of the structurally lower panel through extension along the YRSZ. Further analysis of the brittle faults in west-central Yukon combined with local

thermochronology studies in areas within the present study area are required to distinguish between the possible exhumation processes presented in this study.

Although very broad in scale, these results define an older exhumation history compared to the Alaskan and southern Canadian Cordillera, which record a dominant Eocene collapse signature (e.g. Bao et al. 2014; Dusel-Bacon et al. 2016). A deeper understanding of the different processes governing orogenic plateau formation in the northern and southern Canadian Cordillera, notably understanding why the thermal history of the northern Canadian Cordillera lacks an Eocene signature is significant for understanding the evolution of craton margins, and the natural resources that reside there.

References

Bao, X., Eaton, D.W., and Guest, B., 2014, Plateau uplift in western Canada caused by lithospheric delamination along a craton edge: Nature Geoscience, v. 7, p. 830–833, doi: 10.1038/NGEO2270.

Barnes, J.B., and Ehlers, T.A., 2009, End member models for Andean Plateau uplift: Earth-Science Reviews, v. 97, p. 105–132, doi: 10.1016/j.earscirev.2009.08.003.

Bennett, V., Schulze, C., Ouellette, D., and Pollries, B., 2010, Deconstructing complex Au-Ag-Cu mineralization, Sonora Gulch project, Dawson Range: A Late Cretaceous evolution to the epithermal environment Sonora Gulch, *in*: MacFarlane, K.E., Weston, L.H., and Blackburn, L.R., eds., Yukon Exploration and Geology 2009: Yukon Geological Survey, p. 23-45.

Betsi, T.B., Lentz, D., Mcinnes, B., and Evans, N.J., 2012, Emplacement ages and exhumation rates for intrusion-hosted Cu–Mo–Sb–Au mineral systems at Freegold Mountain (Yukon, Canada): assessment from U–Pb , Ar–Ar , and (U–Th)/He geochronometers: Canadian Journal of Earth Sciences, v. 49, p. 653–670, doi: 10.1139/E2012-009.

Beranek, L.P., and Mortensen, J.K., 2011, The timing and provenance record of the Late Permian Klondike orogeny in northwestern Canada and arc - continent collision along western North America: Tectonics, v. 30, p. 1–23, doi: 10.1029/2010TC002849.

Beranek, L.P., Mortensen, J.K., Orchard, M.J., and Ullrich, T., 2010, Provenance of North American Triassic strata from west-central and southeastern Yukon : correlations with coeval strata in the Western Canada Sedimentary Basin and Canadian Arctic: Canadian Journal of Earth Sciences, v. 73, p. 53–73, doi: 10.1139/E09-065.

Berman, R.G., Ryan, J.J., Gordey, S.P., and Villeneuve, M., 2007, Permian to Cretaceous polymetamorphic evolution of the Stewart River region, Yukon-Tanana terrane, Yukon, Canada: P-T evolution linked with in situ SHRIMP monazite geochronology: Journal of meramorphic geology, vol. 25, p. 803–827, doi: 10.1111/j.1525-1314.2007.00729.x.

Brandon, M.T., Roden-Tice, M.K., and Garver, J.I., 1998, Late Cenozoic exhumation of the Cascadia accretionnary wedge in the Olympic mountains, northwest Washington State: Geological Society of America Bulletin, v. 110, p. 985–1009, doi: 10.1130/0016-7606(1998)110<0985:LCEOTC>2.3.CO;2.

Clift, P.D., Hodges, K. V., Heslop, D., Hannigan, R., Van Long, H., and Calves, G., 2008, Correlation of Himalayan exhumation rates and Asian monsoon intensity: Nature Geoscience, v. 1, p. 875–880, doi: 10.1038/ngeo351.

Colgan, J.P., and Henry, C.D., 2009, Rapid middle Miocene collapse of the Mesozoic orogenic plateau in north-central Nevada: International Geology Review, v. 51, 920-961 p., doi: 10.1080/00206810903056731.

Colpron, M., Crowley, J.L., Gehrels, G., Long, D.G.F., Murphy, D.C., Beranek, L., and Bickerton, L., 2015, Birth of the northern Cordilleran orogen, as recorded by detrital zircons in Jurassic synorogenic strata and regional exhumation in Yukon: Lithosphere, p. 541–562, doi: 10.1130/L451.1.

Colpron, M., Gladwin, K., Johnston, S.T., Mortensen, J.K., and Gehrels, G.E., 2005, Geology and juxtaposition history of the Yukon-Tanana, Slide Mountain, and Cassiar terranes in the Glenlyon area of central Yukon: Canadian Journal of Earth Sciences, v. 42, p. 1431–1448, doi: 10.1139/E05-046.

Colpron, M., Israel, S., Murphy, D., Pigage, L., and Moynihan, D., 2016, Yukon Bedrock Geology Map: Yukon Geological Survey, Open File 2016-1, scale 1:1,000,000, map and legend.

Colpron, M., Nelson, J. L., and Murphy, D.C., 2007, Northern Cordilleran terranes and their interactions through time: GSA Today, v. 17, p. 4–10, doi: 10.1130/GSAT01704-5A.1.

Colpron, M. and Ryan, J.J., 2010, Bedrock geology of southwest McQuesten (NTS 115P) and part of northern Carmacks (NTS 115I) map area, *in:* MacFarlane, K.E., Weston, L.H., and Blackburn, L.R., eds., Yukon Exploration and Geology 2009: Yukon Geological Survey, p. 159-184.

Cook, F.A., Varsek, J.L., Clowes, R.M., Kanasewich, E.R., Spencer, C.S., Parrish, R.R., Brown, R.L., Carr, S.D., Johnson, B.J., and Price, R.A., 1992, Lithoprobe crustal reflection cross section of the southern Canadian Cordillera, 1, Foreland thrust and fold belt to Fraser River fault: Tectonics, v. 11, p. 12–35, doi: 10.1029/91TC02332.

Currie, C.A., Huismans, R.S., and Beaumont, C., 2008, Thinning of continental backarc lithosphere by flow-induced gravitational instability: Earth and Planetary Science Letters, v. 269, p. 436–447, doi: 10.1016/j.epsl.2008.02.037.

Currie, C.A., and Hyndman, R.D., 2006, The thermal structure of subduction zone back arcs: Journal of Geophysical Research: Solid Earth, v. 111, p. 1–22, doi: 10.1029/2005JB004024.

Dai, J., Wang, C., Hourigan, J., Li, Z., and Zhuang, G., 2013, Exhumation History of the Gangdese Batholith, Southern Tibetan Plateau: Evidence from Apatite and Zircon (U-Th)/He Thermochronology: The Journal of Geology, v. 121, p. 155–172, doi: 10.1086/669250.

DeCelles, P.G., Zandt, G., Beck, S.L., Currie, C.A., Ducea, M.N., Kapp, P., Gehrels, G.E., Carrapa, B., Quade, J., and Schoenbohm, L.M., 2015, Cyclical orogenic processes in the Cenozoic central Andes, *in* DeCelles, P.G., Ducea, M.N., Carrapa, B., and Kapp, P.A., eds., Geodynamics of a Cordilleran Orogenic System: The Central Andes of Argentina and Northern Chile: Geological Society of America Memoir 212, p. 459–490, doi:10.1130 /2015.1212(22).

Dewey, J.F., 1988, Extensional collapse of orogens: Tectonics, v. 7, p. 1123–1139, doi: 10.1029/TC007i006p01123.

Dodson, M.H., 1973, Closure temperature in cooling geochronological and petrological systems: Contributions to Mineralogy and Petrology, v. 40, p. 259–274, doi: 10.1007/BF00373790.

Dusel-Bacon, C., Bacon, C.R., Sullivan, P.B.O., and Day, W.C., 2016, Apatite fission-track evidence for regional exhumation in the subtropical Eocene, block faulting, and localized fluid flow in east-central Alaska: Canadian Journal of Earth Sciences, v. 280, p. 260–280.

Dusel-Bacon, C., Hansen, V.L., and Scala, J.A., 1995, High-pressure amphibolite facies dynamic metamorphism and the Mesozoic tectonic evolution of an ancient continental margin, east-central Alaska: Journal of Metamorphic Geology, v. 13, p. 9–24.

Dusel-Bacon, C., Hopkins, M.J., Mortensen, J.K., Daschevsky, S.S., Bressler, J.R., and Day, W.C., 2006, Paleozoic tectonic and metallogenic evolution of the pericratonic rocks of east-central Alaska and adjacent Yukon, *in* Colpron, M., and Nelson, J.L., eds., Paleozoic Evolution and Metallogeny of Pericratonic Terranes at the Ancient Pacific

Margin of North America, Canadian and Alaskan Cordillera: Geological Association of Canada Special Paper, v. 45, p. 25–74.

Dusel-Bacon, C., Lanphere, M.A., Sharp, W.D., Layer, P.W., and Hansen, V.L., 2002, Mesozoic thermal history and timing of structural events for the Yukon-Tanana Upland, east-central Alaska: $^{40}Ar/^{39}Ar$ data from metamorphic and plutonic rocks: Canadian Journal of Earth Sciences, v. 1051, p. 1013–1051, doi: 10.1139/E02-018.

England, P., and Molnar, P., 1990, Surface uplift, uplift of rocks, and exhumation of rocks: Geology, v. 18, p. 1173-1177.

England, P., and Houseman, G., 1990, Extension during continental convergence, with application to the Tibetan Plateau: Journal of Geophysical Research, v. 94, p. 17561–17579, doi: 10.1029/JB094iB12p17561.

Enkelmann, E., Piestrzeniewicz, A., Falkowski, S., Stübner, K., and Ehlers, T.A., 2017, Thermochronology in southeast Alaska and southwest Yukon: Implications for North American Plate response to terrane accretion: Earth and Planetary Science Letters, v. 457, p. 348–358, doi: 10.1016/j.epsl.2016.10.032.

Fan, M., and Carrapa, B., 2014, Late Cretaceous-early Eocene Laramide uplift, exhumation, and basin subsidence in Wyoming: Crustal responses to flat slab subduction: Tectonics, v. 33, p. 509–529, doi: 10.1002/2012TC003221.

Farley, K.A., 2002, (U-Th)/He Dating: Techniques, Calibrations, and Applications: Reviews in Mineralogy and Geochemistry, v. 47, p. 819–844, doi: 10.2138/rmg.2002.47.18.

Farley, K.A., 2000, Helium diffusion from apatite: General behavior as illustrated by Durango fluorapatite: Journal of Geophysical Research: Solid Earth, v. 105, p. 2903–2914, doi: 10.1029/1999JB900348.

Flowers, R.M., Ketcham, R.A., Shuster, D.L., and Farley, K.A., 2009, Apatite (U-Th)/He thermochronometry using a radiation damage accumulation and annealing model: Geochimica et Cosmochimica Acta, v. 73, p. 2347–2365, doi: 10.1016/j.gca.2009.01.015.

Foster, L., Cushing, W., Keith, E.C., and Laird, J., 1985, Early Mesozoic tectonic history of the boundary area, east-central Alaska: Geophysical Research Letters, v. 12, p. 553–556.

Gabrielse, H., Murphy, D.C., and Mortensen, J.K., 2006, Cretaceous and Cenozoic dextral orogen-parallel displacements, magmatism and paleogeography, northcentral Canadian Cordillera, *in* Haggart, J.W., Monger, J.W.H., and Enkin, R.J., eds., Paleogeography of the North American Cordillera: Evidence for and against Large-Scale Displacements: Geological Association of Canada Special Paper, v. 46, p. 255–276.

Gans, P.B., 1987, An open-system, two-layer crustal stretching model for the Eastern Great Basin: Tectonics, v. 6, p. 1–12, doi: 10.1029/TC006i001p00001.

Geisler, T., Pidgeon, R.T., van Bronswijk, W., and Pleysier, R., 2001, Kinetics of thermal recovery and recrystallization of partially metamict zircon: a Raman spectroscopic study: European Journal of Mineralogy, v. 13, p. 1163–1176, doi: 10.1127/0935-1221/2001/0013-1163.

Godwin, C.I., 1975, Alternative interpretations for the Casino Complex and Klotassin Batholith in the Yukon Crystalline Terrane: Canadian Journal of Earth Sciences, v. 12, p. 1910-1916, doi: 10.1139/e75-168.

Gordey, S.P., and Ryan, J.J., 2005, Geology, Stewart River area (115 N, 115-O and part of 115J), Yukon Territory: Geological Survey of Canada, Open File 4970, scale 1:100

000, 1 sheet, doi:10.4095/221149.

Guenthner, W.R., Reiners, P.W., Decelles, P.G., and Kendall, J., 2015, Sevier belt exhumation in central Utah constrained from complex zircon (U-Th)/He data sets: Radiation damage and He inheritance effects on partially reset detrital zircons: GSA Bulletin, v. 127, p. 323–348, doi: 10.1130/B31032.1.

Guenthner, W.R., Reiners, P.W., Ketcham, R.A., Nasdala, L., and Giester, G., 2013, Helium diffusion in natural zircon: radiation damage, anisotropy, and the interpretation of zircon (U-Th)/He thermochronology: American Journal of Science, v. 313, p. 145–198, doi: 10.2475/03.2013.01.

Guenthner, W.R., Reiners, P.W., and Tian, Y., 2014, Interpreting date-eU correlations in zircon (U-Th)/He datasets: A case study from the Longmen Shan, China: Earth and Planetary Science Letters, v. 403, p. 328–339, doi: 10.1016/j.epsl.2014.06.050.

Hansen, V.L., and Dusel-Bacon, C. 1998, Structural and kinematic evolution of the Yukon-Tanana upland tectonites, east-central Alaska: A record of late Paleozoic to Mesozoic crustal assembly: GSA Bulletin, v. 110, p. 211–230.

Hansen, V.L., Heizler, M.T., and Harrison, T.M., 1991, Mesozoic thermal evolution of the Yukon-Tanana Composite Terrane: New evidence from $^{40}Ar/^{39}Ar$ data: Tectonics, v. 10, p. 51–76.

Hardebol, N.J., Pysklywec, R.N., and Stephenson, R., 2012, Small-scale convection at a continental back-arc to craton transition: Application to the southern Canadian Cordillera: Journal of Geophysical Research: Solid Earth, v. 117, p. 1–18, doi: 10.1029/2011JB008431.

Harrison, T.M., Zeitler, P.K., 2005, Fundamentals of Noble Gas Thermochronometry:

Reviews in Mineralogy and Geochemistry, v. 58, p. 123–149, doi: 10.2138/rmg.2005.58.5.

Hayward, N., Miles, W. and Oneschuk, D., 2011, Geophysical Series, Regional Geophysical Compilation Project, Yukon Plateau, Yukon, Parts of NTS 105, 106, 115, and 116: Geological Survey of Canada, Open File 6959, scale 1:750 000, 2 sheets, p.1, doi: 10.4095/288586.

Herman, F., Cox, S.C., and Kamp, P.J.J., 2009, Low-temperature thermochronology and thermokinematic modeling of deformation, exhumation, and development of topography in the central Southern Alps, New Zealand: Tectonics, v. 28, doi: 10.1029/2008TC002367.

Houseman, G.A., and Molnar, P., 1997, Gravitational (Rayleigh-Taylor) instability of a layer with non-linear viscosity and convective thinning of continental lithosphere: Geophysical Journal International, 128, p. 125–150.

Hunt, P.A. and Roddick, J.C., 1992. A compilation of K-Ar ages, Report 21. *In*: Radiogenic Age and Isotopic Studies Report 5: Geological Survey of Canada, Paper 91-2, p. 207-261.

Hyndman, R.D., and Currie, C.A., 2011, Why is the North America Cordillera high? Hot backarcs, thermal isostasy, and mountain belts: Geology, v. 39, p. 783–786, doi: 10.1130/G31998.1.

Hyndman, R.D., Flück, P., Mazzotti, S., Lewis, T.J., Ristau, J., and Leonard, L., 2005, Current tectonics of the northern Canadian Cordillera: v. 42, p. 1117–1136, doi: 10.1139/E05-023.

Israel, S., Murphy, D., Bennett, V., Mortensen, J., and Crowley, J., 2011, New insights into

the geology and mineral potential of the Coast Belt in southwestern Yukon, *in*: MacFarlane, K.E., Weston, L.H., and Relf, C., eds., Yukon Exploration and Geology 2010: Yukon Geological Survey, p. 101-123.

Johnston, S.T., 1999, Large-scale coast-parallel displacements in the Cordillera: A granitic resolution to a paleomagnetic dilemma: Journal of Structural Geology, v. 21, p. 1103–1108, doi: 10.1016/S0191-8141(99)00015-2.

Johnston, S.T., Mortensen, James, K., and Erdmer, P., 1996, Igneous and metaigneous age constraints for the Aishihik metamorphic suite of southwest Yukon: Canadian Journal of Earth Sciences, v. 33, p. 1543–1555.

Johnston, S.T., and Shives, R.B.K., 1995, Interpretation of an airborne multiparameter geophysical survey of the northern Dawson Range, central Yukon: A progress report, *in* Yukon Exploration and Geology, 1994: Exploration and Geological Services Division, Yukon, Indian and Northern Affairs Canada, p. 105-111.

Jolivet, L., Brun, J.-P., 2010, Cenozoic geodynamic evolution of the Aegean: International Journal of Earth Sciences, v. 99, p. 109–138, doi: 10.1007/s00531-008-0366-4.

Joyce, N.L., 2002, Geologic setting, nature, and structural evolution of intrusion-hosted Au-bearing quartz veins at the Longline occurence, Moosehorn Range, west-central Yukon Territory [M.Sc. thesis]: University of British Columbia, 199 p.

Joyce, N.L., Ryan, J.J., Colpron, M., Hart, C.J.R., Murphy, D.C., 2015, A compilation of $^{40}Ar/^{39}Ar$ age determinations for igneous and metamorphic rocks, and mineral occurrences from central and southeast Yukon: Geological Survey of Canada Open-File 7924, 229 p., doi: 10.4095/297446.

Ketcham, R.A., 2005, Forward and Inverse Modeling of Low-Temperature

Thermochronometry Data: Reviews in Mineralogy and Geochemistry, v. 58, p. 275–314, doi: 10.2138/rmg.2005.58.11.

Ketcham, R.A., 2012, Basin thermal history analysis using (U-Th)/He thermochronometry, *in* Harris, N.B., and Peters, K. E., eds., Analyzing the Thermal History of Sedimentary Basins: Methods and Case Studies, SEPM Special Publication, v. 103, p. 105–123.

Kirby, E., Reiners, P.W., Krol, M.A., Whipple, K.X., Hodges, K. V, Farley, K.A., Tang, W., and Chen, Z., 2002, Late Cenozoic evolution of the eastern margin of the Tibetan Plateau: Inferences from $^{40}Ar/^{39}Ar$ and (U-Th)/He thermochronology: Tectonics, v. 21, p. 1-1–1-20.

Knight, E., Schneider, D.A., and Ryan, J., 2013, Thermochronology of the Yukon-Tanana Terrane, west-central Yukon : Evidence for Jurassic Extension and exhumation in the northern Canadian Cordillera: The Journal of Geology, v. 121, p. 371–400, doi: 10.1086/670721.

Lowey, G.W., and Hills, L. V., 1988, Lithofacies, petrography and environments of deposition, Tantalus formation (lower Cretaceous) Indian River area, west-central Yukon: Bulletin of Canadian Petroleum Geology, v. 36, p. 296–310.

Mackenzie, D., Craw, D., and Finnigan, C., 2014, Structural controls on alteration and mineralization at the Coffee gold deposits, Yukon, *in*: MacFarlane, K.E., Nordling, M.G., and Sack, P.J., eds., Yukon Geological Survey, p. 119–131.

Mackenzie, D.J., Craw, D., and Mortensen, J., 2008, Structural controls on orogenic gold mineralisation in the Klondike goldfield, Canada: Mineralum Deposita, v. 43, p. 435–448, doi: 10.1007/s00126-007-0173-z.

Meesters, A.G.C.A., and Dunai, T., 2002, Solving the production – diffusion equation for

finite diffusion domains of various shapes Part II. Application to cases with a-ejection and nonhomogeneous distribution of the source: Chemical Geology, v. 186, p. 333–344, doi: 10.1016/S0009-2541(01)00422-3.

Meissner, R., and Mooney, W., 1998, Weakness of the lower continental crust: a condition for delamination, uplift, and escape: Tectonophysics, v. 296, p. 47–60, doi: 10.1016/S0040-1951(98)00136-X.

Mezger, J.E., Chacko, T., and Erdmer, P., 2001, Metamorphism at a late Mesozoic accretionary margin: a study from the Coast Belt of the North American Cordillera: Journal of Metamorphic Geology, v. 19, p. 121–137, doi: 10.1046/j.0263-4929.2000.00300.x.

Moher, M., 2018, (U-Th)/He thermochronology of the Aishihik batholith, central Yukon: Evidence for stable crust in the Cretaceous [M.Sc. thesis]: University of Ottawa, 69 p.

Morales, L.F.G., and Tommasi, A., 2011, Composition, textures, seismic and thermal anisotropies of xenoliths from a thin and hot lithospheric mantle (Summit Lake, southern Canadian Cordillera): Tectonophysics, v. 507, p. 1–15, doi: 10.1016/j.tecto.2011.04.014.

Mortensen, J.K., 1990, Geology and U-Pb geochronology of the Klondike District, west-central Yukon Territory; Canadian Journal of Earth Sciences, v. 27, p. 903-914, doi: 10.1139/e90-093.

Mortensen, J.K., and Dusel-Bacon, C. 2014. Nature and U-Pb zircon ages of mid-Cretaceous calderas and tuffs in eastern Alaska and western Yukon: Implications for landscape evolution in the northern Cordillera. *In* Geological Society of America Abstracts with Programs, v. 46, no. 6, p. 794.

Murphy, D. C., Mortensen, J. K., Piercey, S. J., Orchard, M. J., and Gehrels, G. E., 2006, Mid-Paleozoic to early Mesozoic tectonostratigraphic evolution of Yukon-Tanana and Slide Mountain terranes and affiliated overlap assemblages, Finlayson Lake massive sulphide district, southeastern Yukon, *in* Colpron, M., and Nelson, J. L., eds., Paleozoic evolution and metallogeny of pericratonic terranes at the ancient Pacific margin of North America, Canadian and Alaskan cordillera. Geological Association of Canada Special Paper 45, p. 75–105.

Murray, K.E., Orme, D.A., and Reiners, P.W., 2014, Effects of U-Th-rich grain boundary phases on apatite helium ages: Chemical Geology, v. 390, p. 135–151, doi: 10.1016/j.chemgeo.2014.09.023.

Nelson, J.L., Colpron, M., and Israel, S., 2013, The Cordillera of British Columbia, Yukon, and Alaska: Tectonics and Metallogeny *in* Colpron, M., Bissig, T., Rusk, B.G., and Thompson, J.H.F., eds., Tectonics, Metallogeny, and Discovery: The North American Cordillera and similar accretionary settings: Society of Economic Geologists Special Publication 17, p. 53–109, doi: 10.1017/CBO9781107415324.004.

Nelson, J. L., Colpron, M., Piercey, S. J., Dusel-Bacon, C., Murphy, D. C., and Roots, C. F., 2006, Paleozoic tectonic and metallogenetic evolution of pericratonic terranes in Yukon, northern British Columbia and eastern Alaska, *in* Colpron, M., and Nelson, J.L., eds., Paleozoic Evolution and Metallogeny of Pericratonic Terranes at the Ancient Pacific Margin of North America, Canadian and Alaskan Cordillera: Geological Association of Canada Special Paper, v. 45, 323-360.

O'Sullivan, P.B., Murphy, J.M., and Blythe, A.E., 1997, Late Mesozoic and Cenozoic thermotectonic evolution of the central Brooks Range and adjacent North Slope

foreland basin, Alaska : Including fission track results from the Trans-Alaska Crustal Transect (TACT): v. 102, p. 20821–20845.

Parrish, R.R., Carr, S.D., and Parkinson, D.L., 1988, Eocene extensional tectonics and geochronology of the southern Omineca belt, British Columbia and Washington: Tectonics, v. 7, p. 181–212.

Pavlis, T.L., Sisson, V.B., Foster, H.L., Nokleberg, W.J., and Plafker, G., 1993, Mid-Cretaceous extensional tectonics of the Yukon-Tanana terrane, Trans-Alaska Crustal Transect (TACT), east-central Alaska: Tectonics, v. 12, p. 103–122.

Piercey, S.J., and Colpron, M., 2009, Composition and provenance of the Snowcap assemblage , basement to the Yukon-Tanana terrane, northern Cordillera : Implications for Cordilleran crustal growth: Geosphere, p. 439–464, doi: 10.1130/GES00505.1.

Platt, J.P., 1986, Dynamics of orogenic wedges and the uplift of high-pressure metamorphic rocks: Geological Society of America Bulletin, v. 97, p. 1037–1053.

Powell, J., Schneider, D., Stockli, D., and Fallas, K., 2016, Zircon (U-Th)/He thermochronology of Neoproterozoic strata from the Mackenzie Mountains, Canada: Implications for the Phanerozoic exhumation and deformation history of the northern Canadian Cordillera: Tectonics, v. 35, p. 663–689, doi: 10.1002/2015TC003989.

Reiners, P.W., 2002, (U-Th)/He chronometry experiences a renaissance: EOS Transactions American Geophysical Union, v. 83, p. 21,26-27, doi: 10.1029/2002EO000012.

Reiners, P.W., 2005, Zircon (U-Th)/He Thermochronometry: Reviews in Mineralogy and Geochemistry, v. 58, p. 151–179, doi: 10.2138/rmg.2005.58.6.

Reiners, P.W., and Brandon, M.T., 2006, Using thermochronology to understand orogenic erosion: Annual Review of Earth and Planetary Sciences, v. 34, p. 419–466, doi:

10.1146/annurev.earth.34.031405.125202.

Reiners, P.W., and Farley, K.A., 2001, Influence of crystal size on apatite (U-Th)/He thermochronology: An example from the Bighorn Mountains, Wyoming: Earth and Planetary Science Letters, v. 188, p. 413–420, doi: 10.1016/S0012-821X(01)00341-7.

Reiners, P.W., Spell, T.L., Nicolescu, S., and Zanetti, K.A., 2004, Zircon (U-Th)/He thermochronometry: He diffusion and comparisons with $^{40}Ar/^{39}Ar$ dating: Geochimica et Cosmochimica Acta, v. 68, p. 1857–1887, doi: 10.1016/j.gca.2003.10.021.

Ring, U., Brandon, M.T., Willett, S.D., and Lister, G.S., 1999, *in* Ring, U., Brandon, M.T., Lister, G.S., and Willett, S.D.,eds., Exhumation Processes: Normal Faulting, Ductile Flow and Erosion: Geological Society, London, Special Publications, v. 154, 1-27.

Ryan, J.J., Colpron, M., and Hayward, N. 2010. Geology, southwestern McQuesten and parts of northern Carmacks, Yukon: Geological Survey of Canada, Canadian Geoscience Map 7, scale 1:125,000, 1 sheet, doi:10.4095/287154.

Ryan, J.J., and Gordey, S.P., 2004, Geology, Stewart River Area (Parts of 115N/1,2,7,8 and 115-O/2-12), Yukon Territory: Geological Survey of Canada Open File 4641, scale 1: 100,000, 1 sheet, doi: 10.4095/215555.

Ryan, J.J., Gordey, S.P., Glombick, P., Piercey, S.J., and Villeneuve, M.E., 2003, Update on bedrock geological mapping of the Yukon-Tanana terrane, southern Stewart River map area, Yukon Territory: Natural Resources Canada, Geological Survey of Canada, Current Research 2003-A9, 7 p.

Ryan, J.J., Hayward, N., and Jackson, L.E., 2017, Landscape antiquity and Cenozoic drainage development of southern Yukon , through restoration modeling of the Tintina: Canadian Journal of Earth Sciences, v. 54, p. 1085–1100.

Ryan, J.J., Zagorevski, A., Roots, C.F., and Joyce, N., 2014, Paleozoic tectonostratigraphy of the northern Stevenson Ridge area, Yukon Paleozoic tectonostratigraphy of the northern Stevenson Ridge area, Yukon: Geological Survey of Canada, Current Research 2014-4, 13 p. doi:10.4095/293924

Ryan, J J; Zagorevski, A; Williams, S P; Roots, C; Ciolkiewicz, W; Hayward, N; Chapman, J B., 2013, Geology, Stevenson Ridge (northeast part), Yukon: Geological Survey of Canada, Canadian Geoscience Map 116, (ed. 2, Prelim.), scale 1:100,000, 1 sheet, https://doi.org/10.4095/292407

Shuster, D.L., Flowers, R.M., and Farley, K.A., 2006, The influence of natural radiation damage on helium diffusion kinetics in apatite: Earth and Planetary Science Letters, v. 249, p. 148–161, doi: 10.1016/j.epsl.2006.07.028.

Silberling, N.J.; Jones, D.L.; Monger, J.W.H.; and Coney, P.J, 1992, Lithotectonic terrane map of the North American Cordillera: USGS Miscellaneous Investigations Map 2176, scale 1:5,000,000, 2 sheets.

Spencer, S., Kohn, B., Gleadow, A., Norman, M., Belton, D., and Carter, T. 2004, The importance of residing in a good neighbourhood: rechecking the rules of the game for apatite (U-Th)/He thermochronometry: Abstract Volume of the 10th International Conference on Fission Track Dating and Thermochronology, Amsterdam, pp. 20.

Spiegel, C., Kohn, B., Belton, D., Berner, Z., and Gleadow, A., 2009, Apatite (U-Th-Sm)/He thermochronology of rapidly cooled samples: The effect of He implantation: Earth and Planetary Science Letters, v. 285, p. 105–114, doi: 10.1016/j.epsl.2009.05.045.

Staples, R.D., Gibson, H.D., Berman, R.G., Ryan, J.J., and Colpron, M., 2013, A window into the Early to mid-Cretaceous infrastructure of the Yukon-Tanana terrane recorded

in multi-stage garnet of west- central Yukon, Canada: Journal of Metamorphic Geology, v. 31, p. 729–753, doi: 10.1111/jmg.12042.

Staples, R.D., Gibson, H.D., Colpron, M., and Ryan, J.J., 2016, An orogenic wedge model for diachronous deformation, metamorphism, and exhumation in the hinterland of the northern Canadian Cordillera: Lithosphere, v. 8, p. 165–184, doi: 10.1130/L472.1.

Staples, R.D., Murphy, D.C., Gibson, H.D., Colpron, M., Berman, R.G., and Ryan, J.J., 2014, Middle Jurassic to earliest Cretaceous mid-crustal tectono-metamorphism in the northern Canadian Cordillera: Recording foreland-directed migration of an orogenic front: GSA Bulletin, v. 126, p. 1511–1530, doi: 10.1130/B31037.1.

Stockli, D.F., 2005, Application of Low-Temperature Thermochronometry to Extensional Tectonic Settings: Reviews in Mineralogy and Geochemistry, v. 58, p. 411–448, doi: 10.2138/rmg.2005.58.16.

Stockli, D.F., Farley, K.A., and Dumitru, T.A., 2000, Calibration of the apatite (U-Th)/He thermochronometer on an exhumed fault block, White Mountains, California: Geology, v. 28, p. 983–986, doi: 10.1130/0091-7613(2000)28<983:COTAHT>2.0.CO;2.

Stüwe, K., 2007, Geodynamics of the Lithosphere: an Introduction: Heidelberg, Springer, 493 p.

Tapponnier, P., Peltzer, G., Le Dain, A.Y., Armijo, R., and Cobbold, P., 1982, Propagation extrusion tectonics in Asia: New insights from simple experiments with plasticine: Geology, v. 10, p. 611–616, doi: 10.1130/0091-7613(1982)10<611:PETIAN>2.0.CO;2.

Thiede, R.C., Bookhagen, B., Arrowsmith, J.R., Sobel, E.R., and Strecker, M.R., 2004, Climatic control on rapid exhumation along the Southern Himalayan Front: Earth and Planetary Science Letters, v. 222, p. 791–806, doi: 10.1016/j.epsl.2004.03.015.

Thorkelson, D.J., Madsen, J.K., and Sluggett, C.L., 2011, Mantle flow through the Northern Cordilleran slab window revealed by volcanic geochemistry: Geology, v.39, p. 267–270.

Thorkelson, D.J., and Taylor, R.P., 1989, Cordilleran slab windows: Geology, v. 17, p. 833–836.

Ueda, K., Gerya, T. V, and Burg, J.-P., 2012, Delamination in collisional orogens: Thermomechanical modeling: Journal of Geophysical Research: Solid Earth, v. 117, B08202, doi: 10.1029/2012JB009144.

Vice, L., 2017, Late Cretaceous to Paleocene evolution of the Blanchard River assemblage, southwest Yukon; implications for Mesozoic accretionary processes in the northwestern Cordillera [M.Sc. thesis]: Simon Fraser University, 231 p.

Wheeler, J.O., and McFeely, P., 1991, Tectonic assemblage map of the Canadian Cordillera and adjacent parts of the United States of America: Geological Survey of Canada map 1712A, scale 1 : 2,000,000, 2 sheets.

Willett, S.D., 1999, Orogeny and orography: The effects of erosion on the structure of mountain belts: Journal of Geophysical Research: Solid Earth, v. 104, p. 28957–28981, doi: 10.1029/1999JB900248.

Wolfe, M.R., and Stockli, D.F., 2010, Zircon (U-Th)/He thermochronometry in the KTB drill hole, Germany, and its implications for bulk He diffusion kinetics in zircon: Earth and Planetary Science Letters, v. 295, p. 69–82, doi: 10.1016/j.epsl.2010.03.025.

Zhang, M., Salje, E.K.H., Capitani, G.C., Leroux, H., Clark, A.M., Schluter, J., and Ewing, R.C., 2000, Annealing of alpha-decay damage in zircon: a Raman spectroscopic study: Journal of Physics: Condensed Matter, v. 12, p. 3131–3148, doi: 10.1088/0953-

8984/12/13/321.

Appendix

Text A1. Zircon and Apatite (U-Th-Sm)/He Methodology

Zircon in **Table 2.2** with an asterix and apatite in **Table 2.3** were analyzed at the (U-Th)/He Thermochronology Research and Instrumentation Laboratory at the University of Colorado in Boulder (USA).

Individual mineral grains were handpicked using a Leica M165 binocular microscope equipped with a calibrated digital camera and capable of both reflected and transmitted, polarized light. The grains were screened for quality, including crystal size, shape, and the presence of inclusions. Zircon were measured for their axial dimensions and photo documented prior to analysis. After characterization, grains were placed into small Nb tubes that were then crimped on both ends. This Nb packet is then loaded into an ASI Alphachron ^{4}He extraction and measurement line. The packet is placed in the UHV extraction line (~3x10^{-8} torr) and heated with a diode laser to ~800-1100°C for 5 to 10 min to extract the radiogenic ^{4}He. The degassed ^{4}He is then spiked with approximately 13 ncc of pure ^{3}He, cleaned via interaction with two SAES getters, and analyzed on a Balzers PrismaPlus QME 220 quadrupole mass spectrometer. Degassed grains are then removed from the line, and taken to a Class 10 clean lab for dissolution. Apatite grains, still enclosed in the Nb tubes, are placed in 1.5 mL Cetac vials, spiked with a ^{235}U-^{230}Th tracer in HNO_3, capped, and baked in a lab oven at 80°C for 2 h. Zircon and apatite with inclusions are dissolved using Parr large-capacity dissolution vessels in a multi-step acid-vapor dissolution process. Grains (including the Nb tube) are placed in Ludwig-style Savillex vials, spiked with a ^{235}U-^{230}Th tracer, and mixed with 200 µl of Optima grade HF. The vials are then capped, stacked in a 125 mL Teflon liner, placed in a Parr dissolution vessel, and baked at 220°C for 72 h. After cooling, the vials are

uncapped and dried down on a 90°C hot plate until dry. The vials then undergo a second round of acid-vapor dissolution, this time with 200 µl of Optima grade HCl in each vial that is baked at 200°C for 24 h. Vials are then dried down a second time on a hot plate. Once dry, 200 µl of a 7:1 HNO_3:HF mixture is added to each vial, the vial is capped, and cooked on the hot plate at 90°C for 4 h. Once the minerals are dissolved, regardless of the dissolution process, they are diluted with 1 to 3 mL of doubly-deionized water, and taken to the ICP-MS lab for analysis. Mineral standards of Durango Apatite (31.5 Ma) and Fish Canyon Tuff Zircon (28.2 Ma) are routinely analyzed (degassed and dissolved) in conjunction with the samples with each run to ensure data integrity. Sample solutions, along with standards and blanks, are analyzed for U, Th, and Sm content using a Thermo Element 2 magnetic sector mass spectrometer. Once the U, Th, and Sm contents have been measured, ^{4}He dates and all associated data are calculated in a custom spreadsheet.

The remaining zircon were analyzed at the (U-Th)/He Laboratory at the University of Texas Jackson School of Geosciences (Austin, USA) using laboratory procedures described in Stockli and others (2000) and House and others (2000). Single inclusion-free grains of zircon were wrapped in Pt foil, heated for 10 minutes at 1290°C and reheated until >99% of the ^{4}He was extracted from the crystal with a continuous mode Nd-YAG laser in a stain-less steel ultra-high vacuum noble gas extraction and purification line. For each single-grain aliquot, ^{4}He was extracted, spiked with ^{3}He for isotope dilution, concentrated and purified with in a Janis cryogenic trap, released, and the ^{3}He /^{4}He ratio was subsequently measured with a Balzers Prisma QMS-200 quadrupole mass spectrometer. All ages were calculated using standard α-ejection corrections using morphometric analyses (Farley et al. 1996). After laser heating, zircon were unwrapped from Pt foil and dissolved using HF-HNO3 and HCl

pressure vessel digestion procedures. U, Th, and Sm concentrations were determined by isotope dilution ICP-MS analysis using a ThermoElement2 mass spectrometer. Mean (U-Th-Sm)/He ages were calculated on the basis of 2-4 zircon replicate analyses. Reported age uncertainties (2σ) reflect the reproducibility of replicate analyses of laboratory standard samples (Farley et al. 2001). Estimated analytical uncertainties are ~8% (2σ) for zircon ^{4}He ages (Reiners et al. 2002). Ft factor refers to α-ejection correction factor as described in Farley and others (1996), assuming homogenous U and Th distribution.

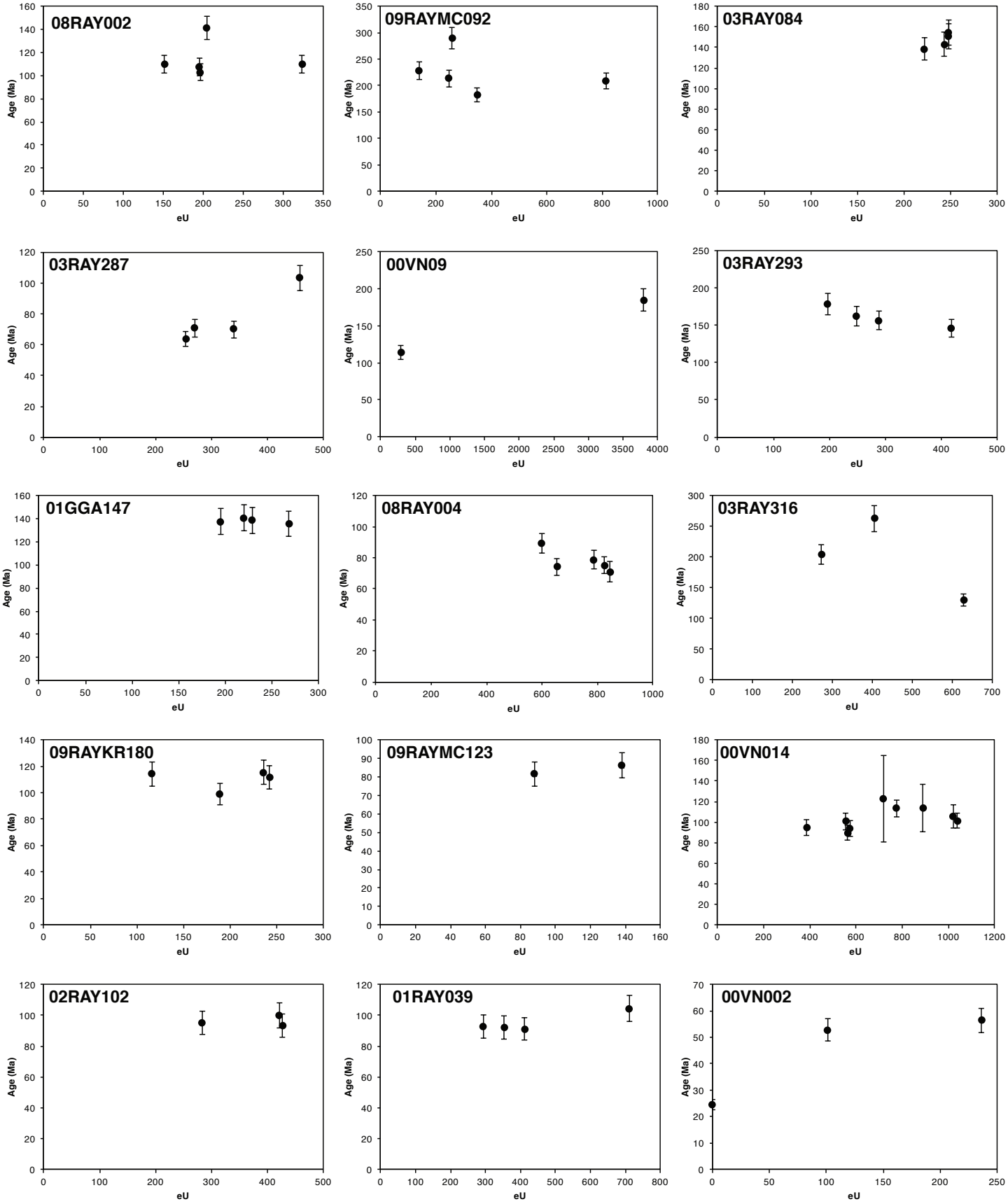

Figure A1. ZHe vs eU graphs for individual rock samples, YTT, Canada.

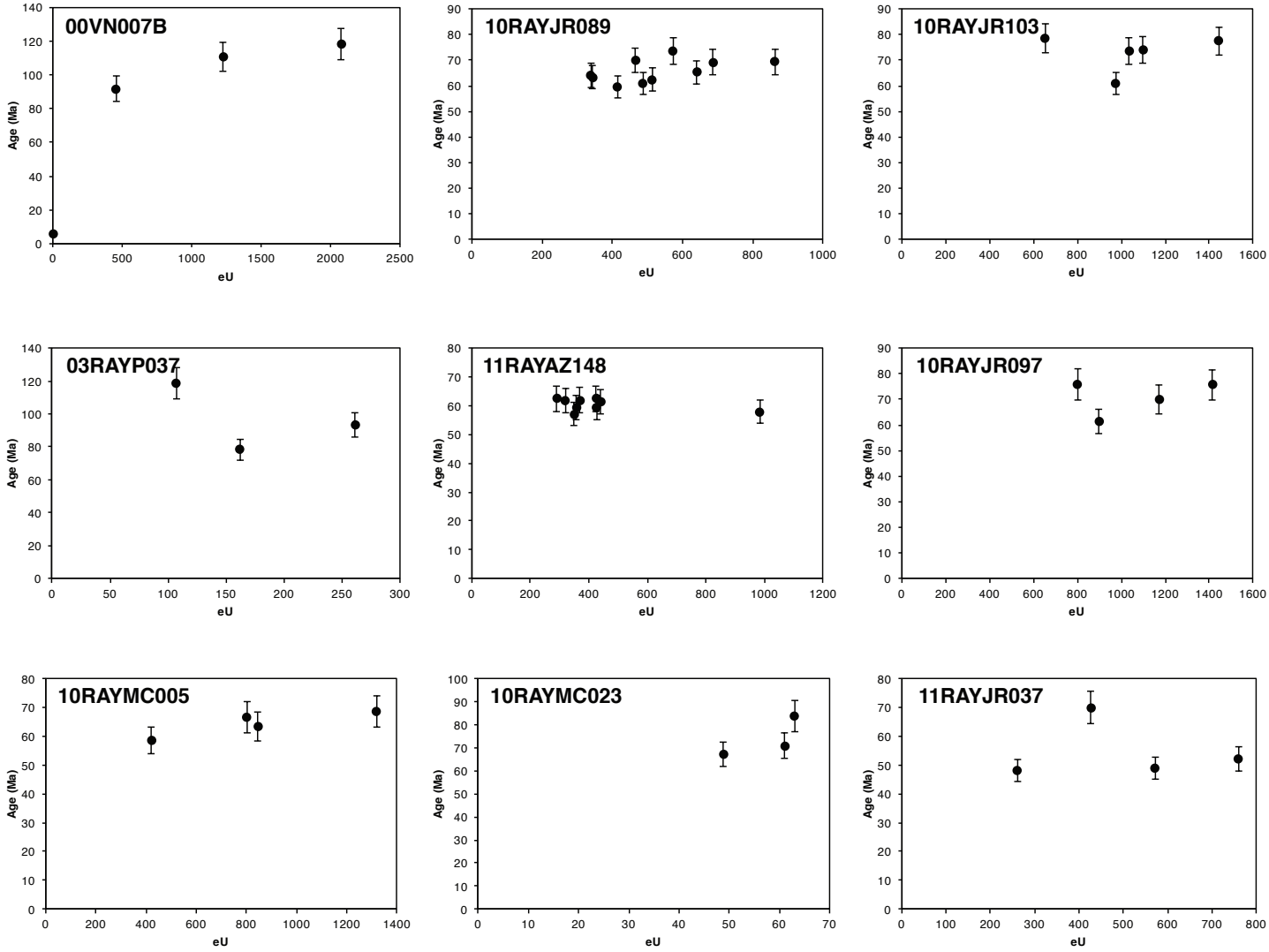

Figure A2. ZHe vs eU graphs for individual rock samples, YTT, Canada.

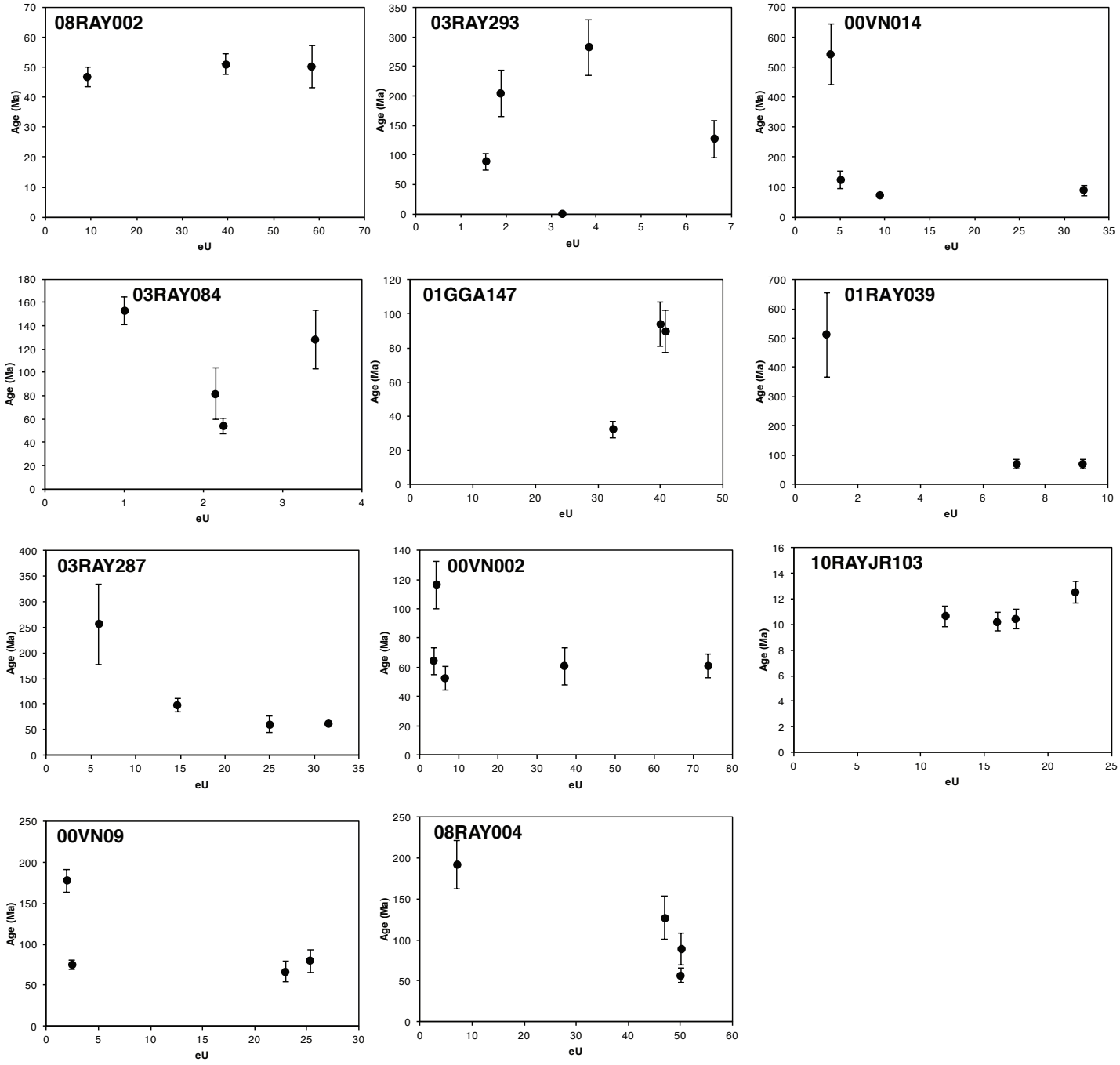

Figure A3. AHe vs eU graphs for individual rock samples, YTT, Canada.

References

Farley, K.A., Wolf, R., and Silver, L., 1996, The effects of long alpha-stopping distances on (U- Th)/He ages: Geochimica et Cosmochimica Acta, v. 60, p. 4223–4229, doi: 10.1016/S0016-7037(96)00193-7.

Farley, K.A., Rusmore, M.E., and Bogue, S.W, 2001, Post–10 Ma uplift and exhumation of the northern Coast Mountains, British Columbia: Geology, v. 29, p. 99–102, doi: 10.1130/0091-7613(2001)029<0099:PMUAEO>2.0.CO;2.

House, M.A, Farley, K.A., and Stockli, D.F., 2000, Helium chronometry of apatite and titanite using Nd-YAG laser heating: Earth and Planetary Science Letters, 183, p. 365–368, doi: 10.1016/S0012-821X(00)00286-7.

Reiners, P.W., 2002, (U-Th)/He chronometry experiences a renaissance: EOS Transactions American Geophysical Union, v. 83, p. 21–27, doi: 10.1029/2002EO000012.

Chapter 3.

Mapping Curie depth across western Canada from a wavelet analysis of magnetic anomaly data

Élyse Gaudreau, Pascal Audet, David Schneider

Abstract

In this study, we estimate Curie depths in western Canada, which provide geothermal gradient estimates for crustal rocks throughout the study area. The Curie depth corresponds to the point at which rocks reach the Curie temperature, above which the material is paramagnetic. Previous studies have shown that there is an abrupt change in crustal temperatures between the Canadian Cordillera and adjacent North American craton, making this an ideal study area to evaluate a new method of estimating Curie depths. We use a wavelet transform for the spatio-spectral analysis of magnetic anomaly data to map the depth to the bottom of the magnetized source rather than the oft-used moving windows, since wavelets allow a better compromise between spatial and wavenumber-domain resolution. We forego the common assumption that crustal magnetization has a high degree of randomness, since many studies have shown that this assumption results in depths to the base of the magnetized crust that are greatly overestimated. The parameters in our model therefore include the parameter β, which describes the degree of self-similarity of magnetization, z_t and z_b, the depths to the top and bottom of the magnetized crust, respectively. Synthetic tests reveal the increased accuracy of the estimated z_b when values for z_t are set prior to the inversion, consequently for western Canada, z_t is set to the thickness of meta-sedimentary rocks overlying the magnetic bedrock. However, in areas where there are rapid, high-amplitude

changes in z_t, the z_b values are underestimated. Moreover, in areas where the z_t values used in the inversion are underestimated, the z_b results are greatly overestimated, highlighting the importance of choosing appropriate input parameters. We estimate the value of β in various regions by comparing the statistics of predicted heat flow values obtained from Curie depths with those from measured heat flow data. In the Canadian Cordillera and the Slave craton, the β parameter that gives the most accurate results is 2.5. A β parameter of 2.0 gives the most accurate results for the remaining North American craton. The Curie depths resolve geological domains and important structural features, with estimates for z_b averaging 15 ± 1 km in the Cordillera, 32 ± 3 km in the Slave craton, and 34 ± 3 km in the North American craton to the south.

3.1. Introduction and tectonic setting

The western margin of the North American continent, which today consists of the Canadian Cordillera, is composed of a patchwork of allochthonous and para-autochthonous terranes that record almost 750 million years of tectonic processes (Monger & Price, 2002). The Cordillera started to develop in the Neoproterozoic with the formation of an ocean basin that formed on the margin of Laurentia, the newly-rifted portion of the Rodinia supercontinent that eventually became the North American continent. By 545 Ma, the rift had evolved to seafloor spreading, where the thick passive margin sediments presently found in the Western Canada Sedimentary Basin were deposited (Bond & Kominz, 1984; Monger & Price, 2002). From the middle Paleozoic, the divergent intra-plate setting shifted to a convergent setting, which led to a series of magmatic arcs forming the many oceanic and accretionary terranes that eventually accreted onto ancestral North America in the Mesozoic (Monger & Price,

2002, and references therein). Orogen-normal compression, uplift and crustal thickening in the Jurassic is interpreted as an important episode of Cordilleran mountain-building (Dusel-Bacon et al., 2002; Foster et al., 1985; Hansen & Dusel-Bacon, 1998; Monger & Price, 2002; Murphy et al., 2006). The Cretaceous is characterized by right-lateral transtension in the northern Canadian Cordillera, similar to the right-lateral transtension in the Eocene across the Canadian Cordillera (Gabrielse et al., 2006; Monger & Price, 2002). In the southern Canadian Cordillera, the subduction of the Juan de Fuca plate beneath North America was responsible for the accretion of Cenozoic terranes onto the western margin of the Cordillera in the Eocene (Cook, 1995).

The modern-day tectonics of the northern Canadian Cordillera are mainly governed by the oblique collision of the Yakutat block at the Alaska subduction zone, and the transpressional, right-lateral shear on the Queen Charlotte fault system offshore of the central Cordillera related to the northward motion of the Pacific plate (**Fig. 3.1**; e.g. Leonard et al., 2007; Mazzotti et al., 2003; Mazzotti et al., 2008). Modern deformation and seismic activity are therefore concentrated on the western margin of the northern Cordillera, however there is active deformation and seismicity in the Mackenzie Mountains, and the role of the active boundaries on the western Cordilleran margin as driving force for this deformation is highly debated (Finzel et al., 2014; Hyndman et al., 2005; Mazzotti et al., 2008; Mazzotti & Hyndman, 2002). Further south, the Juan de Fuca and Explorer plates are subducting beneath the southern Canadian Cordillera (Audet et al., 2008). The ongoing subduction is the main source of active deformation on the western margin of the southern Cordillera, along with some northeast-southwest contraction and shortening in the Rocky Mountains in eastern British Columbia (Mazzotti et al., 2008; Ristau et al., 2007).

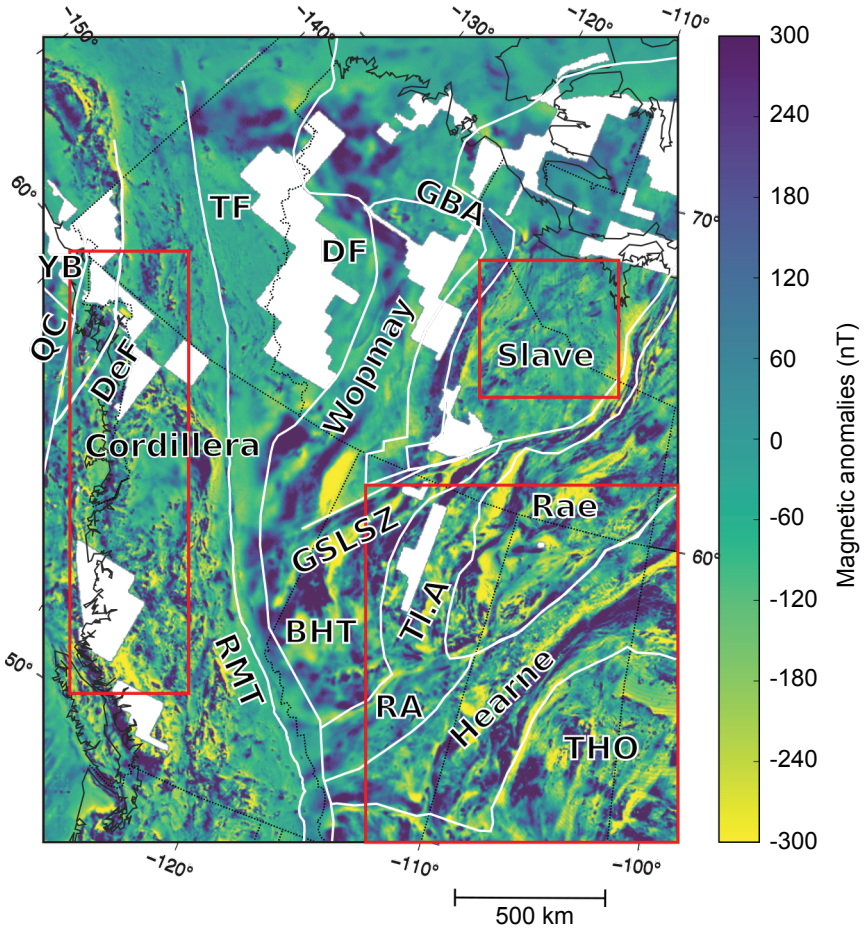

Figure 3.1. Magnetic anomaly grid of western Canada used in the inversion from NAMAG (2002). White lines represent important tectonic boundaries and physiographic lineaments: YB, Yakutat Block; QC, Queen Charlotte Fault; DeF, Denali fault; TF, Tintina Fault; GSLSZ, Great Slave Lake Shear Zone; the North American craton or Canadian Shield lies east of the Cordilleran Deformation Front (DF) and is composed of: GBA, Great Bear Arc; BHT, Buffalo Head Terrane; Tl.A, Talston Arc; RA, Rimbey Arc; THO, Trans-Hudson Orogen. Red boxes delineate the areas used when calculating zb averages for different regions.

Cutting across the entirety of the Cordillera is a major northwest/southeast-striking physiographic lineament which includes the Rocky Mountain Trench (RMT) in British Columbia and the Tintina Fault in Yukon and Alaska (**Fig. 3.1**). The crustal-scale, right-lateral Tintina Fault accommodated >400 km of displacement between the Cenozoic to the present day (Gabrielse et al., 2006; Hayward, 2015; Leonard et al., 2008; Roddick, 1967; Saltus, 2007). This marks an important boundary in terms of geology, separating the oceanic and accretionary terranes west of the fault from the deformed and weakly metamorphosed sedimentary rocks from ancestral North America's passive margin on the eastern side, up to the Cordilleran Deformation Front (e.g. Colpron et al., 2007; Gordey, 2013). East of the Deformation Front, an aggregation of multiple Archean cratons constitutes the North American craton, overlain by Proterozoic juvenile arcs and orogens to the west near the craton edge, overlapping to the other side of the Cordilleran Deformation Front (**Fig. 3.1**).

The present-day geophysical signature of the North American craton is also quite different than that of the Canadian Cordillera. Many studies have defined Cordilleran crust and lithosphere as relatively hot and thin compared to the North American craton, with the average heat flow in the Cordillera being roughly twice the average heat flow in the craton (Lewis et al., 2003; Mareschal et al., 1999; Rolandone et al., 2002), and the elastic thickness in the Cordillera rapidly increasing from <10 km to >70 km at the Cordillera-craton boundary (Audet et al., 2007; Flück et al., 2003). Mantle seismic velocities are lower beneath the Canadian Cordillera than beneath the adjacent craton, however at crustal depths to the uppermost mantle, the variations in seismic velocities vary according to important tectonic boundaries in the Cordillera (Bao et al., 2014; Hyndman et al., 2009; Kao et al., 2013; McLellan et al., 2018; Perry et al., 2002; Schaeffer & Lebedev, 2014). There is also an abrupt

transition between the 30 to 35 km thick crust in the Cordillera and 40 to 45 km thick crust in the craton (Clowes et al., 1995, 2005; Cook et al., 2012; Fernández-Viejo et al., 2005; Kao et al., 2013; Mooney et al., 1998; Perry et al., 2002; Tarayoun et al., 2017). The Moho depth is relatively uniform with a sharp interface in the Cordillera, however there are slight variations related to the Tintina Fault; observations from the SNorCLE lines show that the Moho depth is shallower at the Tintina Fault, increases southwest of the fault, and decreases further to the west (Clowes et al., 1995; Fernández-Viejo et al., 2005). In the North American craton, slight variations are also coincident with major tectonic boundaries (Clowes et al., 2005). Such a shallow Moho, despite the high elevations in the Canadian Cordillera, can be explained by the thermal expansion of the upper mantle, corroborated by high upper mantle temperatures inferred from the thin elastic thickness, low seismic velocities and high heat flow (Currie & Hyndman, 2006; Hyndman & Currie, 2011). The mechanisms responsible for generating and maintaining this high heat are not well constrained. Geodynamic models that focus on this problem require accurate estimates of crustal temperatures. In western Canada, heat flow measurements are sparse and unevenly distributed (**Fig. 3.2**; Mareschal, pers. comm., 2018).

Curie depth estimates, which correspond to the depth at which crustal rocks reach their Curie temperature (~580 °C for magnetite; Dunlop & Özdemir, 1997), give independent temperature constraints for geotherms over an entire area where aeromagnetic data is available. Curie temperature is defined as the temperature at which ferrimagnetic and ferromagnetic materials become paramagnetic. The thickness and depth to the base of the magnetized crust is reflected in the wavenumber content of the magnetic anomaly data, and the Curie depth can be estimated directly from the power spectra using curve-fitting methods. Therefore, this method provides more direct estimates of crustal temperatures than those

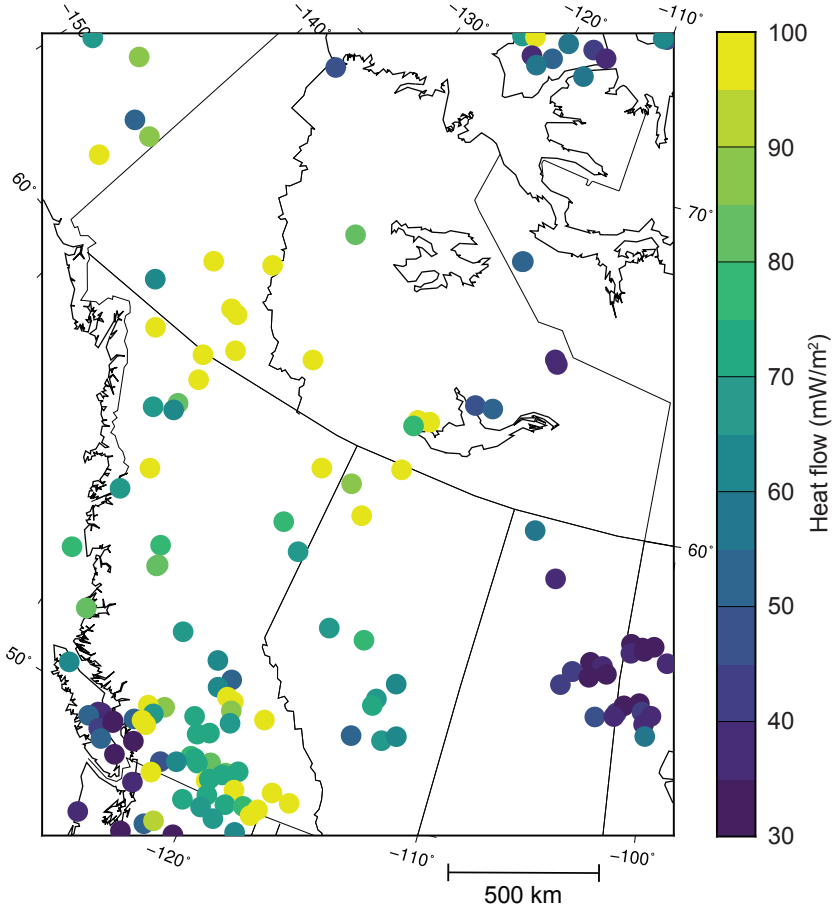

Figure 3.2. Distribution of heat flow measurements within the study area (Mareschal, personal communication, 2018).

obtained from elastic thickness or seismic tomography models (e.g. Goes & Van Der Lee, 2002; Priestley & McKenzie, 2006).

Since the wavenumber content of magnetic anomaly data varies spatially, and the long wavelength anomalies require large windows that reduce the spatial resolution, spatio-spectral localization techniques must be employed to analyze the signal. Among the most popular techniques used are moving square windows of various sizes to estimate the depth to the bottom of the magnetic source in different areas throughout the study region to create a map of the depth to the bottom of the magnetic source, or the Curie depth (e.g. Bouligand et al., 2009; Li et al., 2017; Wang & Li, 2015; Witter & Miller, 2017). The segmentation of the signal using moving windows has significant drawbacks including spectral leakage, even when minimized using tapers. Moreover, an optimal window size is set in advance, which must be large enough to accurately characterize the long wavelengths of the signal (typically a window width that is 6-10 times the depth to the bottom of the magnetic source; Ravat et al., 2007), limiting the spatial resolution. Here we use a 2D wavelet transform, where wavelets at different azimuths and scales are translated across the magnetic anomaly grid, avoiding the segmentation of the signal that arises when using moving windows. Wavelets with smaller scales result in better spatial resolution, and larger scales result in better wavenumber resolution. The wavelet transform offers a better compromise between spatial and wavenumber resolution than moving windows since the wavelet transform uses a combination of multiple wavelet scales to construct a power spectrum at each grid point. Moreover, using moving windows in western Canada is disadvantageous because there are significant data gaps (white areas in **Figure 3.1**), which require a buffer zone around each area that lacks magnetic anomaly data so that the windows do not overlap these areas. The wavelets in this study can

still translate across the anomaly grid even where there are data gaps, because these values are set to 0 nT, and the resulting wavelet coefficients are simply ignored.

The shape of the radially averaged power spectra that results from the wavelet transform in this study can be modelled as a function of the depths to the top (z_t) and bottom (z_b) of the magnetized layer, and β, which describes the fractal distribution of crustal magnetization (e.g. Bansal et al., 2011; Bouligand et al., 2009; Li et al., 2017; Maus et al., 1997; Maus & Dimri, 1996; Pilkington et al., 1994; Pilkington & Todoeschuck, 1993). Many Curie depth studies assume that the distribution of magnetization in the crust is random, which is represented by a β value of 0 (Blakely, 1988; Ross et al., 2006; Tanaka et al., 1999). Previous studies have demonstrated the inverse relationship between the fractal parameter and z_b results and show that assuming a randomly magnetized crust results in greatly overestimated z_b (e.g. Bouligand et al., 2009; Witter & Miller, 2017).

A great number of these studies (using both random and fractal magnetization) use the centroid method to estimate z_t and z_b (e.g. Bhattacharyya & Leu, 1977; Okubo et al., 1985; Tanaka et al., 1999). With this method, z_t is calculated by finding the slope of the power spectrum at high wavenumbers, and the centroid depth z_0 is calculated by finding the slope at low wavenumbers. The depth to the bottom of the magnetized crust (z_b) is given by $2z_0 - z_t$. However, there are no formal criteria on which part of the spectrum to use when calculating the high wavenumber and low wavenumber slopes for the centroid method.

In this study, we use a fractal correction method to remove the effect of the parameter β, followed by curve-fitting to find the best-fit theoretical power spectrum in a least-squares sense. We first test the inversion on synthetic data to show the strengths and limitations of the method. These tests demonstrate that z_b can be estimated at a better spatial resolution when

using the wavelet transform than when moving windows are used, and z_b can be more accurately estimated if z_t and β are fixed to the correct value. We then apply our method to data from western Canada. Our results indicate that the Tintina Fault system, RMT and Slave craton are very well resolved by the estimated z_b map. As expected, the z_b values suggest much higher geothermal gradients in the Canadian Cordillera than in the North American craton, and the z_b results are generally negatively correlated with surface heat flow measurements.

3.2. Methodology

3.2.1. Layered Magnetization Model

The magnetization model used here assumes that the magnetic anomalies are caused by a single magnetized layer confined between depths z_t and z_b. A magnetized layer of a certain depth and thickness has a predictable spectral shape, therefore the depths to the top and bottom of the magnetic source can be inferred from the power spectrum of the magnetic anomalies using curve-fitting methods. For a magnetic layer located between depths z_t and z_b, the equation from Blakely (1988) can represent the 2D theoretical power density spectrum of the total-field anomaly:

$$\Phi_h(k_x, k_y) = \Phi_M(k_x, k_y) \cdot H(k_x, k_y) \quad (1)$$

where $\Phi_M(k_x, k_y)$ is the 2D power spectrum of magnetization, and

$$H(k_x, k_y) = 4\pi^2 C_m^2 |\Theta_m|^2 |\Theta_f|^2 (e^{-|\boldsymbol{k}|z_t} - e^{-|\boldsymbol{k}|z_b})^2, \quad (2)$$

where $|\boldsymbol{k}|$ is the norm of the 2D wavevector $\boldsymbol{k} = (k_x, k_y)$, C_m is a constant, and Θ_m and Θ_f are complex functions of k_x and k_y that depend on the orientations of the dipole $\hat{m}$, and the unit vector parallel to the ambient field $\hat{f}$, respectively. The radial average of the total-field anomaly power spectrum is given by

$$\Phi_h(k) = A \cdot \Phi_M(k)(e^{-kz_t} - e^{-kz_b})^2 \quad (3)$$

where $k = |\boldsymbol{k}|$ and A is a constant that depends on the direction of magnetization and regional magnetic field.

Deep magnetic sources are characterized by longer wavelength anomalies, because the amplitude of short wavelength anomalies attenuate at a faster rate. Therefore, in the power spectrum, the relative power at low wavenumbers is higher when the base of the magnetized layer is deeper. The depth to the top of the magnetized layer affects the high wavenumber end of the spectrum, with higher power at shallower depths. Consequently, areas that are magnetized at shallow depths will be characterized by short wavelength anomalies.

3.2.2. Crustal Magnetization

Solving equation 3 for z_t and z_b from the observed spectrum of the total-field anomaly requires some assumptions on the statistical properties of magnetization. A common assumption is that crustal magnetization is a random distribution of dipoles in the Cartesian plane (e.g. Blakely, 1988; Ross et al., 2006; Tanaka et al., 1999; Witter & Miller, 2017), in which $\Phi_M(k)$ is a constant and we can solve directly for z_t and z_b from the total-field anomaly spectrum. However, magnetization often follows a fractal distribution, meaning that crustal magnetization has some degree of self-similarity (Maus & Dimri, 1995, 1996; Pilkington et al., 1994; Pilkington & Todoeschuck, 1993). The degree of self-similarity seems to depend on

a number of factors including the lithology and geological processes and is likely to vary within a study area (Bansal et al., 2010; Gettings, 2005, 2012; Leonardi & Kumpel, 1996; Maus & Dimri, 1995, 1996; Pilkington & Todoeschuck, 1993; Pilkington, 2007). Since z_b is estimated by analyzing the shape of the power spectrum of magnetic anomalies (e.g. Spector & Grant, 1970), self-similarity is an important characteristic to consider: a fractal distribution is expressed by a negative slope in the power spectra of magnetic anomalies on a log-log plot affecting all wavenumbers, whereas a random distribution has a flat power spectrum. The negative slope of the power spectrum of magnetization on a log-log scale (the power-law exponent for the power spectrum) is given by β:

$$\Phi_M(k_x, k_y) \propto |\mathbf{k}|^{-\beta}. \quad (4)$$

The negative slope of the power spectrum decreases with increasing degree of randomness, and $\beta = 0$ represents a random function whose power spectrum is flat. A fractal model for Φ_M in equation 3 is introduced by substituting Φ_M by $k^{-\beta}$.

3.2.3. Wavelet Analysis

The 2D wavelet transform computes the convolution of a signal with different wavelets $\psi^{\theta}_{a,\mathrm{b}}$, which are scaled and rotated versions of the mother wavelet ψ, at scales a and azimuths θ (Foufoula-Georgiou & Kumar, 1994). The different scales and azimuths allow for the signal to be analyzed at different bandwidths and directions, and they are translated to analyze the signal at different locations (**b**):

$$\psi^{\theta}_{a,\mathrm{b}} = \frac{1}{a}\psi\left[\frac{1}{a}\mathbf{C}_{\theta}(\mathbf{r} - \mathbf{b})\right], \quad (5)$$

where **r** is the location on the 2D physical plane (r_x, r_y), and $\mathbf{C}_{\theta}$ is the rotation operator

$$\mathbf{C}_\theta(\mathbf{r}) = [r_x \cos(\theta) + r_y \sin(\theta) - r_x \sin(\theta) + r_y \cos(\theta)]\,, 0 \leq \theta \leq 2\pi.$$

The scaled, rotated and translated wavelets allow for the characterization of a non-stationary signal in spectral space.

The non-orthogonal continuous wavelet transform is used for this analysis, which is defined at arbitrary scales, and is less complicated to express analytically than its orthogonal counterpart. It is defined as

$$W_f(a, \theta, b) = \int_{R^2} f(\mathbf{r}) \psi^{\theta *}_{a,b}(\mathbf{r}) d^2\mathbf{r}, \quad (6)$$

where the asterisk denotes complex conjugation. The convolution in equation 6 is equivalent to a multiplication in the Fourier domain, which is much faster to perform than equation 6:

$$\widehat{W}_F(a, \theta, \mathbf{k}) = \mathcal{F}[f] \hat{\psi}^*_a\big(\mathbf{C}_\theta(\mathbf{k})\big), \quad (7)$$

where $\mathcal{F}[f]$ is the 2D Fourier transform of $f(\mathbf{r})$ and $\hat{\psi}^*_a\big(\mathbf{C}_\theta(\mathbf{k})\big)$ is the complex conjugate of the Fourier transform of $\psi^{\theta}_{a,b}(\mathbf{r})$.

The choice of the wavelet influences the spatial and wavenumber resolution. In this study, a 2D scaled and rotated Morlet wavelet is chosen, since it is a complex-valued wavelet. The 2D isotropic Morlet wavelet is a complex exponential modulated by a Gaussian function, and being a directional wavelet, allows for the detection of azimuthal information:

$$\psi(\mathbf{r}) = e^{-i\mathbf{k_0}\cdot\mathbf{r}} e^{-\frac{1}{2}|\mathbf{Ar}|^2}, \quad (8)$$

which satisfies the conditions for a wavelet, which are a) a zero mean to establish a wave-like behaviour, and b) compact support in physical and spectral spaces. The variable $\mathbf{k}_0$ is a wavevector that sets the spectral resolution and has to be set to a value higher than 5.336 to

satisfy the zero-mean condition, and **A** is the 2 x 2 anisotropic diagonal matrix, where the first and second elements are set to 1 to create an isotropic wavelet in this case (Antoine et al., 1993; 1996; Kumar, 1995).

The Morlet wavelet is defined in spectral space as

$$\hat{\psi}(\mathbf{k}) = e^{-\frac{1}{2}|\mathbf{k}-\mathbf{k_0}|^2}. \quad (9)$$

The wavelets are arranged in a 'fan' geometry, defined by the superposition of adjacent isotropic Morlet wavelets through azimuthal averaging. The fan wavelet is superior to many popular wavelets in terms of Fourier-based estimates, such as Derivative of Gaussian, Paul, Perrier, and Poisson (Kirby, 2005). The fan wavelet is defined as

$$\hat{\psi}_F(\mathbf{k}) = \frac{1}{N_\theta}\sum_{i=1}^{N_\theta} \hat{\psi}[\mathbf{C}_{\theta_i}(\mathbf{k})], \quad (10)$$

where $N_\theta = int(\frac{\Delta\theta}{\delta\theta})$, $\delta\theta = 2\sqrt{-2\ln(0.75)}\,/|\mathbf{k}_0|$ and $\Delta\theta$ is the azimuthal extent.

The fast Fourier Transform is employed when transforming between the space domain and spectral domain to decrease the processing time, using the magnetic anomaly grid padded with zeros to the next power of 2 in each direction. For a more in-depth description of the wavelet transform, see Foufoula-Georgiou & Kumar (1994), Torrence & Compo (1998), and Holschneider (1999).

3.2.4. Application

In this study, 2D wavelets are translated over the entire study area at 20 different scales, yielding multiple power spectra with different bandwidths at each grid point on the magnetic anomaly map. The 3σ uncertainty is then calculated for each power spectrum from the radial

averages. Equation 3 may be used as the theoretical expression for the power density spectrum once the fractal dimension is corrected for; the slope of the radially averaged power spectrum is removed by dividing it by $|\mathbf{k}|^{\beta}$. To simplify the analysis, the logarithm of the radial average of the power spectrum is calculated at each grid point, and only includes wavenumbers from 0.01 to 0.5 rad/km:

$$\ln\left(\Phi_h(k)\right) = \mathrm{B} + \ln\left(\Phi_M(k)\right) + 2 \cdot \ln(e^{-kz_t} - e^{-kz_b}) \quad (11)$$

The best-fit curve, and thus the best-fit z_t and z_b are then found using nonlinear least-squares, and the goodness of fit is calculated using the reduced chi-square statistic. Similar to this study, Bouligand et al. (2009) estimated z_t and z_b by finding the theoretical power spectrum that best fits the calculated power spectrum in a least-squares sense, however the fractal dimension of the calculated spectrum did not have to be corrected since the equation for the theoretical power spectra used was from Maus et al. (1997), which includes β. Bouligand et al. (2009) also used a 3D model for crustal magnetization whereas a 2D magnetization model is used here, so the β value of 3 used in Bouligand et al. (2009) is equivalent to a β value of 2 in this study. Bouligand et al. (2009) demonstrated that calculating z_t, z_b and β simultaneously may lead to inaccurate results, therefore in this study, we estimate depth parameters with β fixed at a constant value for the entire study area. Multiple maps of z_t and z_b created using a different β value from 2.0 to 3.5 are shown, but inversions were also carried out with β values from 1.5 to 4.0, which are typical values estimated in crustal rocks (e.g. Maus & Dimri, 1995; Maus et al. 1997; Pilkington & Todoeschuck, 1993).

3.3. Synthetic examples

The synthetic tests in the present study builds on the work of Bouligand et al. (2009) by testing the inversion when both β and z_t are fixed, which shows that z_b values are more accurate when it is the only unknown parameter. Moreover, we go further by testing the inversion on a magnetized layer that has a variable thickness, showing that varying z_t and z_b in the synthetic models results in less reliable z_t and z_b estimates than a uniform magnetic layer. We test the inversion by generating synthetic magnetic anomaly maps using a set of parameters that describe the magnetization: z_t, z_b and β. First, the Fourier spectrum of magnetization is generated by creating a grid of wavenumbers with random phase; the wavenumber grid is then raised to the exponent - $\beta/2$, and inverse Fourier transformed. To obtain the magnetic anomaly map, we multiply the Fourier transform of the magnetization by the function H in equation 2 using the specified values for z_t and z_b. In these examples, we only test the recovery of z_t and z_b assuming a known β parameter. The synthetic map is therefore corrected for β using the input value. We then calculate the wavelet transform and wavelet power spectra using the parameter $\mathbf{k}_0 = 10$, and invert each point of the 2D map using equation 11 to estimate z_t and z_b. This inversion is carried out 100 times using the same model parameters but a different random seed generator in order to obtain the statistics of the recovered parameters. For each model, the inversions are also run where z_t is set to the correct value, and z_b is the only parameter estimated.

Selected inversion results from the synthetic datasets are shown in **Figures 3.3, 3.4, 3.5, and 3.6. Figure 3.3** shows the inversion results for a magnetized slab with uniform z_t and z_b, and illustrates the trade-off between z_t and z_b. These examples show how setting z_t to the correct (i.e., input) value provides much more accurate z_b results.

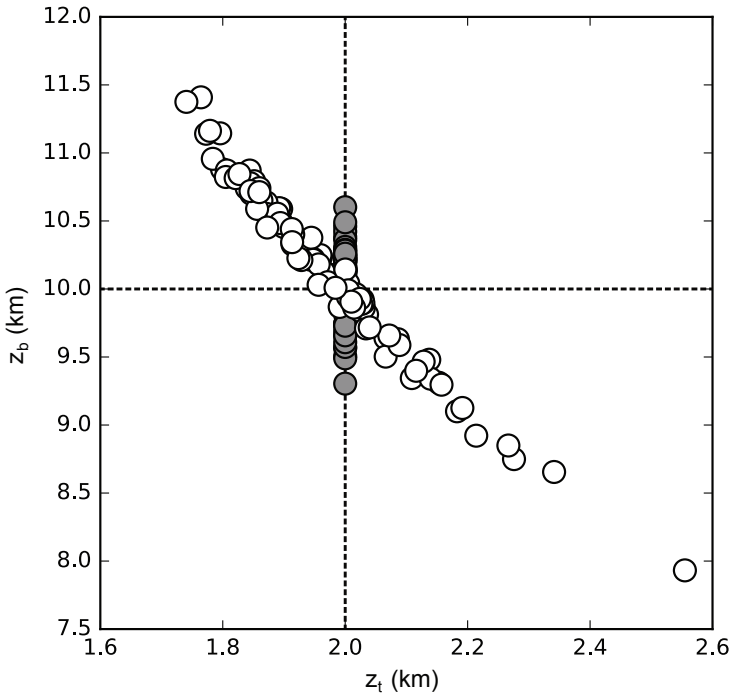

Figure 3.3. Results from 100 inversions on synthetic magnetic anomaly data generated for a magnetized layer of uniform thickness where $\beta = 3.0$, $z_t = 2$ km and $z_b = 10$ km, plotted as z_b as a function of z_t. There is a much larger spread in the results when z_t and z_b are jointly estimated (in white) rather than when z_b alone is estimated (in gray).

Synthetic data are also generated for a magnetic layer of variable thickness using the method of Blakely (1995), where the Fourier transform of the total-field anomaly is given by

$$\mathcal{F}[\Delta T] = 2\pi C_m \Theta_m \Theta_f e^{|k|z_0} \sum_{n=1}^{\infty} \frac{(-|k|)^n}{n!} \mathcal{F}[M(z_t^n - z_b^n)], \quad (12)$$

where $\mathcal{F}[\Delta T]$ is the Fourier transform of the total-field anomaly ΔT and $z_0 = \frac{z_t + z_b}{2}$.

Figure 3.4A and 3.4B shows the depth to the top and bottom of the magnetic layer, respectively, and **Figure 3.4C and 3.4D** shows the inversion results for a magnetic layer with a uniform z_t and variable z_b. The inversion results for z_b when z_t and z_b are jointly estimated have relatively large standard deviations and the estimated z_b are not accurate near the transitions from shallow to deep z_b (**Fig. 3.4C**). Where there is a transition from deep to shallow z_b, the average estimated z_b becomes even deeper instead of transitioning to a shallower z_b. As for the average z_t map (**Fig. 3.4C**), the average depth becomes shallower where the z_b becomes shallower. The z_t results are more accurate and have a smaller standard deviation than the results for z_b. When z_t is fixed to the correct value, z_b results are more accurate and the standard deviation is smaller relative to the results when z_t and z_b are estimated, however the inverted z_b are not able to replicate sharp transitions (**Fig. 3.4D**).

Figure 3.5 shows the inversion results when z_t varies, and the base of the layer is at a uniform depth. When z_t and z_b are estimated simultaneously, the correct topography in z_t is not found; z_t is relatively uniform but at the mean depth of the input z_t (**Fig. 3.5C**). The calculated z_b is also relatively uniform, but deeper than the input value (**Fig. 3.5C**). If z_b is calculated while z_t is fixed to the correct values, the estimated z_b are still not accurate, having the inverse of the z_t topography but with amplitudes ~2 times higher (**Fig. 3.5D**).

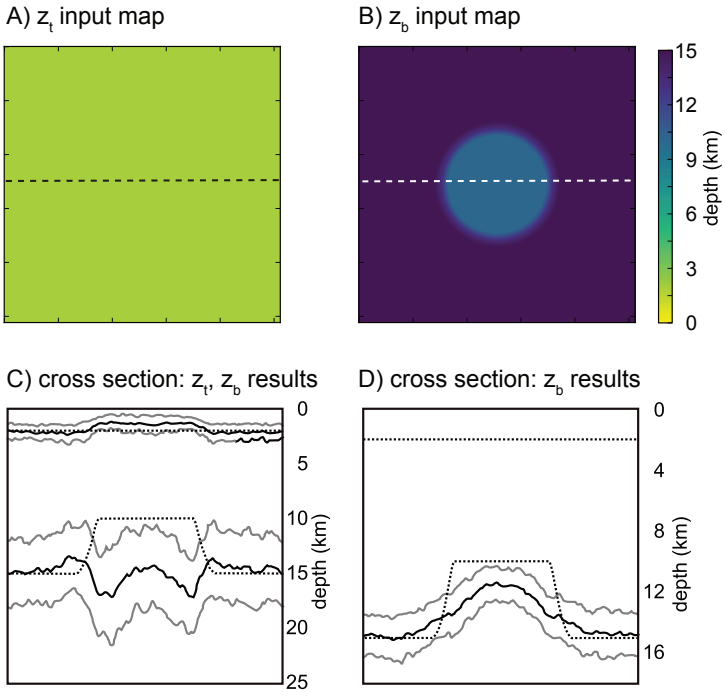

Figure 3.4. Results from 100 inversions of synthetic magnetic anomaly data generated for a magnetized layer where z_b is shallower in the centre of the map and $\beta = 3.0$; A, B) maps of the input parameters (z_t, z_b, respectively) used to generate 100 magnetic anomaly maps; C) cross section showing the depths to the top and bottom of the magnetized layer (dashed black lines) along the dashed lines in A) and B). The averaged depths retrieved for each of the parameters by the inversion where z_t and z_b are jointly estimated (solid black lines). Standard deviation is in gray. D) Cross section showing the depths to the top and bottom of the magnetized layer and the averaged depths to the bottom retrieved by the inversion where z_b alone is estimated.

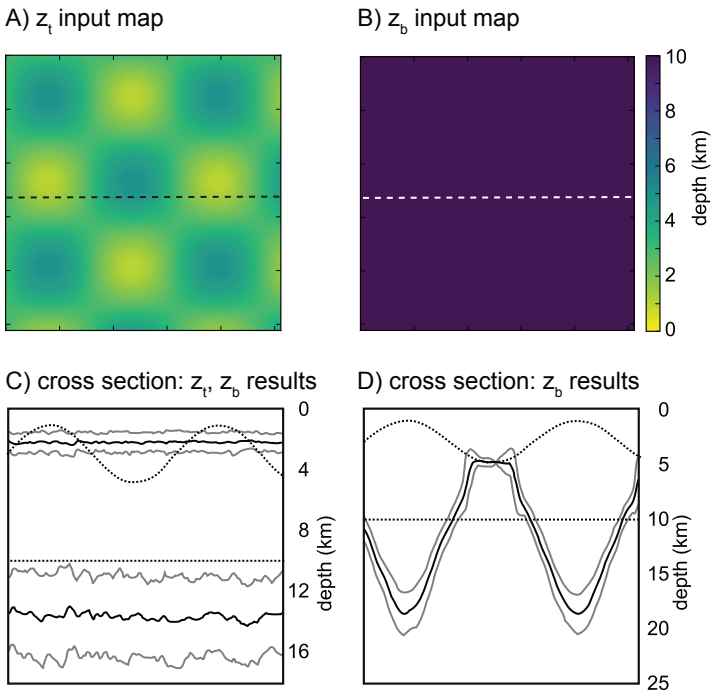

Figure 3.5. Results from 100 inversions on synthetic magnetic anomaly data generated for a magnetized layer where z_t varies strongly and z_b is constant, and $\beta = 3.0$. Formatting is the same as Figure 3.4.

Figure 3.6 shows inversion results where z_t strongly varies laterally, as expected for thick sedimentary basins that are only weakly magnetized. Here, z_t is fixed to the depth to basement according to SEDMAP (**Fig. 3.7**; Laske & Masters, 1997) and we further imposed a circular region in the centre where z_b is shallower (15 km) than the surrounding z_b (20 km) to assess if these variations can be recovered using the wavelet transform approach (**Fig. 3.6A, 3.6B**). The data gaps in the magnetic anomaly grid (white areas in **Figure 3.1**) are also included in this synthetic test, by setting the magnetic anomaly values in these areas to 0 nT to visualise the effect of these gaps on the inversion results. The inversion results are superior with z_t fixed to the correct depth during the inversion (**Fig. 3.6C, 3.6D**). In **Figures 3.6C and 3.6D**, where z_t is estimated and where z_t is fixed to the depth to the bedrock, respectively, the z_b near the edges of the maps are shallower than 20 km, then gradually increase within 200 km from the east and west edges, and 100 km from the north and south edges. The areas surrounding the data gaps are less accurate when z_t is estimated at the same time as z_b, where some of the surrounding z_b values are deeper than 36 km and extend less than 50 km outward (**Fig. 3.6D**). When z_b only is estimated, the z_b surrounding the data gaps are either shallower or deeper but less so than when z_t and z_b are estimated jointly, and again, these areas extend less than 50 km outward from the gaps (**Fig. 3.6C**). In either inversion, the z_b results are less accurate where there is a sharp transition in z_t, for example in the Bowser Basin in northern British Columbia, and at the Cordilleran Deformation Front (**Fig. 3.6C, 3.6D**).

3.4. Application to Western Canada

3.4.1. Magnetic Anomaly Dataset

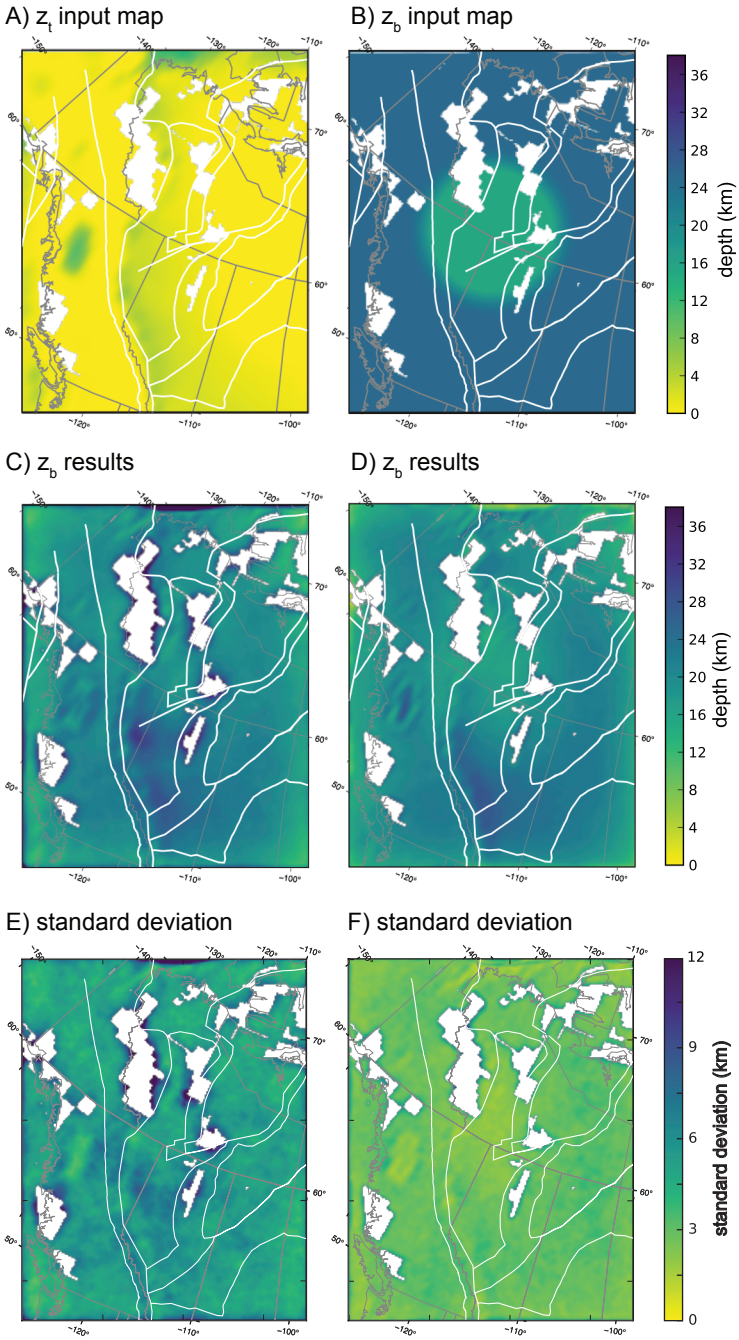

Figure 3.6. Results from 100 inversions on synthetic magnetic anomaly data generated for a magnetized layer where z_t is set to the thickness of sedimentary material in western Canada, and the z_b is shallower in the centre of the map. $\beta = 3.0$ and $k_0 = 10.0$. White areas are the data gaps in Figure 1. A, B) maps of the input parameters (z_t, z_b, respectively) used to generate 100 magnetic anomaly maps; C) map showing the depth to the bottom of the magnetized layer retrieved by the inversion (average of 100 inversions) where z_t and z_b are jointly estimated. D) map showing the depth to the bottom of the magnetized layer retrieved by the inversion (average of 100 inversions) where z_b alone is estimated. E) map showing the standard deviation of the 100 inversions where z_t and z_b are jointly estimated. F) map showing the standard deviation of the 100 inversions where z_b alone is estimated.

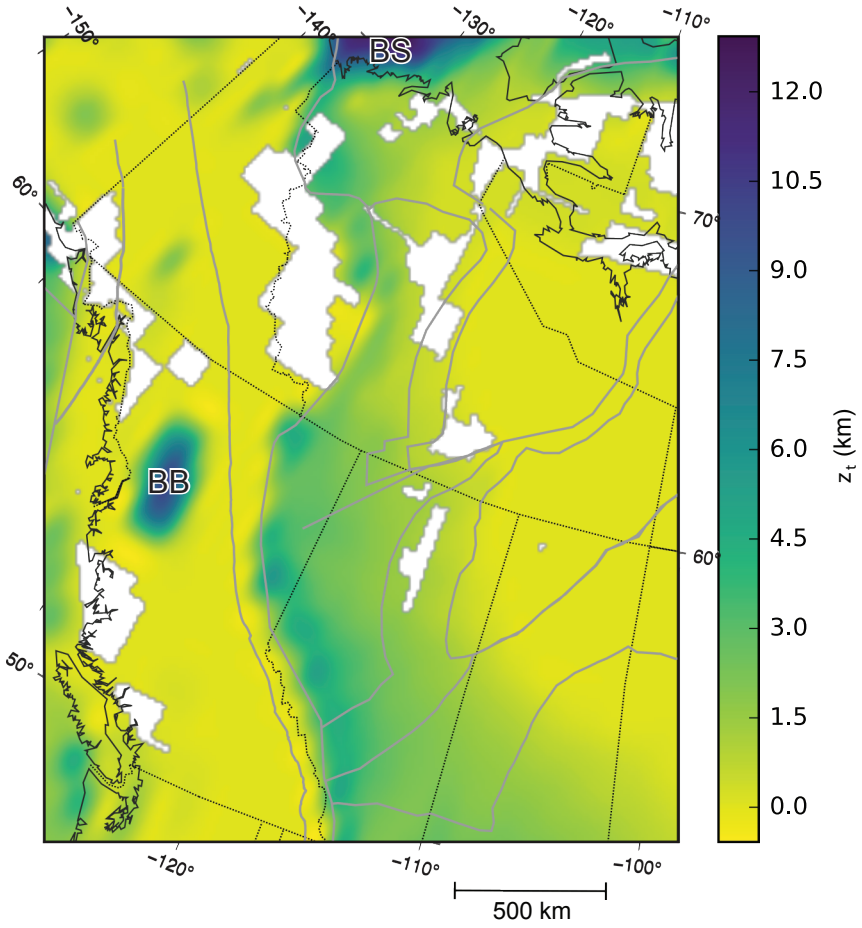

Figure 3.7. Map of thickness of sedimentary material used as z_t in the inversion, taken from SEDMAP (Laske & Masters, 1997). BB, Bowser Basin; BS, Beaufort Sea.

The magnetic anomaly map (**Fig. 3.1**) is a portion of the aeromagnetic compilation from NAMAG (2002), which includes surveys from different sources such as the Geological Survey of Canada and industry. For this study, the grid spacing is 3 km, and the grids are continued to an elevation of 305 m above topography. Merging different grids with different specifications may have resulted in offsets or changes in the spectral content within the survey area, thus the long wavelength anomalies in the original merged dataset are not accurately represented. The anomalies with wavelengths greater than 500 km are already filtered out of the compilation grid and replaced by downward-continued satellite data.

The change in spectral content of the magnetic anomalies throughout the study is visible from the magnetic anomaly map (**Fig. 3.1**). The Cordillera west of the Tintina-RMT boundary is characterized by short wavelength anomalies, and east of this boundary until the Cordilleran Deformation Front there are little to no magnetic anomalies even though the deformed Cordilleran crust continues eastward to the Deformation Front, which reflects a change in geology (**Fig. 3.1**). West of the Tintina-RMT boundary are a collection of accreted oceanic and arc terranes, and east of this boundary are the passive margin rocks of ancestral North America (e.g. Colpron et al., 2007; Gordey, 2013). The lack of magnetic anomalies east of the Tintina-RMT structure may be explained by the thick sedimentary material in these areas. Arc material is often relatively highly magnetic and sedimentary rocks are expected to be paramagnetic (weakly magnetic). East of the Cordillera Deformation Front, the long wavelength anomalies generally have much greater amplitude than the anomalies in the Cordillera (**Fig. 3.1**).

3.4.2. Curie Depth

The results presented in this section are shown as z_b maps for western Canada estimated from the wavelet analysis of magnetic anomalies, as described above. The results are shown as maps of the depths to the bottom of the magnetic layer relative to topography, which give an independent constraint for crustal temperatures. For joint inversions of z_t and z_b, the z_t map is also shown; otherwise the z_t is fixed to the depths to the magnetic basement shown in **Figure 3.7**.

The synthetic tests outlined above have shown that estimating z_t and z_b simultaneously leads to results that are less accurate. An inversion is done by jointly estimating z_t and z_b, to compare with the z_b results when z_t is fixed to a certain depth. An example is shown in **Figure 3.8**. In this inversion, β is set to 2.5. The saturation of the scalebar at 50 km is based on the assumption that the mantle is nonmagnetic (e.g. Wasilewski et al., 1979; Wasilewski & Mayhew, 1992), therefore Curie depths beyond this are deemed unreasonable (the maximum depth to the Moho in western Canada is ~50 km; Cook et al., 2012; Kao et al., 2013). Some of the z_b values in the northern Canadian Cordillera are >50 km, including some reaching over 1000 km. The mean z_b in the Cordillera is calculated from within the western box outlined in **Figure 3.1** to avoid the areas with unreasonably deep z_b values beyond 50 km. The z_b values in the Cordillera in **Figure 3.8** are 24 ± 4 km on average. In the Slave craton, taken from the top right box in **Figure 3.1**, the mean z_b is 29 ± 5 km and 14 ± 4 km in the rest of the North American craton.

In the following inversions, β and z_t are fixed to limit the number of unknown variables, leaving only z_b to be estimated. The depth to the top of the magnetic layer is chosen to be the thickness of the sedimentary layer overlying the bedrock (SEDMAP; Laske & Masters, 1997), since this layer is most likely weakly magnetic and is assumed to not contribute to the

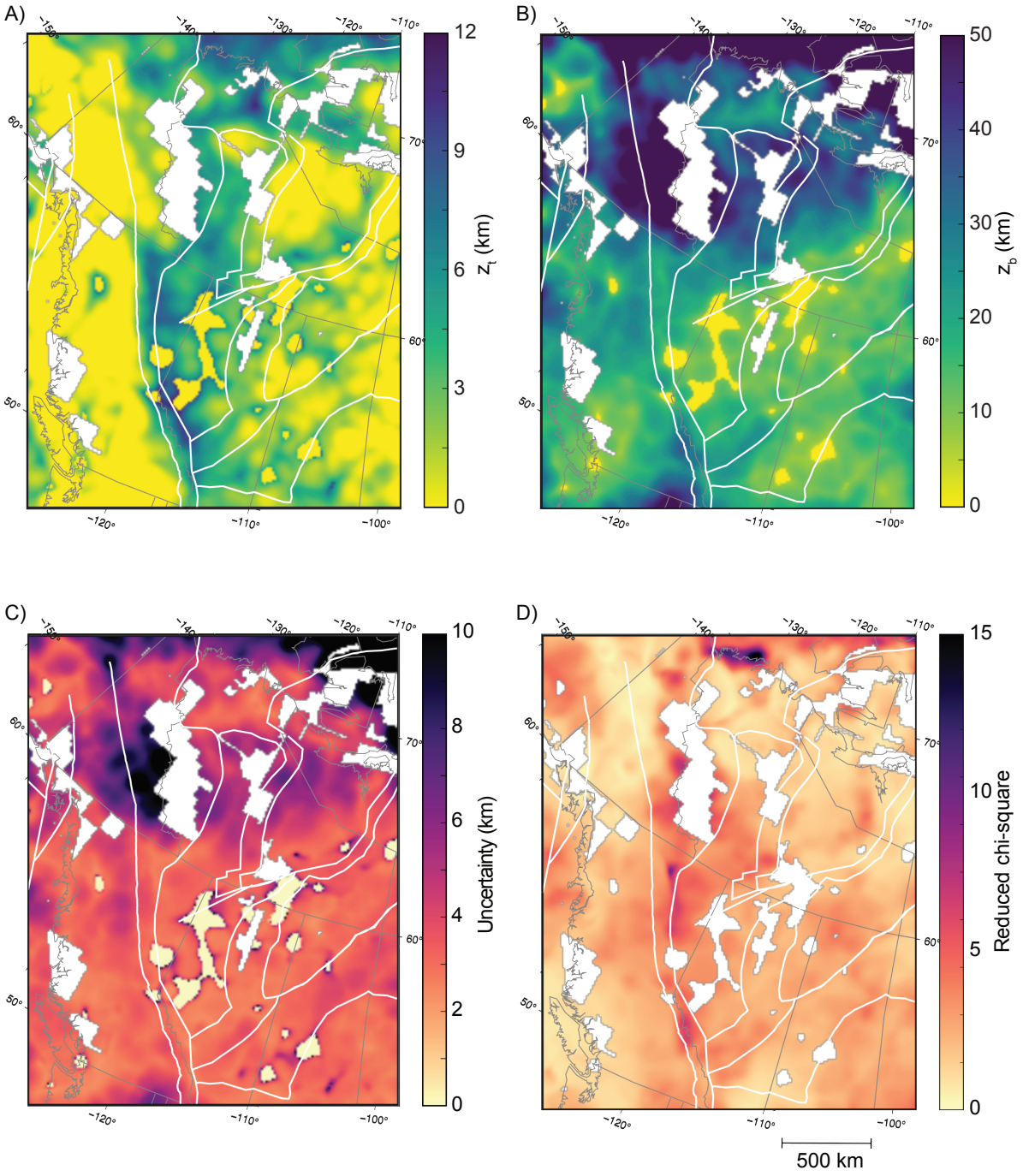

Figure 3.8. Maps with A) z_t and B) z_b results for western Canada when z_t and z_b are jointly estimated. C) Uncertainty in z_b. D) Reduced chi-square statistic for z_b. For this example, β = 2.5 and k_0 = 20.0.

magnetic anomalies. However, this map has limitations, for instance, the seismic model used does not resolve older, denser, and deformed sedimentary rocks such as the late Proterozoic to Devonian Selwyn Basin and Mackenzie Platform in Yukon (Gordey, 2013, and references therein).

Since the fractal parameter of magnetization for the crust in western Canada is not known, the inversion is performed multiple times with different values for β, ranging from 2.0 to 3.5. **Figure 3.9** shows the inversion results for different $\mathbf{k}_0$ and β values: when β increases, there is an important decrease in z_b (**Fig. 3.9**). Increasing the wavelet parameter $\mathbf{k}_0$ has a smoothing effect on the results since wavelets with higher $\mathbf{k}_0$ values are wider in space, so more accurate in the Fourier domain than the space domain (**Fig. 3.9**). With a higher $\mathbf{k}_0$, the short wavelength patterns in the z_b maps are less affected by the short wavelength patterns of the magnetic anomalies (**Figs. 3.1, 3.9**). As the β parameter increases from 2.0 to 3.5, the mean z_b value in the Cordillera decreases from 37.6 km to 1.7 km. The mean z_b within the Slave Craton ranges from 5.1 km to 75.8 km (with decreasing β), and in the Canadian Shield south of the Slave craton, the mean z_b ranges from 2.6 km to 34.2 km. These mean values are calculated from the maps obtained with a $\mathbf{k}_0$ value of 20. Since changes in z_t are very rapid in certain areas mentioned previously, the depth to the bottom of the magnetic source in the areas is underestimated, often with $z_b = 0$, so these data points are not included when calculating the averages. The edge effects illustrated in **Figure 3.6.D** do not change the mean z_b, namely in the craton south of the Slave Craton.

Maps with the uncertainty and reduced chi-square of the fitted parameters are shown in **Figures 3.10A and 3.10B**, respectively, for each of the inversions with a $\mathbf{k}_0$ of 20. Within each map in **Figure 3.10A**, the estimated z_b uncertainty is high where the z_b values are deeper

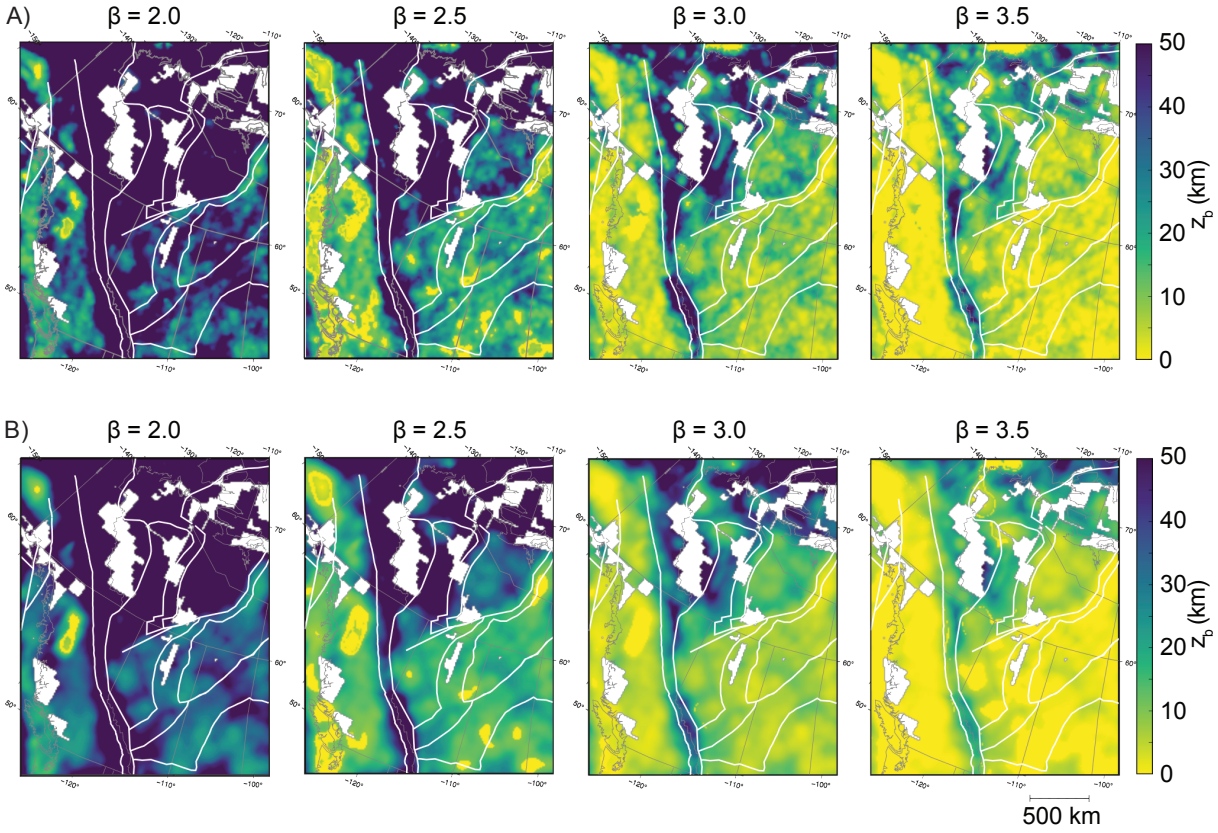

Figure 3.9. Maps showing z_b results based on the aeromagnetic data in western Canada when z_t is set to the sediment thickness map (Fig. 3.7) for A) $k_0 = 10$ and B) $k_0 = 20$ and various β (assuming constant β values throughout the study area), illustrating the inverse relationship between the fractal exponent β and z_b.

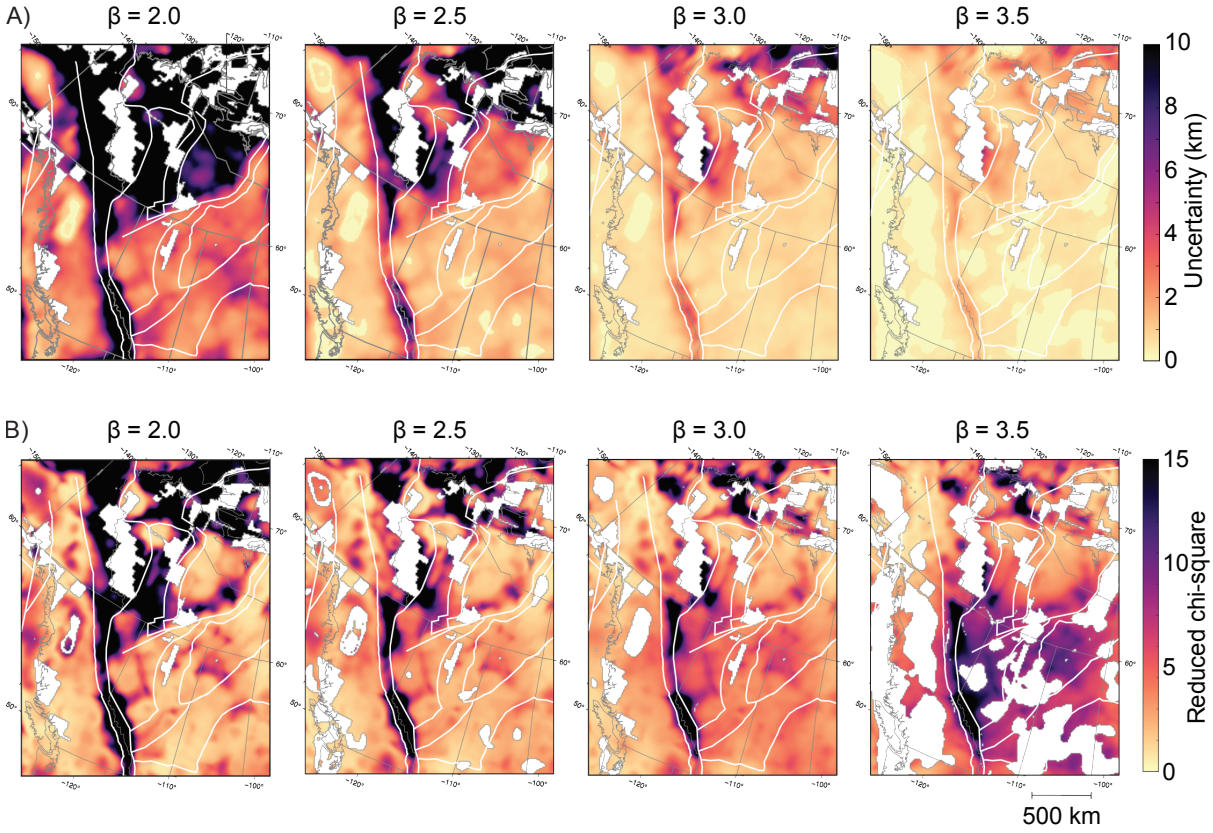

Figure 3.10. A) 3σ uncertainty of the best-fit z_b in western Canada for $k_0 = 20$. B) Maps of the reduced chi-square statistic illustrating the fit between the calculated and best-fit theoretical power spectra in western Canada for $k_0 = 20$. Goodness of fit is highest when the reduced chi-square is 1.

than 50 km, and decreases with increasing β. The chi-square statistic in the Cordillera and Slave craton remain relatively constant in the different inversions, but the chi-square statistic in the Canadian Shield south of the Slave craton decreases with increasing β (**Fig. 3.10B**). For all β values, the reduced chi-square is highest where z_b is deeper than 50 km. The fit in different areas is also illustrated in **Figure 3.11**, which shows the calculated and best-fit theoretical spectra from a single grid point in different areas when $\beta = 2.5$ and $\mathbf{k}_0 = 20$: the fit is superior in areas of shallow z_b. For the spectrum in **Figure 3.11A**, located in the southern Canadian Cordillera (grid point A in **Figure 3.11E**), z_t is set to 0.044 km and the best fit z_b is 13 ± 1 km, with a reduced chi-square of 1.7. The spectra in **Figures 3.11B and 3.11C** are from points located where the z_b results are aberrant. For grid point B, z_t is set to 0.028 km and the best fit z_b is 48 ± 5 km, with a reduced chi-square of 15. The fit for grid point C is worse; the best fit z_b is 82 ± 11 km, with a reduced chi-square of 20. Here, the z_t is set to 1.20 km. Grid point D is located within the North American craton where z_b values are well below 50 km (**Figure 3.11E**). At point D, z_t is set to 0.53 km and the best fit z_b is 15 ± 1 km, with a reduced chi-square of 2.1.

3.4.3. Monte Carlo Simulation

The previous section compares the results for the different z_b maps of western Canada resulting from inversions with different β parameters. In order to find the most appropriate β between 2.0 and 3.5 for different regions within the study area (assuming that β is constant within these regions), we assume that z_b within the boxes outlined in **Figure 3.1** correspond to the Curie depth and compare observed heat flow estimates (un-corrected for crustal heat generation) with heat flow calculated by assuming a conductive geotherm constrained by the average Curie depth within each box. The heat flow for the Slave craton is calculated

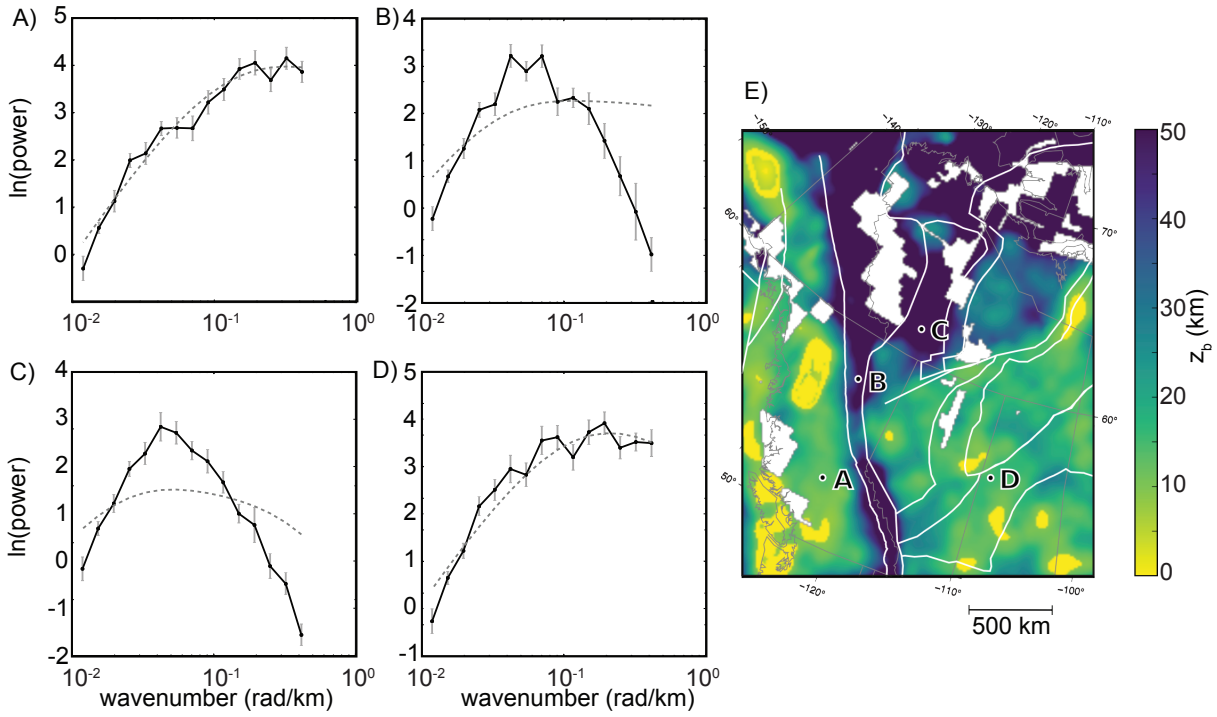

Figure 3.11. A-D) Calculated spectra (solid black line) and best-fit theoretical spectra (dashed gray line) for select grid points, with the locations shown in E) the z_b map of western Canada. Error bars (3σ confidence intervals) are in gray.

separately from the heat flow of the Canadian Shield to the south because of the distinct z_b results in the Slave craton, which may be due to a different β parameter.

A Monte Carlo approach is used in order to include a range of possibilities for the Curie temperature. We sample the Curie temperatures from a normal distribution with a mean of 580 °C and standard deviation of 50 °C (**Table 3.1**). The Monte Carlo simulation calculates 1,000,000 heat flow values from the equation

$$q = \kappa \frac{T_C}{z_b}, \kappa = \kappa_n \frac{\ln(1+c \cdot T_C)}{c \cdot T_C} \quad (13)$$

where q is the heat flux, κ is the bulk conductivity, κ_n is the thermal conductivity at 0 °C, T_C is the Curie temperature, and the temperature coefficient for the upper crust is c = 0.001 (Lewis et al., 2003).

A range of values centered around the average z_b for each region is also used. The parameters used for the Monte Carlo simulation are found in **Table 3.1**. The average measured surface heat flow is taken from Lewis et al. (2003) for the Cordillera (92 ± 24 mW/m^2) and the Slave craton (53 ± 10 mW/m^2; Lewis et al., 2003; Russell et al., 2001; Russell & Kopylova, 1999) and 50 ± 7 mW/m^2 is used for the North American craton south of the Slave craton (Majorowicz, 2018). **Figure 3.12** shows log-normal histograms indicating the frequency of the heat flow values obtained from each simulation, their mean and standard deviations, with measured surface heat flow values superimposed. For both the Cordillera and the Slave craton, the calculated mean heat flow is centred around the measured mean heat flow for β = 2.5 (**Fig. 3.12**). Using a β of 2.5, the average z_b is 15 ± 1 km in the Cordillera and 32 ± 3 km in the Slave craton (in the rectangular areas outlined in **Figure 3.1**). For the rest of the Canadian

Table 3.1. Parameters used in Monte Carlo simulation

	Mean Curie temperature (°C)[a]	Standard deviation (°C)[a]	k_n (W/m K)	z_b range (km)				Mean heat flow (mW/m^2)	Heat flow reference
				β = 2.0	β = 2.5	β = 3.0	β = 3.5		
Canadian Cordillera	580	50	2.7-3.3	27-47	9-21	2-8	0.5-3	94 ± 24	Lewis et al., 2003
Slave craton	580	50	2.7-3.3	60-90	26-38	11-16	3-7	53 ± 10	Lewis et al., 2003; Russell & Kopylova, 1999; Russell et al., 2001
North American craton	580	50	2.7-3.3	26-42	12-20	3-9	1-4	50 ± 7	Majorowicz, 2018

[a]For normal distribution

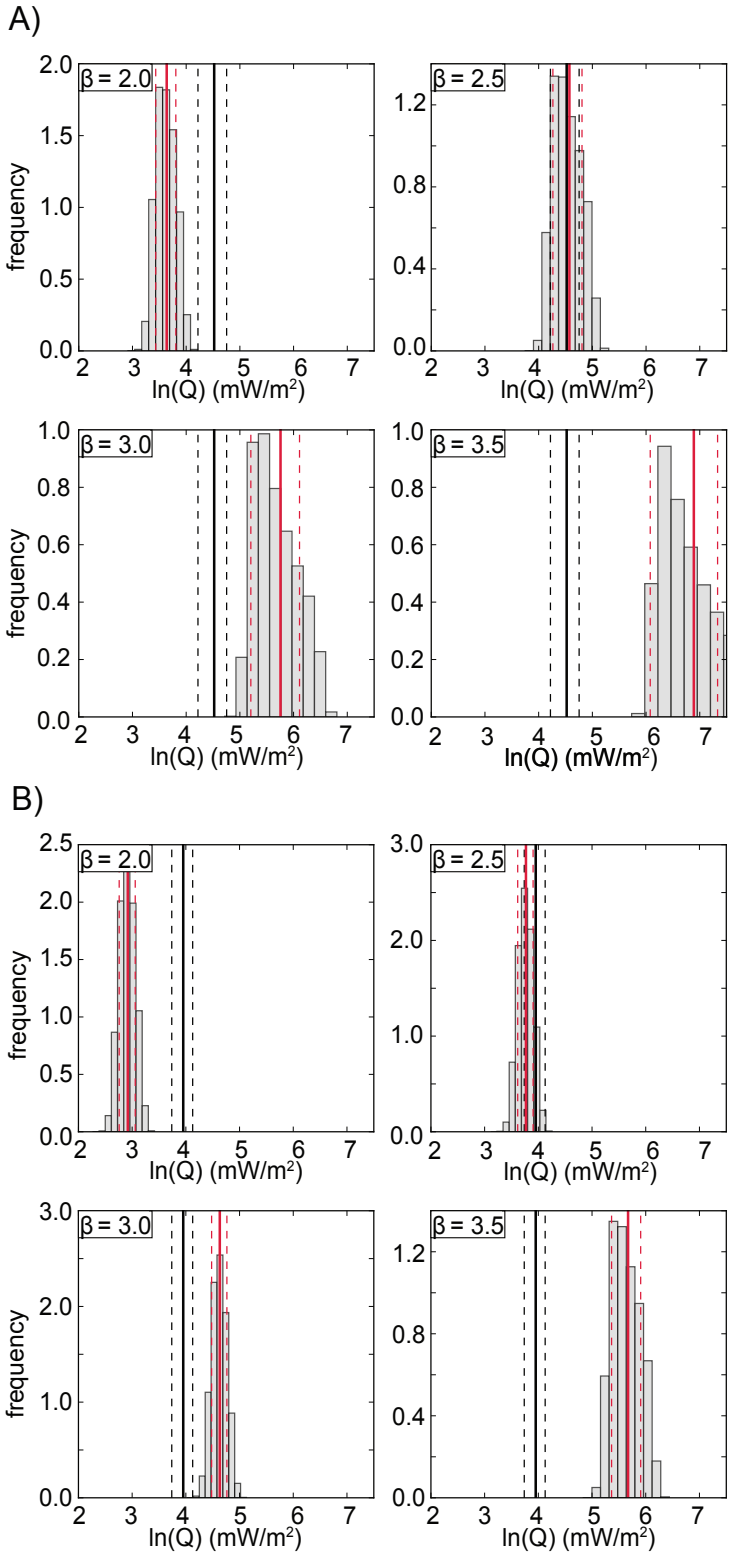

Figure 3.12. Monte Carlo simulation results for heat flow based on the inversion results with different β for A) the Canadian Cordillera, B) the Slave craton and C) the Canadian Shield south of the Slave craton.

C)

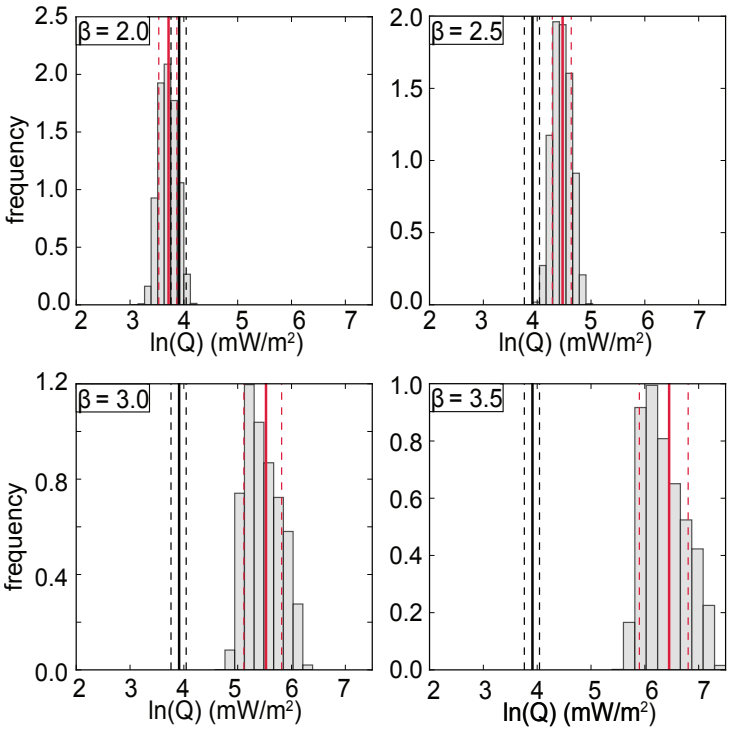

Shield, the calculated mean heat flow is closest to the measured mean heat flow if β = 2.0. The average z_b in this area is 34 ± 3 km if β = 2.0.

3.5. Discussion

3.5.1. Comparison with Geological and Magnetic Features

When z_t and z_b are estimated jointly, the only z_b feature that coincides with major tectonic or geological boundaries is the Slave craton, where z_b is deeper than the Canadian Shield to the south (**Fig. 3.9B**). For β = 2.5, the z_b depths in the Cordillera (23 ± 4 km on average; **Fig. 3.9B**) are deeper than the z_b results when z_t is fixed (15 ± 1 km on average; **Fig. 3.8**). In the Slave craton, the z_b is 29 ± 5 km when z_t and z_b are estimated jointly compared to 32 ± 3 km otherwise; and 14 ± 4 km in the rest of the North American craton when z_t is also estimated compared to 16 ± 1 km (**Fig. 3.9B**). When z_t is not fixed, the uncertainty is higher (**Fig. 3.9C**), however the reduced chi-square is lower than if z_b alone is estimated, with most values on the grid less than 5 (**Fig. 3.10; 3.9D**).

Based on the results of the Monte Carlo simulation, our preferred inversion results (where only z_b is estimated) for the Cordillera and Slave craton are those with a β of 2.5 while the preferred results in the rest of the Canadian Shield are the results with β = 2.0 (**Fig. 3.13**). The higher $\mathbf{k}_0$ is used in the preferred model, as it smooths the small-scale z_b features that tend to follow the short wavelength magnetic anomalies, and has a more accurate resolution in the wavenumber domain.

Perhaps the most striking feature of the z_b maps (**Fig. 3.13**) is the sharp transition between shallow (~15 km) and very deep (>50 km) z_b values which coincides with the Tintina

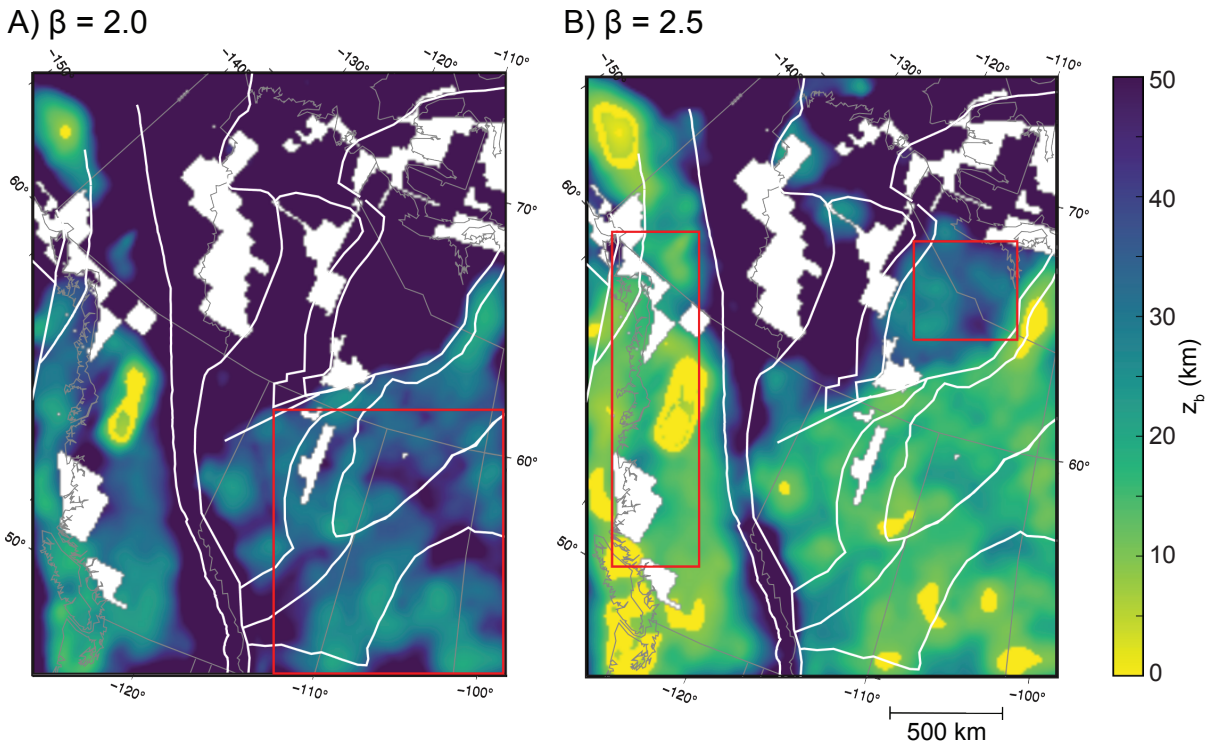

Figure 3.13. A) z_b map for western Canada where β = 2.0 and k_0 = 20.0, which are the best-fit z_b results for the Canadian Shield south of the Slave craton in terms of heat flow; B) Best-fit z_b results for the Canadian Cordillera and Slave craton in terms of heat flow, where β = 2.5 (based on the Monte Carlo heat flow simulation results).

Fault in Yukon and the RMT in British Columbia. In the northern Canadian Cordillera, the region of z_b beyond 50 km continues northward and eastward until the eastern edge of the Slave craton in the Northwest Territories. In the southern Canadian Cordillera, the area of deep z_b values extends eastward until the Cordilleran Deformation Front. In northern British Columbia, Alberta, and across the Northwest Territories, the Great Slave Lake Shear zone and Talston Arc are very visible in the magnetic anomaly map, and this is reflected in the z_b maps (**Figs. 3.1; 3.13**). These structures coincide with the southern and eastern extent of the Slave craton, which has distinct z_b values that are deeper than the rest of the Canadian Shield to the south: when β is set to 2.5, the average z_b in the Slave craton is 31.8 km, compared to 16.1 km in the rest of the Canadian Shield. If β is constant throughout the study area, the deeper z_b imply that the crust is much cooler than the average crust in the North American craton, however this does not reflect the heat flow data (Lewis et al., 2003; Majorowicz, 2018; Majorowicz & Weides, 2015; Rolandone et al., 2002). Alternatively, one could interpret the shallow z_b in the Canadian Shield south of the Slave craton as a lithological contact that represents the base of the magnetized crust that is shallower than the Curie depth (Blakely, 1988); however, a contact at this depth that is consistent throughout the North American craton south of the Slave craton is unlikely. A more reasonable explanation is that there is a strong change in lithology and geological history resulting in a different β value for the Slave craton, and this is consistent with the heat flow simulations (**Fig. 3.12**).

Rayleigh and S-wave tomography, magnetotelluric and geochemical studies and seismic reflection profiles have demonstrated that the Tintina-RMT boundary is a crustal-scale structural feature that defines a major change in the geology (Abraham et al., 2001; Cook et al., 2004; Ledo et al., 2002; McLellan et al., 2018; Snyder et al., 2005), and this is also evident

from our inversion results. East of the Tintina-RMT structure but west of the Deformation Front, the z_b that are beyond 50 km are interpreted to be due to a lack of ferrimagnetic material (i.e. the base of the weakly magnetic sedimentary or metasedimentary rocks in this area is deeper than the Curie depth). The difference in the anomalies in these areas is not due to a change in survey specifications since the locations and shapes of the different surveys do not coincide with the areas of deep z_b, yet they do coincide with geological boundaries. Moreover, these z_b values are deeper than the Moho (Clowes et al., 1995, 2005; Cook et al., 2012; Fernández-Viejo et al., 2005; Kao et al., 2013; Mooney et al., 1998; Perry et al., 2002; Tarayoun et al., 2017), so interpreting these values as Curie depths implies that the mantle material in this area is magnetic. In the past, the mantle was generally considered nonmagnetic (e.g. Wasilewski et al., 1979; Wasilewski & Mayhew, 1992), meaning that the base of the magnetized layer could correspond to the Moho rather than the Curie depth, however recent studies (e.g., Ferré et al., 2014) make a strong case for the occurrence of a magnetized upper mantle in certain geological contexts. In our study, however, many z_b values are >100 km in these areas, which implies a geothermal gradient of less than 5.8 °C/km (if a Curie temperature of 580 °C is assumed), which is much lower than the current estimates for this area (Clowes et al., 2005; Lewis et al., 2003; Majorowicz, 2018). In addition, the fit of the z_b in these areas is much worse than in the areas where z_b <50 km (**Fig. 3.10B, 3.11**). Therefore, these aberrant z_b values are likely erroneous. The fit is particularly poor at high wavenumbers; in the spectra plotted in **Figure 3.11B and 3.11C**, the slope of the spectra calculated using the wavelet transform is very steep at high wavenumbers compared to the theoretical spectra in these areas. Because z_t affects the high wavenumber portion of the spectra, this suggests that the actual z_t in these areas are much deeper than the values in SEDMAP, which corroborates the

interpretation that the aberrant z_b values are in areas where there is very thick sedimentary material. The poor fit between the theoretical and calculated spectra are likely due to underestimated z_t values.

The model used in this study assumes that the magnetic anomalies are caused by a single magnetized layer in the subsurface, the bottom of which may correspond to the Curie depth. However, the geology of an area is most likely more complex and is composed of many layers of different magnetic susceptibilities, and the anomalies at the surface are the sum of the contributions from these layers. In some cases, z_b may not always represent the base of the magnetized crust, but the depth to the base of the first magnetic layer if this first layer has a high enough magnetic susceptibility to mask the magnetic signal of the other layers (Blakely, 1988). If this is the case in our study region, the calculated heat flow values are overestimated. This is a concern in the Cordillera west of the Tintina-RMT structure, where the accreted terranes are thought to have been thrust over the ancestral North American passive margin as a thin thrust sheet (Snyder et al., 2009). The layering of the accreted terranes over the passive margin sediments (which are expected to have a weaker magnetic susceptibility) could result in z_b values that correspond to the base of this thrust sheet rather than the Curie depth (Blakely, 1988). Results from reflection profiles from Lithoprobe SNORCLE lines suggest that the thin thrust sheet is less than 10 km thick at the Tintina Fault, and gradually thickens westward to about 35 km over a lateral distance of ~250 km (Snyder et al., 2009). Our z_b values west of the Tintina-RMT structure do not increase steadily westward to 35 km, suggesting that the z_b values do not represent the base of the accreted terranes, rather the Curie depth is shallower than the base of the terranes.

The synthetic tests show that z_b is not well resolved when there are strong variations in z_t (**Fig. 3.5, 3.6**). Most of the depths in the sediment thickness map are close to 1 km, however in some areas, the z_t sharply increases to values above 10 km. This results in z_b values that are shallower than z_t for example in the Bowser Basin in northeastern British Columbia and in the Beaufort Sea, as illustrated in **Figures 3.7 and 3.13**. The z_b values in these areas are an artifact of the inversion and cannot be interpreted as the Curie depth.

3.5.2. Comparison with Other Studies

Previous studies have demonstrated the inverse relationship between the fractal parameter and z_b results and show that assuming a randomly magnetized crust with $\beta = 0$ results in greatly overestimated z_b (e.g. Bouligand et al., 2009; Witter & Miller, 2017). It is very clear from **Figure 3.9** that increasing the β value has a significant effect on the inversion results. Moreover, many of these studies (using both random and fractal magnetization) use the centroid method to estimate z_t and z_b (e.g. Bhattacharyya & Leu, 1977; Okubo et al., 1985; Tanaka et al., 1999). However, this method is subjective since there is no agreement on which part of the spectrum to use when estimating the high wavenumber and low wavenumber slopes for the centroid method, which may lead to incorrect z_b results.

The study area of Witter & Miller (2017) is located within the limits of our study, so a comparison between the z_b results can be made. The Witter & Miller (2017) study illustrates some of the disadvantages of using moving windows, such as the need for a buffer zone around each area that lacks magnetic anomaly data. Unlike the model presented in this paper, in Witter & Miller (2017), the Tintina Fault is not a boundary for a major change in Curie depths. This may be due to the large windows used (200 km and 300 km squares), some of which cover areas on both sides of the Tintina Fault. The Curie depths calculated from these windows are

based on the wavenumber content of both sides of the fault, however the wavenumber content on the eastern side of the fault is very different than that on the western side. This change is observable from the spectra plotted on **Figure 3.11**, and from the magnetic anomaly map (**Fig. 3.1**). Since the wavelet transform has a better spatial resolution, the Tintina-RMT boundary is resolved in the z_b maps presented herein. Similar to the results presented in this paper, there are very deep (>50 km) z_b east of the Tintina Fault and in northwestern Yukon in the Witter & Miller (2017) model. There is a small area of shallow z_b on the eastern side of the Tintina Fault in central Yukon which may be explained by a piece of the Slide Mountain and Yukon Tanana terranes on the other side of the Tintina Fault (see e.g. Colpron et al., 2007). An area of shallow z_b appears exactly where this terrane is located (closer to the Yukon-British Columbia border) in the z_b maps presented in this paper, visible if the saturation depth shown on the maps is increased beyond 50 km. This is also observed in Li et al. (2017), a worldwide model for Curie depths; a map of this model in Yukon is included in Witter & Miller (2017). This piece of the accreted terranes is composed of similar material as the terranes on the western side of the Tintina Fault (e.g. Colpron et al., 2007). West of this fault, the z_b results from this study and Witter & Miller (2017) are qualitatively similar, with shallower depths in central Yukon and slightly deeper depths in northwest Yukon.

Bao et al. (2014) calculated the Curie depth (defined as the 585 °C isotherm in their study) of a southwest-northeast cross section through the southern Canadian Cordillera and a ~400 km portion of the North American craton east of the Deformation Front, based on a steady-state conductive geotherm model using the method of Russell & Kopylova (1999). This is a 2-layer model where the upper crust geotherm is higher than the lower crust because of increased heat generation. The 585 °C isotherm calculated in the Cordillera in Bao et al.

(2014) is relatively constant at ~20 km, and markedly increases to ~80 km at the Cordillera-craton boundary and decreases eastward to ~40 km, which are deeper than the average z_b in the Cordillera and North American craton calculated in the present study. The discrepancy may be caused by the assumptions in the steady-state conductive geotherm model, for instance the upper versus lower crustal heat generation. Alternatively, the shallower z_b found in the present study could mean that the Curie temperature is lower than 585 °C, or the β parameter is not set to the correct value (and should be somewhere between 2 and 2.5 for the Cordillera, and below 2 for the Canadian Shield south of the Slave craton according to **Figure 3.9**). However, even with a different β in the craton, there still would not be the steady eastward decrease in z_b on the eastern side of the Deformation Front (**Figure 3.9**).

3.5.3. Comparison with Heat Flow Measurements

The Monte Carlo simulation assumes that the Curie temperatures of the crustal rocks in western Canada follow a normal distribution around 580 °C, the Curie temperature of magnetite. This is because the origin of magnetic anomalies in crustal rocks is principally due to magnetite and titanomagnetite, however other ferrimagnetic minerals may contribute to the whole rock magnetic susceptibility such as hematite, pyrrhotite and other iron and nickel alloys in some cases (Blakely, 1995 and references therein). Thus the popular assumption that the Curie depth corresponds to a 580 °C isotherm, the Curie temperature of pure magnetite (Dunlop & Özdemir, 1997), may not be correct, since the Curie temperature of titanomagnetite is lower than 580 °C at atmospheric pressure, and decreases with increasing Ti content (Hunt et al., 1995), and the Curie temperatures for hematite and pyrrhotite are 675 – 695 °C (Chevallier, 1951; Guillaud, 1951; Smith & Fuller, 1967) and 310 – 325 °C (Dekkers, 1989), respectively. Moreover, Curie temperatures have been shown to increase with pressure

(Schult, 1970). Most crustal rock-forming minerals such as quartz and feldspars are weakly magnetic relative to magnetite and titanomagnetite (e.g. Brown & McEnroe, 2008; Hunt et al., 1995), so their whole-rock susceptibility is mainly due to a trace amount of the latter two minerals (Blakely, 1995 and references therein). If the distribution of Curie temperatures used in the Monte Carlo simulation does not accurately represent the distribution of Curie temperatures in western Canada, the heat flow results from the simulation are not accurate.

The distribution of heat flow measurements is shown in **Figure 3.2**. The heat flow measurements are relatively dense in southern British Columbia, where the heat flow does not appear to be constant in this area, with values ranging from ~60 mW/m^2 to ~100 mW/m^2. This range of values is consistent with the measurements reported for northern British Columbia (**Figure 3.2**). In southwestern British Columbia on Vancouver Island, multiple heat flow measurements near 30 mW/m^2 are anomalously low and do not agree with the z_b results. The low heat flow anomaly in southwestern British Columbia is due to the Juan de Fuca slab subducting beneath the Cordillera in this area, and z_b is shallow in this area. The heat flow in Yukon seems to be more consistent near 100 mW/m^2, but the only measurements are in the southeastern part of Yukon. The high heat flow in Yukon has been attributed to an increased heat generation in the upper crust resulting in higher measured surface heat flow (Lewis et al., 2003). However, the high surface heat flow values seem to be consistent with xenolith and seismic studies in Yukon (Francis et al., 2010; Shi et al., 1998), and the z_b estimates do not seem to be shallower in the northern Canadian Cordillera than the southern portion as a result of higher upper crust heat generation (**Fig. 3.9**). There is a dense group of measurements in east-central Saskatchewan and west-central Manitoba where the heat flow is consistently low at values below 50 mW/m^2 (**Fig. 3.2**). **Figure 3.2** shows that the heat flow in the Cordillera is

generally higher than in the Canadian Shield, however the sparse data make it difficult to see the smaller-scale variations in crustal temperature and assess how consistent these heat flow values are throughout the Cordillera and North American craton. The sparseness of the data makes it difficult to compare with the z_b map, but the correlation between the heat flow values and z_b is shown by the scatter plots in **Figure 3.14**. A negative correlation is expected, since shallow Curie depths imply high geothermal gradients and vice-versa. **Figure 3.14A** shows the correlation between heat flow and the corresponding z_b at the location of the heat flow measurement within the different boxes outlined in **Figure 3.1**, for inversion results with β = 2.5. **Figure 3.14B** is the same scatter plot, but the z_b results within the Canadian Shield south of the Slave craton are the inversion results with β = 2.0, since these z_b results work best with published heat flow averages. There is an unsurprisingly large amount of scatter in both Figures, owing to the variety of rock compositions, geological settings, and upper crustal heat generation. The heat generation in the upper crust is often higher than the lower crust because of a higher concentration of radioactive elements (e.g. Lewis et al., 2003). The results for the Cordillera consistently plot at low z_b <15 km, but exhibit a wide range in heat flow values, although these are >40 mW/m^2. The North American craton mostly plots at deeper z_b (especially in **Figure 3.14B**), and exhibits a wide range in heat flow values that are generally lower than the Canadian Cordillera. However, the amount of upper crustal heat generation is uncertain in most areas. If the measured heat flow is significantly higher as a result of the upper crustal heat generation, the Monte Carlo simulation results may be biased toward a higher β, where the z_b results are shallower. This may also explain some high heat flow values where z_b is large in **Figure 3.14**. The steady state geotherm model of Russell & Kopylova (1999) accounts for the increased heat production in the upper crust, is consistent with Moho

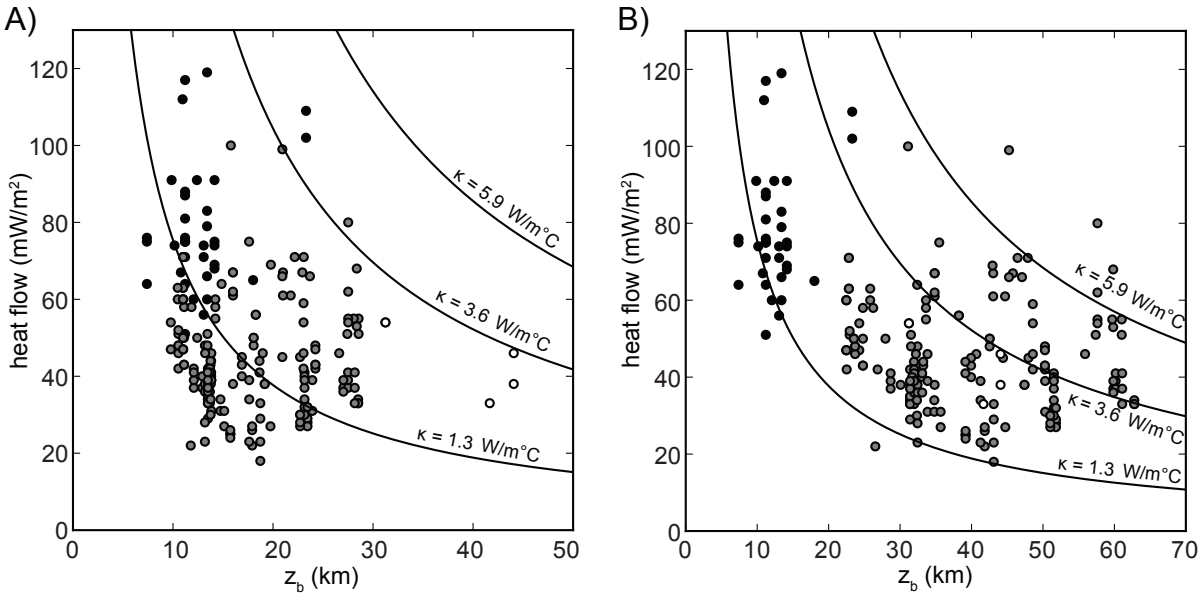

Figure 3.14. Heat flow as a function of zb in the different subregions delineated in Figure 2: Canadian Cordillera (in black); Slave craton (in white); North American craton south of the Slave craton (in gray). The curves plotted in each Figure are the theoretical curves for the 1D heat conductive model for different thermal conductivities: the heat flow is given by $q = \kappa T_C / z_b$ where κ is the thermal conductivity and T_C is the Curie temperature (580 °C is used here). A) z_b results when β = 2.5; B) z_b results where β = 2.5 for the Canadian Cordillera and Slave craton, and z_b results where β = 2.0 for the rest of the North American craton south of the Slave craton, after the results of the Monte Carlo heat flow simulation.

temperature estimates in the Slave craton (Lewis et al., 2003), and predicts the 580 °C isotherm to be at depths of ~75 km for the Slave craton, consistent with the inversion results using $\beta < 2.5$. The effect of the upper crustal heat generation on heat flow measurements is also highly variable within the study area since different rock types tend to have different concentrations of radioactive minerals, with felsic rocks having a greater concentration than mafic rocks (Hasterok & Chapman, 2011). Despite the variability in heat flow measurements, the negative correlation between heat flow and z_b is more apparent in **Figure 3.14B** than **3.14A**, where most of the data points fit between the theoretical curves for the 1D heat conductive transport model for thermal conductivities between 1.3 and 3.5 W/m°C.

3.6. Conclusions

This study improves on previous Curie depth studies, since the wavelet transform has a better spatial resolution than moving windows while still having a good wavenumber-domain resolution. Our method also assumes that crustal magnetization follows a fractal distribution characterized by the parameter β, since the results show the significant impact that this parameter has on the estimated z_b. The results provide crustal temperature constraints with good spatial coverage in western Canada, an area that is not well understood in terms of the source of heat to explain thermal isostasy in the Cordillera and the sharp contrast at the Cordillera-craton boundary. According to our heat flow calculations, a β value of 2.5 gives the most accurate inversion results in the Cordillera and Slave craton, while a β value of 2.0 gives better results in the Canadian Shield south of the Slave craton. With these parameters, the average Curie depth is 15 ± 1 km in the Canadian Cordillera, 32 ± 3 km in the Slave craton, and 34 ± 3 km in the North American craton to the south. The elevated and uniform

crustal temperatures in the Cordillera (west of the Tintina Fault) relative to the North American craton corroborate previous heat flow, seismic and elastic thickness studies, providing independent temperature information throughout most of the study area.

The present analysis has unearthed some of the limitations of this method. First, the inversions performed on synthetic datasets show that for a magnetic layer with variable thickness, the estimated z_b are not accurate if z_t is also estimated, and z_b estimates are greatly improved by setting z_t to the correct value in the inversion. Furthermore, the inversions on synthetic datasets have shown that if the map of fixed z_t values has areas of rapid changes with high amplitudes, the z_b results calculated in these areas are greatly underestimated. In the map of sedimentary rock thicknesses used as z_t in western Canada, this effect is seen in the Bowser Basin in northern British Columbia and in the Beaufort Sea where z_b is shallower than z_t, but elsewhere in the study area, there is a much smaller variation in sedimentary rock thicknesses that does not affect the z_b results as much. In other areas, the inversion resulted in unreasonably deep z_b in the northern part of the study area between the Tintina Fault and Slave craton, and in the southern part of the study area between the RMT and Deformation Front, since the base of the thick sedimentary rocks in these regions lies at depths greater than the Curie depth. Therefore, study areas with thick packages of nonmagnetic rocks and underestimating the z_t values used in the inversion might lead to large errors when estimating Curie depths.

The results presented in this study show that the thermal structure of different geologic domains may be estimated from a wavelet analysis of magnetic anomaly data, if using complementary datasets such as the depth to the magnetic bedrock, knowledge of the regional

geology, and the gravity and seismic structure of the crust and upper mantle to differentiate the Curie depths from the z_b that do not correspond to a thermal boundary.

References

Abraham, A. C., Francis, D., & Polvé, M. (2001). Recent alkaline basalts as probes of the lithospheric mantle roots of the northern Canadian Cordillera. *Chemical Geology*, *175*(3–4), 361–386. https://doi.org/10.1016/S0009-2541(00)00330-2

Antoine, J. P., Carrette, P., Murenzi, R., & Piette, B. (1993). Image analysis with two-dimensional continuous wavelet transform. *Signal processing*, *31*(3), 241-272. https://doi.org/10.1016/0165-1684(93)90085-O

Antoine, J. P., Vandergheynst, P., & Murenzi, R. (1996). Two-dimensional directional wavelets in image processing. *International journal of imaging systems and technology*, *7*(3), 152-165. https://doi.org/10.1002/(SICI)1098-1098(199623)7:3%3C152::AID-IMA1%3E3.0.CO;2-7

Audet, P., Jellinek, A. M., & Uno, H. (2007). Mechanical controls on the deformation of continents at convergent margins. *Earth and Planetary Science Letters*, *264*(1–2), 151–166. https://doi.org/10.1016/j.epsl.2007.09.024

Audet, P., Bostock, M. G., Mercier, J. P., & Cassidy, J. F. (2008). Morphology of the explorer - Juan de Fuca slab edge in northern Cascadia: Imaging plate capture at a ridge-trench-transform riple junction. *Geology*, *36*(11), 895–898. https://doi.org/10.1130/G25356A.1

Bansal, A. R., Gabriel, G., & Dimri, V. P. (2010). Power law distribution of susceptibility and density and its relation to seismic properties: An example from the German Continental Deep Drilling Program (KTB). *Journal of Applied Geophysics*, *72*(2), 123–128. https://doi.org/10.1016/j.jappgeo.2010.08.001

Bansal, A. R., Gabriel, G., Dimri, V. P., & Krawczyk, C. M. (2011). Estimation of depth to

the bottom of magnetic sources by a modified centroid method for fractal distribution of sources: An application to aeromagnetic data in Germany. *Geophysics*, *76*(3), L11–L22. https://doi.org/10.1190/1.3560017

Bao, X., Eaton, D. W., & Guest, B. (2014). Plateau uplift in western Canada caused by lithospheric delamination along a craton edge. *Nature Geoscience, 7*, 830–833. https://doi.org/10.1038/ngeo2270

Bhattacharyya, B. K., & Leu, L.-K. (1977). Spectral analysis of gravity and magnetic anomalies due to rectangular prismatic bodies. *Geophysics*, *42*(1), 41–50. https://doi.org/10.1190/1.1440712

Blakely, R. J. (1988). Curie temperature isotherm analysis and tectonic implications of aeromagnetic data from Nevada. *Journal of Geophysical Research*, *93*(B10), 11817–11832. https://doi.org/10.1029/JB093iB10p11817

Blakely, R. J. (1995). *Potential Theory in Gravity and Magnetic Applications*. Cambridge, U.K.: Cambridge University Press, 441 p.

Bond, G. C., & Kominz, M. A. (1984). Construction of tectonic subsidence curves for the early Paleozoic miogeocline, southern Canadian Rocky Mountains: Implications for subsidence mechanisms, age of breakup, and crustal thinning. *Geological Society of America Bulletin*, *95*(2), 155–173. https://doi.org/10.1130/0016-7606(1984)95<155:COTSCF>2.0.CO;2

Bouligand, C., Glen, J. M. G., & Blakely, R. J. (2009). Mapping Curie temperature depth in the western United States with a fractal model for crustal magnetization. *Journal of Geophysical Research: Solid Earth*, *114*(B11104). https://doi.org/10.1029/2009JB006494

Brown, L. L., & McEnroe, S. A. (2008). Magnetic properties of anorthosites: A forgotten source for planetary magnetic anomalies? *Geophysical Research Letters*, *35*(L02305). https://doi.org/10.1029/2007GL032522

Chevallier, R. (1951). Propriétés magnétiques de l'oxyde ferrique rhomboédrique (Fe2O3 α). *Journal de Physique et Le Radium*, *12*(3), 172–188.

Clowes, R. M., Zelt, C. A., Amor, J. R., & Ellis, R. M. (1995). Lithospheric structure in the southern Canadian Cordillera from a network of seismic refraction lines. *Canadian Journal of Earth Sciences*, *32*(10), 1485–1513. https://doi.org/10.1139/e95-122

Clowes, R. M., Hammer, P. T., Fernández-Viejo, G., & Welford, J. K. (2005). Lithospheric structure in northwestern Canada from Lithoprobe seismic refraction and related studies: a synthesis. *Canadian Journal of Earth Sciences*, *42*(6), 1277–1293. https://doi.org/10.1139/e04-069

Colpron, M., Nelson, J. L., & Murphy, D. C. (2007). Northern Cordilleran terranes and their interactions through time. *GSA Today, 17*(4/5), 4–10. https://doi.org/10.1130/GSAT01704-5A.1

Cook, F. A. (1995). Lithospheric processes and products in the southern Canadian Cordillera: a Lithoprobe perspective. *Canadian Journal of Earth Sciences*, *32*(10), 1803–1824. https://doi.org/10.1139/e95-139

Cook, F. A., Clowes, R. M., Snyder, D. B., van der Velden, A. J., Hall, K. W., Erdmer, P., & Evenchick, C. A. (2004). Precambrian crust beneath the Mesozoic northern Canadian Cordillera discovered by Lithoprobe seismic reflection profiling. *Tectonics*, *23*(2), TC2010. https://doi.org/10.1029/2002TC001412

Cook, F.A., Percival, J.A., & Clowes, R.M. (2012). Tectonic styles in Canada:

LITHOPROBE perspective on the evolution of the North American continent. In J.A. Percival, F.A. Cook, and R.M. Clowes (Eds.), *Tectonic Styles in Canada: The LITHOPROBE Perspective*: *Special Paper* (Vol. 49, pp. 467–498). St. John's, Canada: Geological Association of Canada.

Currie, C. A., & Hyndman, R. D. (2006). The thermal structure of subduction zone back arcs. *Journal of Geophysical Research: Solid Earth*, *111*(8), 1–22. https://doi.org/10.1029/2005JB004024

Dekkers, M. J. (1989). Magnetic properties of natural pyrrhotite. II. High- and low-temperature behaviour of Jrs and TRM as function of grain size. *Physics of the Earth and Planetary Interiors*, *57*(3–4), 266–283. https://doi.org/10.1016/0031-9201(89)90116-7

Dunlop, D.J., Özdemir, Ö. (1997). *Rock magnetism: fundamentals and frontiers*. Cambridge Studies in Magnetism. Cambridge, U.K.: Cambridge University Press.

Dusel-Bacon, C., Lanphere, M. A., Sharp, W. D., Layer, P. W., & Hansen, V. L. (2002). Mesozoic thermal history and timing of structural events for the Yukon-Tanana Upland, east-central Alaska : $^{40}Ar/^{39}Ar$ data from metamorphic and plutonic rocks, *Canadian Journal of Earth Sciences*, *39*(6), 1013–1051. https://doi.org/10.1139/E02-018

Fernández-Viejo, G., Clowes, R. M., & Welford, J. K. (2005). Constraints on the composition of the crust and uppermost mantle in northwestern Canada: *Vp*/*Vs* variations along Lithoprobe's SNorCLE transect. *Canadian Journal of Earth Sciences*, *42*(6), 1205–1222. https://doi.org/10.1139/e05-028

Ferré, E. C., Friedman, S. A., Martín-Hernández, F., Feinberg, J. M., Till, J. L., Ionov, D.

A., & Conder, J. A. (2014). Eight good reasons why the uppermost mantle could be magnetic. *Tectonophysics*, *624–625*, 3–14. https://doi.org/10.1016/j.tecto.2014.01.004

Finzel, E. S., Flesch, L. M., & Ridgway, K. D. (2014). Present-day geodynamics of the northern North American Cordillera. *Earth and Planetary Science Letters*, *404*, 111–123. https://doi.org/10.1016/j.epsl.2014.07.024

Flück, P., Hyndman, R., & Lowe, C. (2003). Effective elastic thickness T_e of the lithosphere in western Canada. *Journal of Geophysical Research*, *108*(B9), 2430. https://doi.org/10.1029/2002JB002201

Foufoula-Georgiou, E., & Kumar, P. (1994). Wavelet analysis in geophysics: an introduction. In *Wavelet Analysis and Its Applications* (Vol. 4, pp. 1–43). San Diego, U.S.A.: Academic Press.

Foster, H. L., Cushing, G. W., Keith, T. E. C., & Laird, J. (1985). Early Mesozoic tectonic history of the boundary area, east-central Alaska, *Geophysical Research Letters*, *12*(9), 553–556. https://doi.org/10.1029/GL012i009p00553

Francis, D., Minarik, W., Proenza, Y., & Shi, L. (2010). An overview of the Canadian Cordilleran lithospheric mantle. *Canadian Journal of Earth Sciences*, *47*(4), 353–368. https://doi.org/10.1139/E09-072

Gabrielse, H., Murphy, D. C., & Mortensen, J. K. (2006). Cretaceous and Cenozoic dextral orogen-parallel displacements, magmatism, and Cretaceous and Cenozoic dextral orogen-parallel displacements, magmatism, and paleogeography, north-central Canadian Cordillera. In Haggart, J. W., Enkin, R. J. and Monger, J. W. H. (Eds.), *Paleogeography of the North American Cordillera: Evidence For and Against Large-Scale Displacements: Special Paper* (Vol. 46, pp. 255-276). St. John's, Canada:

Geological Association of Canada.

Gettings, M. E. (2005). Multifractal magnetic susceptibility distribution models of hydrothermally altered rocks in the Needle Creek Igneous Center of the Absaroka Mountains, Wyoming. *Nonlinear Processes in Geophysics*, *12*(5), 587–601. https://doi.org/10.5194/npg-12-587-2005

Gettings, M. E. (2012). Multifractal model of magnetic susceptibility distributions in some igneous rocks. *Nonlinear Processes in Geophysics*, *19*(6), 635–642. https://doi.org/10.5194/npg-19-635-2012

Goes, S., & Van Der Lee, S. (2002). Thermal structure of the North American uppermost mantle inferred from seismic tomography. *Journal of Geophysical Research, 107*(B3), 2050. https://doi.org/10.1029/2000JB000049

Gordey, S. P. (2013). Evolution of the Selwyn Basin region, Sheldon Lake and Tay River map areas, central Yukon. *Geological Survey of Canada Bulletin 599*, 176 p. https://doi.org/10.4095/293034

Guillaud, C. (1951). Propriétés magnétiques du sesquioxyde de fer Fe2O3α. *Journal de Physique et Le Radium, 12*(3), 489–491. https://doi.org/10.1051/jphysrad:01951001203048900

Hansen, V. L., & Dusel-Bacon, C. (1998). Structural and kinematic evolution of the Yukon-Tanana upland tectonites, east-central Alaska: A record of late Paleozoic to Mesozoic crustal assembly. *Geological Society of America Bulletin, 110*(2), 211–230.

Hasterok, D., & Chapman, D. S. (2011). Heat production and geotherms for the continental lithosphere. *Earth and Planetary Science Letters*, *307*(1–2), 59–70. https://doi.org/10.1016/j.epsl.2011.04.034

Hayward, N. (2015). Geophysical investigation and reconstruction of lithospheric structure and its control on geology, structure, and mineralization in the Cordillera of northern Canada and eastern Alaska. *Tectonics, 34*(10), 2165–2189. https://doi.org/10.1002/2015TC003871

Hunt, C. P., Moskowitz, B. M., & Banerjee, S. K. (1995). Magnetic Properties of Rocks and Minerals. In: T. J. Ahrens (Ed.): *Rock physics & phase relations* (pp. 89–204). Washington, D.C., U.S.A: AGU. https://doi.org/10.1029/RF003

Hyndman, R. D., & Currie, C. A. (2011). Why is the North America Cordillera high? Hot backarcs, thermal isostasy, and mountain belts. *Geology*, *39*(8), 783–786. https://doi.org/10.1130/G31998.1

Hyndman, R. D., Flück, P., Mazzotti, S., Lewis, T. J., Ristau, J., & Leonard, L. (2005). Current tectonics of the northern Canadian Cordillera, *Canadian Journal of Earth Sciences, 42*(6), 1117–1136. https://doi.org/10.1139/E05-023

Hyndman, R. D., Currie, C. A., Mazzotti, S., & Frederiksen, A. (2009). Temperature control of continental lithosphere elastic thickness, Te vs Vs. *Earth and Planetary Science Letters*, *277*(3–4), 539–548. https://doi.org/10.1016/j.epsl.2008.11.023

Kao, H., Behr, Y., Currie, C. A., Hyndman, R., Townend, J., Lin, F. C., et al. (2013). Ambient seismic noise tomography of Canada and adjacent regions: Part I. Crustal structures. *Journal of Geophysical Research: Solid Earth*, *118*(11), 5865–5887. https://doi.org/10.1002/2013JB010535

Kirby, J. F. (2005). Which wavelet best reproduces the Fourier power spectrum? *Computers & Geosciences*, *31*(7), 846–864. https://doi.org/10.1016/j.cageo.2005.01.014

Kumar, P. (1995). A wavelet based methodology for scale-space anisotropic analysis. *Geophysical Research Letters*, *22*(20), 2777-2780. https://doi.org/10.1029/95GL02934

Laske, G. & Masters, G. (1997). A global digital map of sediment thickness. *Eos Transactions AGU*, *78*, F483.

Ledo, J., Jones, A. G., & Ferguson, I. J. (2002). Electromagnetic images of a strike-slip fault: The Tintina fault-Northern Canadian. *Geophysical Research Letters*, *29*(8), 66-1–66-4. https://doi.org/10.1029/2001GL013408

Leonard, L. J., Hyndman, R. D., Mazzotti, S., Nykolaishen, L., Schmidt, M., & Hippchen, S. (2007). Current deformation in the northern Canadian Cordillera inferred from GPS measurements. *Journal of Geophysical Research: Solid Earth*, *112*(B11), B11401. https://doi.org/10.1029/2007JB005061

Leonard, L. J., Mazzotti, S., & Hyndman, R. D. (2008). Deformation rates estimated from earthquakes in the northern Cordillera of Canada and eastern Alaska. *Journal of Geophysical Research: Solid Earth*, *113*(B8), B08406. https://doi.org/10.1029/2007JB005456

Leonardi, S., & Kumpel, H. J. (1996). Scaling behaviour of vertical magnetic susceptibility and its fractal characterization: An example from the German continental deep drilling project (KTB). *Geologische Rundschau*, *85*(1), 50–57. https://doi.org/10.1007/BF00192060

Lewis, T. J., Hyndman, R. D., & Flück, P. (2003). Heat flow, heat generation, and crustal temperatures in the northern Canadian Cordillera: Thermal control of tectonics. *Journal of Geophysical Research: Solid Earth*, *108*(B6), 2316.

https://doi.org/10.1029/2002JB002090

Li, C. F., Lu, Y., & Wang, J. (2017). A global reference model of Curie-point depths based on EMAG2. *Scientific Reports*, *7*, 45129. https://doi.org/10.1038/srep45129

Majorowicz, J., & Weides, S. (2015). *Large scale geothermal high in the westernmost North American covered craton – Can heat flow Vs . basement heat production be a reliable tool in predicting deep EGS geothermal resource?* Proceedings of the 40th Workshop on Geothermal Reservoir Engineering, Stanford University, Stanford, California (pp. 26–28).

Majorowicz, J. A. (2018). Heat flow–heat production relationship not found: what drives heat flow variability of the Western Canadian foreland basin? *International Journal of Earth Sciences*, *107*(1), 5–18. https://doi.org/10.1007/s00531-016-1352-x

Mareschal, J. C., Jaupart, C., Cheng, L. Z., Rolandone, F., Gariepy, C., Bienfait, G., et al. (1999). Heat flow in the Trans-Hudson Orogen of the Canadian Shield: Implications for Proterozoic continental growth. *Journal of Geophysical Research-Solid Earth*, *104*(B12), 29007–29024. https://doi.org/10.1029/1998jb900209

Maus, S., & Dimri, V. (1995). Potential field power spectrum inversion for scaling geology. *Journal of Geophysical Research*, *100*(B7), 12605–12616. https://doi.org/10.1029/95JB00758

Maus, S., & Dimri, V. (1996). Depth estimate from the scaling power spectrum of potential fields? *Geophysical Journal International*, *124*(1), 113–120. https://doi.org/10.1111/j.1365-246X.1996.tb06356.x

Maus, S., Gordon, D., & Fairhead, D. (1997). Curie-temperature depth estimation using a self-similar magnetization model. *Geophysical Journal International*, *129*(1), 163–168.

https://doi.org/10.1111/j.1365-246X.1997.tb00945.x

Mazzotti, S., & Hyndman, R. D. (2002). Yakutat collision and strain transfer across the northern Canadian Cordillera. *Geology*, *30*(6), 495–498. https://doi.org/10.1130/0091-7613(2002)030<0495:YCASTA>2.0.CO;2

Mazzotti, S., Hyndman, R. D., Flück, P., Smith, A. J., & Schmidt, M. (2003). Distribution of the Pacific/North America motion in the Queen Charlotte Islands-S. Alaska plate boundary zone. *Geophysical Research Letters*, *30*(14), 1762. https://doi.org/10.1029/2003GL017586

Mazzotti, S., Leonard, L. J., Hyndman, R. D., & Cassidy, J. F. (2008). Tectonics, Dynamics, and Seismic Hazard in the Canada-Alaska Cordillera. In J. T. Freymuller, P. J. Haeussler, R. L. Wesson, G. Ekström, *Active Tectonics and Seismic Potential of Alaska* (Vol. 179, pp. 297–319). Washington, D. C.: American Geophysical Union. https://doi.org/10.1029/179GM17

McLellan, M., Schaeffer, A. J., & Audet, P. (2018). Structure and fabric of the crust and uppermost mantle in the northern Canadian Cordillera from Rayleigh-wave tomography. *Tectonophysics*, 724-*725*, 28–41. https://doi.org/10.1016/j.tecto.2018.01.011

Monger, J., & Price, R. (2002). The Canadian Cordillera: Geology and Tectonic Evolution. *CSEG Recorder*, *February*, 17–36.

Mooney, W. D., Laske, G., & Masters, T. G. (1998). CRUST 5.1: A global crustal model at 5° × 5°. *Journal of Geophysical Research: Solid Earth*, *103*(B1), 727–747. https://doi.org/10.1029/97JB02122

Murphy, D.C., Mortensen, J.K., Piercey, S.J., Orchard, M.J., and Gehrels, G.E. (2006). Mid-

Paleozoic to early Mesozoic tectonostratigraphic evolution of Yukon-Tanana and Slide Mountain terranes and affiliated overlap assemblages, Finlayson Lake massive sulphide district, southeastern Yukon. In M. Colpron, J.L. Nelson, (Eds.), *Paleozoic Evolution and Metallogeny of Pericratonic Terranes at the Ancient Pacific Margin of North America, Canadian and Alaskan Cordillera: Special Paper* (Vol. 45, pp. 75–105). St. John's, Canada: Geological Association of Canada.

Okubo, Y., Graf, R. J., Hansen, R. O., Ogawa, K., & Tsu, H. (1985). Curie point depths of the Island of Kyushu and surrounding areas, Japan. *Geophysics*, *50*(3), 481–494. https://doi.org/10.1190/1.1441926

Perry, H. K. C., Eaton, D. W. S., & Forte, A. M. (2002). LITH5.0: A revised crustal model for Canada based on Lithoprobe results. *Geophysical Journal International*, *150*(1), 285–294. https://doi.org/10.1046/j.1365-246X.2002.01712.x

Pilkington, M. (2007). Fractal character of oceanic crustal magnetism determined from drill hole measurements. *Indian Journal of Marine Sciences*, *36*(2), 97–104.

Pilkington, M., & Todoeschuck, J. P. (1993). Fractal magnetization of continental crust. *Geophysical Research Letters*, *20*(7), 627–630. https://doi.org/10.1029/92GL03009

Pilkington, M., Gregotski, M. E., & Todoeschuck, J. P. (1994). Using fractal crustal magnetization models in magnetic interpretation. *Geophysical Prospecting*, *42*(6), 677–692. https://doi.org/10.1111/j.1365-2478.1994.tb00235.x

Priestley, K., & McKenzie, D. (2006). The thermal structure of the lithosphere from shear wave velocities. *Earth and Planetary Science Letters, 244*(1–2), 285–301. https://doi.org/10.1016/j.epsl.2006.01.008

Ravat, D., Pignatelli, A., Nicolosi, I., & Chiappini, M. (2007). A study of spectral methods

of estimating the depth to the bottom of magnetic sources from near-surface magnetic anomaly data. *Geophysical Journal International*, 169(2), 421-434. http://doi.org/10.1111/j.1365-246X.2007.03305.x

Ristau, J., Rogers, G. C., & Cassidy, J. F. (2007). Stress in western Canada from regional moment tensor analysis. *Canadian Journal of Earth Sciences*, *44*(2), 127-148. https://doi.org/10.1139/e06-057

Roddick, J. A. (1967). Tintina Trench. *The Journal of Geology*, *75*(1), 23–33. https://doi.org/10.1086/627228

Rolandone, F., Jaupart, C., Mareschal, J. C., Gariépy, C., Bienfait, G., Carbonne, C., & Lapointe, R. (2002). Surface heat flow, crustal temperatures and mantle heat flow in the Proterozoic Trans-Hudson Orogen, Canadian Shield. *Journal of Geophysical Research: Solid Earth*, *107*(B12), ETG 7-1-ETG 7-19. https://doi.org/10.1029/2001JB000698

Ross, H. E., Blakely, R. J., & Zoback, M. D. (2006). Testing the use of aeromagnetic data for the determination of Curie depth in California. *Geophysics*, *71*(5), L51–L59. https://doi.org/10.1190/1.2335572

Russell, J. K., Dipple, G. M., & Kopylova, M. G. (2001). Heat production and heat flow in the mantle lithosphere beneath the slave craton. *Physics of Earth and Planetary Interiors*, *123*, 27–44.

Russell, K., & Kopylova, M. G. (1999). A steady state conductive geotherm for the north central Slave, Canada : Inversion of petrological data from the Jericho Kimberlite pipe surface. *Journal of Geophysical Research*, *104*(B4), 7089–7101. https://doi.org/10.1029/1999JB900012

Saltus, R. W. (2007). Matching Magnetic Trends and Patterns Across the Tintina Fault,

Alaska and Canada — Evidence for Offset of About 490 Kilometers. In L. P. Gough, W. C. Day (Eds.), *Recent U.S. Geological Survey Studies in the Tintina Gold Province, Alaska, United States, and Yukon, Canada—Results of a 5-Year Project: Scientific Investigations Report 2007-5289-C* (pp. C1–C7). Reston, USA: United States Geological Survey.

Schaeffer, A. J., & Lebedev, S. (2014). Imaging the North American continent using waveform inversion of global and USArray data. *Earth and Planetary Science Letters*, *402*, 26–41. https://doi.org/10.1016/j.epsl.2014.05.014

Schult, A. (1970). Effect of pressure on the Curie temperature of titanomagnetites [(1-x) $\cdot Fe_3O_4$ - x $\cdot TiFe_2O_4$]. *Earth and Planetary Science Letters*, *10*(1), 81–86. https://doi.org/10.1016/0012-821X(70)90067-1

Shi, L., Francis, D., Ludden, J., Frederiksen, A., & Bostock, M. (1998). Xenolith evidence for lithospheric melting above anomalously hot mantle under the northern Canadian Cordillera. *Contributions to Mineralogy and Petrology*, *131*(1), 39–53. https://doi.org/10.1007/s004100050377

Smith, R. W., & Fuller, M. (1967). Alpha-Hematite: Stable Remanence and Memory. *Science*, *156*(3778), 1130–1133. https://doi.org/10.1126/science.156.3778.1130

Snyder, D. B., Roberts, B. J., & Gordey, S. P. (2005). Contrasting seismic characteristics of three major faults in northwestern Canada. *Canadian Journal of Earth Sciences*, *42*(6), 1223–1237. https://doi.org/10.1139/e05-027

Snyder, D. B., Pilkington, M., Clowes, R. M., & Cook, F. A. (2009). The underestimated Proterozoic component of the Canadian Cordillera accretionary margin. *Geological Society, London, Special Publications*, *318*(1), 257–271.

https://doi.org/10.1144/SP318.9

Spector, A., & Grant, F. S. (1970). Statistical models for interpreting aeromagnetic data. *Geophysics*, *35*(2), 293–302. https://doi.org/10.1190/1.1440092

Tanaka, A., Okubo, Y., & Matsubayashi, O. (1999). Curie point depth based on spectrum analysis of the magnetic anomaly data in East and Southeast Asia. *Tectonophysics*, *306*(3–4), 461–470. https://doi.org/10.1016/S0040-1951(99)00072-4

Tarayoun, A., Audet, P., Mazzotti, S., & Ashoori, A. (2017). Architecture of the crust and uppermost mantle in the northern Canadian Cordillera from receiver functions. *Journal of Geophysical Research: Solid Earth*, *122*(7), 5268–5287. https://doi.org/10.1002/2017JB014284

Wang, J., & Li, C. F. (2015). Crustal magmatism and lithospheric geothermal state of western North America and their implications for a magnetic mantle. *Tectonophysics*, *638*, 112–125. https://doi.org/10.1016/j.tecto.2014.11.002

Wasilewski, P. J., & Mayhew, M. A. (1992). The Moho as a magnetic boundary revisited. *Geophysical Research Letters*, *19*(22), 2259–2262. https://doi.org/10.1029/92GL01997

Wasilewski, P. J., Thomas, H. H., & Mayhew, M. A. (1979). The Moho as a magnetic boundary. *Geophysical Research Letters*, *6*(7), 541–544. https://doi.org/10.1029/GL006i007p00541

Witter, J., & Miller, C. (2017). Curie point depth mapping in Yukon (Open File 2017-3, 37p.). Whitehorse, Canada: Yukon Geological Survey. https://doi.org/10.13140/RG.2.2.28506.34242

Chapter 4.

Conclusion

Geodynamic processes operating on a lithosphere-scale involve geological processes at various scales, therefore our understanding of geodynamic systems relies not only on the characterization of their geophysical properties, but also the smaller-scale surface processes. In recent years, geophysical studies have shown that the lithospheric architecture of western Canada is complex, marked by a sharp transition between the thick, cold and stable North American craton and the hot and thin Canadian Cordillera (e.g. Audet et al. 2007; Bao et al. 2014; Currie et al. 2008; Lewis et al. 2003; McLellan et al. 2018; Schaeffer & Lebedev 2014). To contribute to a better understanding of the Canadian Cordillera, this thesis provides geological and geophysical constraints on the crust of the Canadian Cordillera at different spatial scales and timescales.

In Chapter 2, numerical modeling of low temperature (U-Th)/He data was used to assess shallow crustal exhumation mechanisms of different crustal blocks within the Yukon Tanana Terrane in the northern Canadian Cordillera. The shallow tectonism of the Yukon Tanana Terrane in west-central Yukon was mainly active in the Cretaceous, coeval with dextral faulting across the northern Canadian Cordillera, facilitating the northwestward displacement of Cordilleran material (Gabrielse et al. 2006; Pavlis et al. 1993). There is a significant contrast between the modeled Cretaceous thermal histories of the structurally higher and lower crustal blocks within the study area. Numerical modeling of (U-Th)/He data coupled with independent geologic data resolve the timing of exhumation of the structurally higher blocks to 118-110 Ma, whereas the structurally lower crustal blocks are modeled to exhume between 85 and 75 Ma. Major faults such as the YRSZ and BCF coincide with the boundaries between

the two domains, which is represented in the (U-Th)/He data by a marked change in age-eU trends. This suggests that faulting was responsible for exhumation, however at this scale, further studies are needed to identify the exact faults and exhumation mechanisms. Future studies may include smaller-scale thermochronology studies in the eastern side of crustal block 2 to confirm if this area did in fact exhume in the late-Early Cretaceous, and assess whether or not the Stewart River fault is more important than previously thought, and is responsible for the disparity in (U-Th)/He data between the eastern and western sides of block 2.

In Chapter 3, Curie depths are estimated from a spatio-spectral analysis of magnetic anomaly data, yielding constraints on geothermal gradients throughout the Canadian Cordillera and Canadian Shield. This study differs from most Curie depth studies by using the wavelet transform to obtain spectral information at a greater spatial resolution than if moving windows were used, while minimizing the effects of spectral leakage and avoiding the negative effects that gaps in the anomaly grid have on moving windows. The Curie depths reflect the results of previous geophysical studies in western Canada, since the Curie depths are much shallower in the Cordillera (15 ± 1 km) than in the Canadian Shield (34 ± 1 km), confirming that geothermal gradients in the crust are much higher throughout the Cordillera, than in the Canadian Shield. An important amelioration for this model would be to improve the z_t map used in the inversion, since we have found that in certain areas, the depths from SEDMAP seem to be much shallower than the depth to the magnetic crust, resulting in erroneous Curie depth results. Furthermore, as discussed in Chapter 3, one of the limitations of this method is that the estimated depth to the base of the magnetized crust may in fact correspond to a geologic boundary that is shallower than the Curie depth. Future studies

involving complementary datasets such as gravity anomaly grids and seismic tomography will be useful for assessing the significance of this issue within our Curie depth results.

References

Audet, P., Jellinek, A.M., and Uno, H., 2007, Mechanical controls on the deformation of continents at convergent margins: Earth and Planetary Science Letters, v. 264, p. 151–166, doi: 10.1016/j.epsl.2007.09.024.

Bao, X., Eaton, D.W., and Guest, B., 2014, Plateau uplift in western Canada caused by lithospheric delamination along a craton edge: Nature Geoscience, v. 7, p. 830–833, doi: 10.1038/NGEO2270.

Currie, C.A., Huismans, R.S., and Beaumont, C., 2008, Thinning of continental backarc lithosphere by flow-induced gravitational instability: v. 269, p. 436–447, doi: 10.1016/j.epsl.2008.02.037.

Gabrielse, H., Murphy, D.C., and Mortensen, J.K., 2006, Cretaceous and Cenozoic dextral orogen-parallel displacements, magmatism and paleogeography, northcentral Canadian Cordillera, *in* Haggart, J.W., Monger, J.W.H., and Enkin, R.J., eds., Paleogeography of the North American Cordillera: Evidence for and against Large-Scale Displacements: Geological Association of Canada Special Paper, v. 46, p. 255–276.

Lewis, T.J., Hyndman, R.D., and Flück, P., 2003, Heat flow, heat generation, and crustal temperatures in the northern Canadian Cordillera: Thermal control of tectonics: Journal of Geophysical Research: Solid Earth, v. 108, doi: 10.1029/2002JB002090.

McLellan, M., Schaeffer, A.J., and Audet, P., 2018, Structure and fabric of the crust and uppermost mantle in the northern Canadian Cordillera from Rayleigh-wave tomography: Tectonophysics, v. 725, p. 28–41, doi: 10.1016/j.tecto.2018.01.011.

Pavlis, T.L., Sisson, V.B., Foster, H.L., Nokleberg, W.J., and Plafker, G., 1993, Mid-Cretaceous extensional tectonics of the Yukon-Tanana terrane, Trans-Alaska Crustal Transect (TACT), east-central Alaska: Tectonics, v. 12, p. 103–122.

Schaeffer, A.J., and Lebedev, S., 2014, Imaging the North American continent using waveform inversion of global and USArray data: Earth and Planetary Science Letters, v. 402, p. 26–41, doi: 10.1016/j.epsl.2014.05.014.